UNIVERSITÁ DEGLI STUDI DI MODENA E REGGIO EMILIA

Dipartimento di Scienze Fisiche, Informatiche e Matematiche

CORSO DI LAUREA MAGISTRALE IN PHYSICS

# Tribovoltaic effect in metal-semiconductor couplings:

## design and optimization of the set-up and investigation of the Al-Si tribo-pair

Relatore:

**Prof. Alberto Rota**

Correlatrice:

**Dott.ssa Elisabetta Salerno**

Laureanda:

**Samantha Roggiani**

ANNO ACCADEMICO 2024/2025

# Summary

**1. Introduction ..... 1**

**2. State of art ..... 4**

*2.1 Contact electrification ..... 4*

*2.2 Triboelectric series ..... 7*

*2.3 Triboelectric effect ..... 9*

*2.4 Tribovoltaic effect ..... 11*

*2.5 Tribovoltaic effect in Al-Si pair ..... 16*

*2.6 Triboelectric effect with DLC ..... 19*

**3. Experimentals ..... 22**

*3.1 Tribometer ..... 22*

*3.2 Electrical set-up ..... 26*

*3.3 Profilometer ..... 28*

*3.4 Scanning Electron Microscope (SEM) and Energy Dispersive X-ray Analysis (EDX) ..... 29*

*3.5 Coating fabrication ..... 30*

*3.6 X-ray Photoemission Spectroscopy (XPS) ..... 31*

*3.7 Test procedure ..... 32*

*3.8 Procedure for tribovoltaic analysis ..... 35*

**4. Set-up 1 ..... 43**

*4.1 Implementation of the standard set-up ..... 43*

*4.2 Preliminary investigation of the tribo-electric properties of Al-Si pair ..... 45*

4.2.1 Tribological characterization: coefficient of friction measurement ..... 51

4.2.2 Morphological characterization: wear rate evaluation ..... 55

4.2.3 Morphological characterization: EDX ..... 58

4.2.4 Electrical characterization: tribovoltaic effect ..... 64

**5. Issues related to set-up 1 ..... 70**

*5.1 Electrical issue ..... 70*

*5.2 Mechanical issue ..... 72*

**6. Set-up 2 ..... 75**

*6.1 Implementation of set up 1 ..... 75*

*6.2 Resulting tribo-electric properties of Al-Si pair ..... 76*

6.2.1 Tribological characterization: coefficient of friction measurement ..... 81

6.2.2 CoF comparison between set-up 1 and set-up 2 ..... 85

6.2.3 Electrical characterization: tribovoltaic effect ..... 86

**7. Collateral measurements ..... 91**

*7.1 Investigation of the tribo-electric properties of DLC-Si pair ..... 91*
7.1.1 Deposition of DLC ..... 91
7.1.2 Chemical characterization: XPS ..... 92
7.1.3 Results of DLC deposition ..... 95
7.1.4 Tribological characterization: coefficient of friction measurement ..... 99
7.1.5 Morphological characterization: EDX ..... 103
7.1.6 Potential future investigations ..... 108

**8. Conclusions and possible development lines ..... 109**

**9. Bibliografia ..... 111**

# 1. Introduction

The increasing demand of energy in modern society boosts in designing and developing new processes, materials and devices able to fulfil this requirement (1). The current demand for energy gives rise to a set of problems: great exploitation of energy sources, energy transport, energy storage, disposal of exhausted materials (2) (3). Among all the energy-dependent systems, some personal devices need a relative small amount of energy (portable pc, smartphone, tablet, smartwatch, etc.). However, they all need almost daily recharge, and their diffusion makes their impact on the energy production significant. A successful power generator for these devices must be lightweight, scalable, resistant to mechanical stresses of various kinds and not dangerous to human health, but also capable of providing a significant energy output without a primary energy input being necessarily constant over time (4).

A possible solution could be the use of triboelectric nano-generators. Triboelectric nano-generators allow the transformation of mechanical energy into electrical energy. They operate on the mechanisms of triboelectrification. Triboelectrification (TE) is one of the most conventional phenomena that occurs in all phases (solid, liquid, gas) in our daily life. It is a convolution of friction and contact electrification (CE), which refers to the presence of electric charges on the surfaces after their contact (5).

The present Master Thesis is part of a larger project ("Tribo-Electricity: a New Route for Tribology (TRIEL)", funded by NextGeneration EU) which aims at providing a deeper understanding of TE phenomena, by investigating it both at the fundamental level and at the macro-scale. The final goal of the project is to suggest possible directions for efficiency improvements. In particular, this Thesis focuses on the experimental measurement of the voltage induced by metal-semiconductor couplings in relative motion. The study is parametric, since it analyzes how the produced voltage is affected by the sliding settings, environmental conditions and materials. For that purpose, a dedicated experimental set-up has been assembled and tribological tests with the concurrent measurement of the electric response have been performed. The extracted data have been analyzed and are going to be discussed in comparison with the existing literature (6).

In this respect, this research is expected to constitute the triggering stage of a much broader research field, mostly unexplored, which is connected to vast scientific and technological applications.

Triboelectric nanogenerators operate on the mechanisms of CE and friction. Most previous studies focused on alternate voltage scenarios, consequently needing rectification prior to utilization. On the other hand, tribovoltaic nanogenerators (TVNGs) produce DC voltage outputs on many material couplings. On the basis of the most reliable theories, a TVNG operates on the mechanism of electron-hole pairs created as a result of the energy released during sliding (7) (8).

In literature, various material couplings have been investigated to understand the mechanisms (5), but until now the details on the electronic changes occurring at the atomic and molecular level, as well as their relation with the energy produced during friction, are still debated. Thus, there is the need to further investigate this topic to develop a robust method for the exploitation of the phenomenon.

One of the important part of this thesis is related to the design and optimization of the experimental set-up. A standard tribometer has been modified to collect in real-time the tribovoltaic signal generated in sliding contact during reciprocating motion. For this purpose, the existing reciprocating ball-on-plate module has been combined with a circuit consisting of a low noise pre-amplifier and a digital oscilloscope, connected to the moving sample and the static counterpart. In particular, a dynamic Schottky junction is obtained by sliding an Aluminum ball against a Silicon substrate 2 mm thick (Al-Si pair), varying contact pressure, sliding frequency and humidity. Since the tribological properties of the mentioned pair are expected to be strictly connected to the outcoming tribovoltage, friction and wear of the Si substrate and of the Al ball have been estimated and compared with the corresponding generated voltage.

# 2. State of art

## 2.1 Contact electrification

CE is the phenomenon by which two materials acquire electrical charges upon coming in contact and being separated. This effect can occur between both conductors and insulators and mechanical friction is not necessary although it can aid in delivering the charges.

CE mechanism has been long debated to understand the basic transfer model that describes it. The discussed possibilities were electron transfer, ion transfer, or even materials species transfer, but all the experimental results support the electron transfer model. Here some results are proposed:

- the mechanism of releasing surface charges follows the electron thermionic emission model since more triboelectric charges are transferred at lower temperatures (1);
- higher humidity provokes the transfer of fewer charges with respect to the 0% humidity case which represents the maximum charge transfer, but in ion transfer model water has a crucial role (2) (3);
- CE is observed at 623K when there are hardly any water-related ions remaining on solid surfaces (4);
- CE is observed higher in vacuum case than in atmosphere pressure, where more water molecules are present (5).

Based on these studies, the conclusion is that CE is largely, if not exclusively, due to electron transfer.

To better understand CE, an introduction about the two possible interactions between atoms is needed. Atomic interactions could be repulsive or attractive depending on the distance between the atoms, as shown in *Figure2.1*:

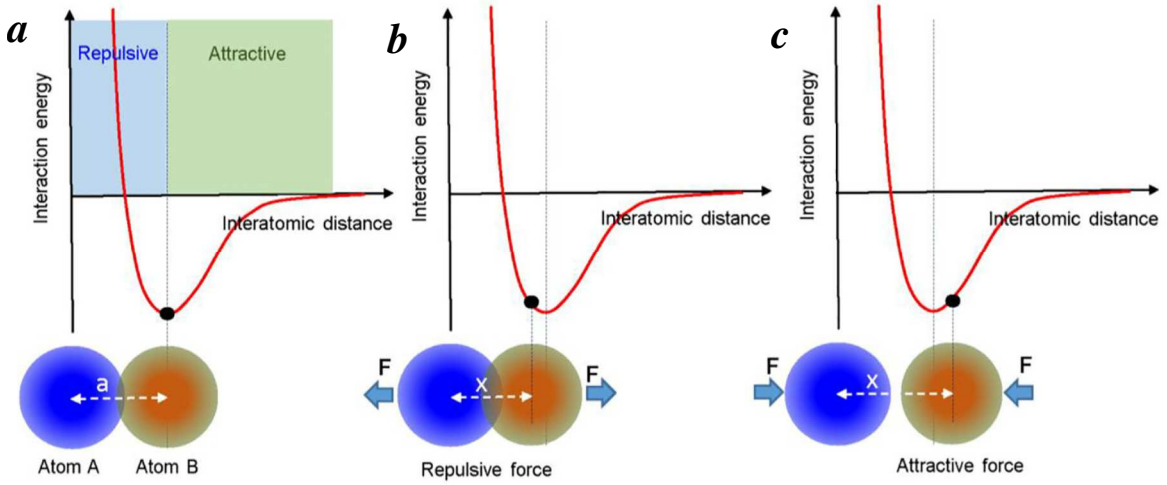



*Figure2.1:* Interatomic interaction potential between two atoms and the force between the two when they are (*a*) at equilibrium position, (*b*) with strong electron cloud/wave-function overlap in the repulsive region, and (*c*) with little electron cloud/wave-function overlap in the attractive region.

*Figure2.1a* represents the equilibrium regime, where the interatomic distance *x* is equal to the *a*, the bond length. Indeed, the two represented atoms have a sort of overlap in electron clouds or wave function. While in *Figure2.1b*, the distance *x* is shorter than the bond length *a* thus it corresponds to the repulsive regime. Instead in *Figure2.1c* an attractive force is applied between the two atoms, representing the attractive regime.

In CE, the external force applied to put in contact the two surfaces has a key role: it has to generate a local high pressure that allows the interatomic distance to be shorter than the bond length *a*, resulting in local repulsive regime. In this regime, CE is experienced because of the increase overlap in local electron clouds, leading to electron transition from one material to the other. *Figure2.2* allows to explain this atomic-scale charge transfer mechanism (6) (7) through the electron-cloud-potential-well model:

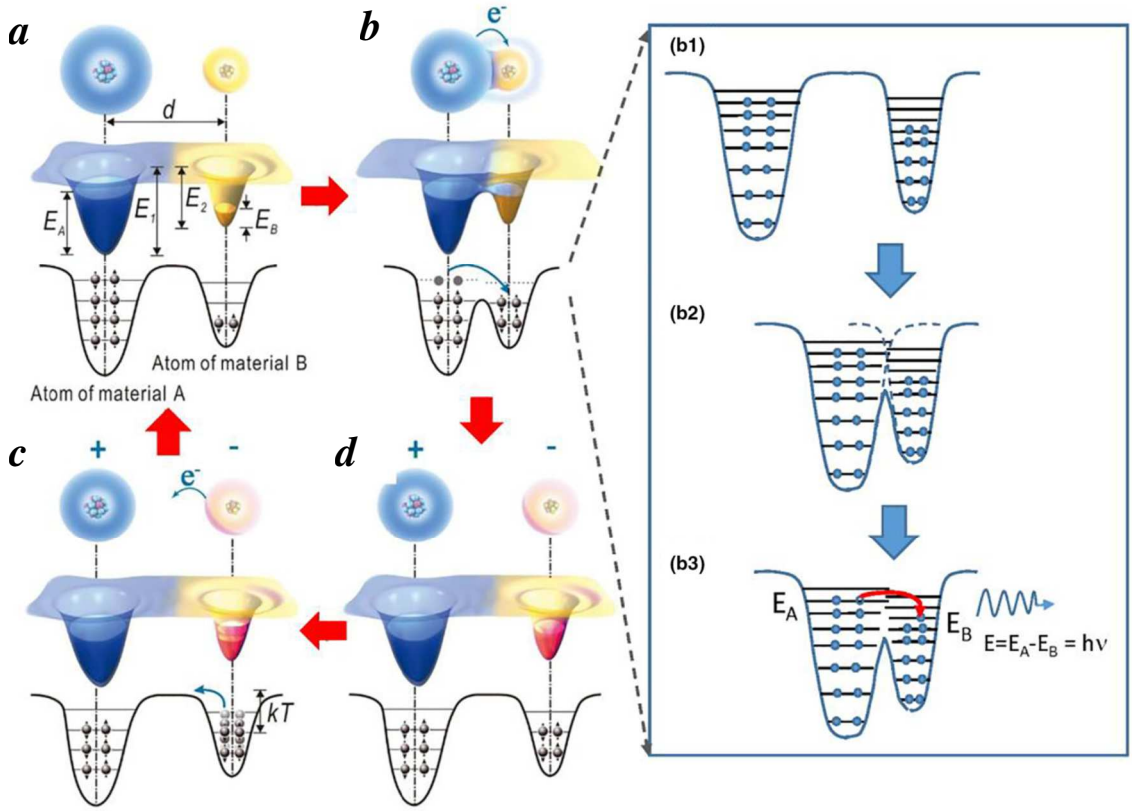



*Figure2.2*: An electron-cloud-potential-well model proposed for explaining CE and charge transfer and release between two materials that may not have well-specified energy band structure, for general material cases. *d* = distance between the two nuclei; $E_A$ and $E_B$ are potential energies for electrons to escape.

In this model, two different materials A and B are considered, specifically the focus is on two atoms, one per material. Each atom is represented by its electron cloud and potential energy profile (3D and 2D). In (*a*) the contact of the two materials does not occur, thus their respective electron clouds remain separated without overlapping. The electrons are tightly bounded in specific orbitals and they can't move from them. In (*b*) the atoms get close to and are in contact, leading to an electron cloud overlap. Indeed, in this case, mechanical contact allows to shorten the distance between atoms, causing a strong overlap. The initial single potential wells become asymmetric double well potential, leading to a reduction of the energy barrier between the two atoms. This allows electron transfer from one atom to the other, resulting in CE. When the distance increases, after contact, the transferred electrons remain as static charges on the material's surface, as shown in (*c*). (*d*) represents the charge release from the atom when an elevated temperature T occurs, i.e. once kT approaches the barrier height.

In the right blue box, (*b1–b3*) are detailed illustrations of (*b*) to show that the increased electron cloud overlap results in a lower potential barrier between the two atoms, resulting in interatomic electron transition and possible photon emission (with energy ~ tens of *eV*) (8).

## 2.2 Triboelectric series

As previously described, during contact, electrons can transfer from one material to another. Consequently, one material loses electrons, while the other gains electrons.

Over the past decades, various material pairings have been tested to classify materials based on the surface charge effect upon contact (9). However, quantifying CE behavior of a single material remains challenging due to two main factors:

1. The CE mechanism involves two materials, making the performance of one dependent on the properties of the others;
2. CE is highly sensitive to surface characteristics, as the process occurs at material interface.

A standardized method has been proposed to consistently evaluate triboelectric phenomena, beyond just CE, for a wide range of materials. To maximize contact uniformity, a liquid metal is employed as the reference counterpart. Using this approach, the normalized triboelectric charge density (TECD) has been introduced to quantify the tendency of materials to gain or lose electrons (8) (*Figure2.3*).

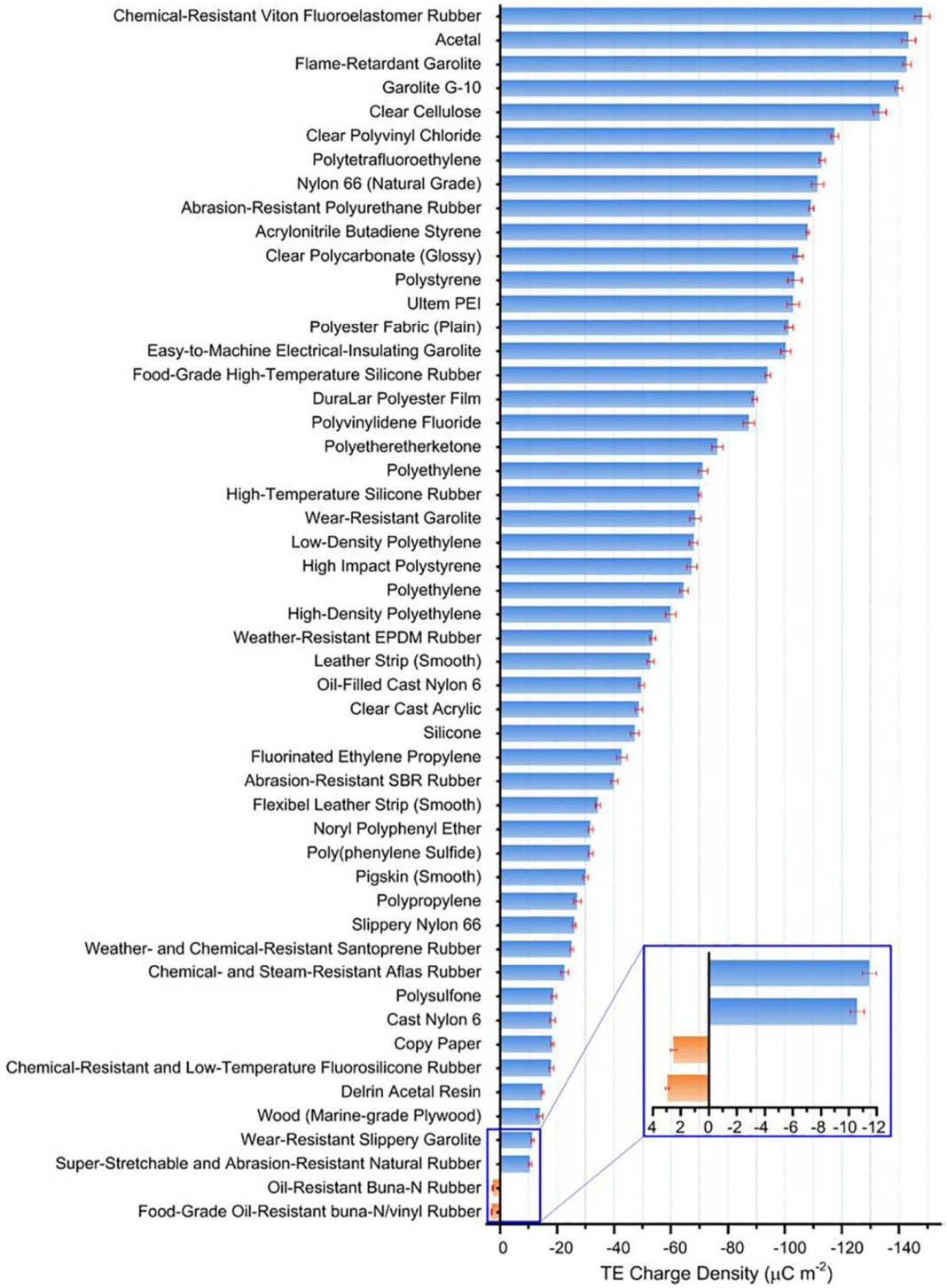



*Figure2.3:* the TECD of over 50 materials.

The position of the material in the triboelectric series determines how effectively the charges will be exchanged (8).

## 2.3 Triboelectric effect

TENGs allow the conversion of mechanical energy into an electrical output.

This category of NGs is also currently gaining increasing interest in the research community, thanks to its intrinsic characteristics such as:

• The wide degree of freedom in the choice of used materials;

• The possibility of adapting them to multiple conditions of use;

• The high power-to-weight ratio;

• The high structuring possibilities (10).

In its most common case, a TENG consists of two layers of different dielectric materials, superimposed but not constrained in contact; two electrodes are in contact with the faces opposite those adjacent to the other dielectric and then connected to each other through the external circuit (in *Figure2.4I*)

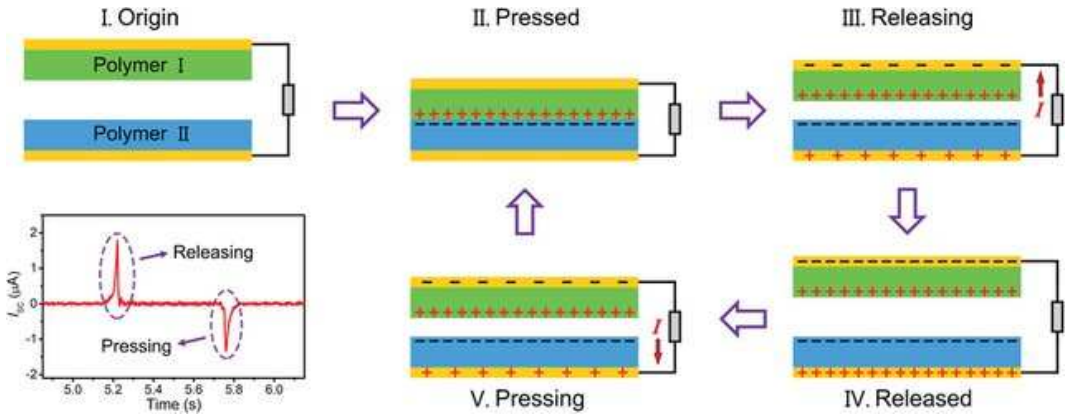



*Figure2.4*: Sketches illustrating the working principle of the TENG in contact-separation mode (11).

When a mechanical force is applied to the nanogenerator, it brings the two dielectric layers into contact, initiating a charge transfer between their surfaces via CE mechanism. Since the materials are dielectric, the transferred charges remain confined to the inner surfaces (those opposite the electrodes).

While the two dielectrics are in contact, the electrostatic charges are balanced, and no net potential is observed between the electrodes. However, upon separation, the spatial displacement of opposite surface charges creates an electrostatic field. To maintain electrostatic equilibrium, a charge redistribution occurs in the electrodes: electrons flow through the external circuit, generating a measurable potential difference and inducing a corresponding charge density.

When the external force is applied again, a new contact-separation cycle begins. As the charged surfaces come into contact again, the electrostatic field decreases, the induced

potential drops, and the electrons now flow through the circuit in the opposite direction. This generates a current of opposite polarity, returning the system to a condition similar to the initial one.

Repeating this contact-separation cycle multiple times, an alternating current is generated, with a frequency directly related to the frequency of the applied mechanical force (12).

Till now, TENG mechanism is described considering the contact-separation mode. Depending on the material used and on the operating mode, it is possible to distinguish four different operating mode:

a. Contact-separation (CS)
b. Lateral sliding (LS)
c. Single electrode mode (SE)
d. Freestanding triboelectric-layer (FT)

The basic mechanism is the same for all of these, but the building elements and the operating directions are different. In *Figure2.5* a schematic draw for each mode is shown:

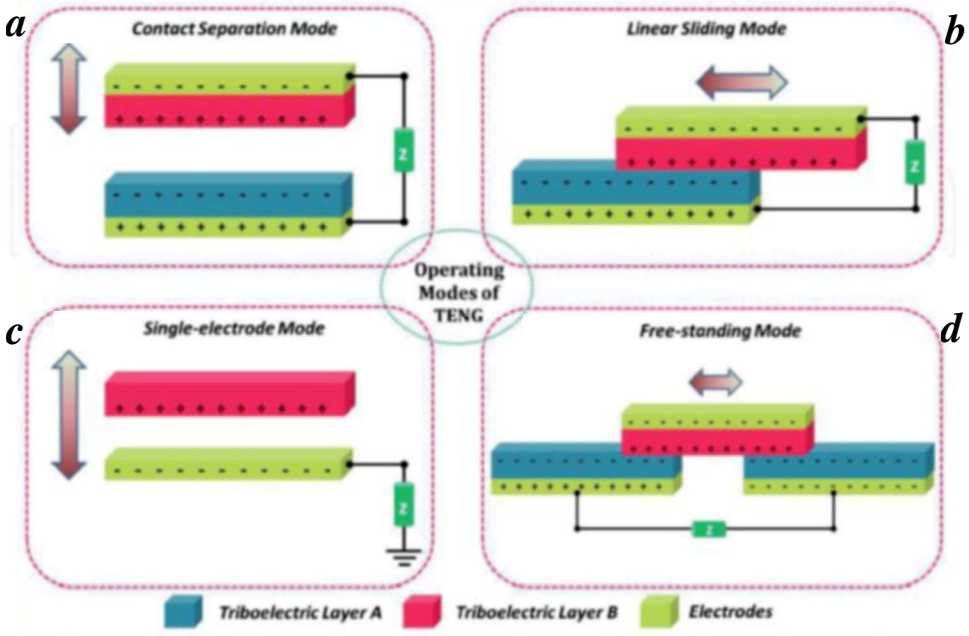



*Figure2.5:*Schematic representation of the four TENG modes: (*a*) CS, (*b*) LS, (*c*) SE and (*d*) FT (13).

In the Contact-Separation (CS) mode, the relative motion between the triboelectric layers is perpendicularly to the contact surfaces. The separation distance directly influences the generated potential difference and, consequently, the current produced in the external circuit.

Its simple structural design allows for easy fabrication, contributes to reducing overall production costs and permits the production of a multi-unit stacking for the enhanced output performance.

In the Lateral Sliding (LS) mode, the motion is parallel to the interface, thus the two triboelectric layers slide relative to each other. The variation in in-plane distance between charges induces a potential difference necessary to establish a current in the external circuit. A rotational version of this mechanism can also be implemented using a rotary structure: this is a more compact solution.

In the Single-Electrode (SE) mode, the relative movement between the triboelectric layers can be both vertically and laterally. As the name suggests, only one electrode is used, while the ground is used as a reference electrode to close the external circuit. This configuration is particularly useful when one of the surfaces cannot be connected to an electrode, allowing for more flexible integration in real-world applications. Despite this, the output performance is too low due to the small charge transfer, making the generated voltage and current to be less than in the other modes.

In the Freestanding Triboelectric-layer (FT) mode, the working principle is similar to LS, but in this case, the potential difference is generated between two fixed, symmetrical electrodes that are in contact with two triboelectric layers. As a freestanding triboelectric material slides over them, a varying potential is established between the electrodes, resulting in a flowing current in the external circuit. In this case, it gives high output efficiency (9).

## 2.4 Tribovoltaic effect

In the most common configuration previously discussed, the voltage output is alternate (AC voltages), consequently needing rectification prior to utilization (14). A better alternative would be represented by direct current (DC) voltage sources which can be used without incurring any losses during rectification on portable or large-scale applications. In this respect, TVNGs produce such DC voltage outputs on many material couplings, composed of metal-semiconductor, p-n junction, metal-insulator-semiconductor or metal-insulator-semiconductor (15) (16).

The first observation of DC signal generation during one experimental test dates to 2018, when Liu et al. analyzed sliding between a metal probe on a molybdenum disulfide (MoS2) film (17). Simultaneously, the presence of electron tunneling in metal-insulator-semiconductor triboelectric interfaces was identified (18). The first denomination of this phenomenon as “tribovoltaic effect” is introduced by Wang et al. in 2019 (8). The experimental validation of the phenomenon is given by Xu, Lu, Lin et al. in the same year (19) (20) (21). In 2020, Zhang et al. provided a formal definition of the tribovoltaic effect,

describing it as the generation of direct voltage and current through mechanical friction at semiconductor interfaces; band theory and friction-induced carrier excitation allow the explanation of this effect (22). Furthermore, they proposed a coupling power generation mechanism that combines the tribovoltaic effect with the thermoelectric effect (23). Lin et al. demonstrated a new approach for harvesting energy from liquid motion since the DC generation from liquid-solid friction (24). Song et al. measured DC generation when a metal tip slid over zinc oxide (ZnO) nanowires, with the output strongly correlated to the concentration of oxygen vacancy defect states on the ZnO surface (25). In 2021, Meng et al. developed an organic TVNG based on flexible interfaces, expanding the potential of TVNGs in wearable electronics (26). That same year, Huang et al. explored a superlubricated structural TVNG based on graphene with a micro-lamellar structure. TVNG in low temperatures conditions were explored by Zheng et al., noting an improvement in efficiency as the temperature decreased (27). The interfacial electric fields are used to explain the tribovoltaic mechanism in 2022 by Zhang et al. (28) (29). Qiao et al. enhanced the wear resistance of TVNGs by utilizing water-based graphene for macroscopic lubrication (30). Yuan et al. designed a rolling-mode TVNG for harvesting both mechanical and solar energy (31). A tunable output of the tribovoltaic effect could be attributed to Yang et al., which took advantage of the transition of Vanadium oxide from metal phase to semiconductor phase (32). In 2023, Deng et al. fabricated tribovoltaic textiles using organic semiconductors, enabling distributed sensing applications (33). Dong et al. innovatively created a freestanding-mode TVNG and integrated it into rolling bearings to capture mechanical friction energy (34) (20).

The present study sets in the above delineated context, aiming at investigating the tribovoltaic effect generated between metal-semiconductor interfaces in relative linear sliding motion under reciprocating module, that is a back-and-forth movement between counterparts along a linear path, as shown in *Figure2.6*.

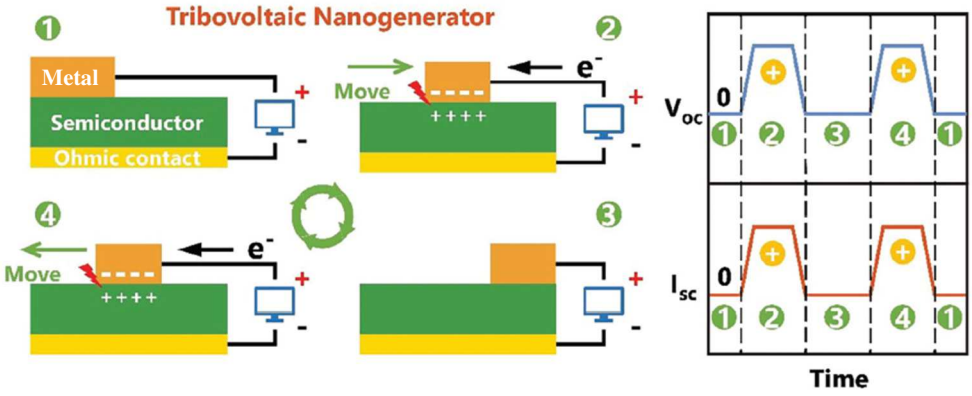



*Figure2.6*: the working mode of sliding-mode tribovoltaic nanogenerator in the case where the work function of the metal $\phi_M$ is smaller than the one of semiconductor $\phi_S$.

It is possible to divide the process into four steps, an alternation of stationary state and dynamic state:

- Step 1: the metal and the semiconductor are in contact with an applied load. In the voltage-time and current-time graphs, this is represented by the absence of signals.

- Step 2: sliding starts, and friction energy excites a flowing of charges resulting in no-zero measurement of voltage and current signal.
- Step 3: metal and semiconductor are in stationary condition, no carriers are excited by friction energy, resulting in zero current and voltage in the external circuit, as in step 1.
- Step 4: while the metal starts to slide in the opposite direction than that in step 2, the motion direction of the frictionally excited non-equilibrium carriers remains unchanged: the generated current and voltage in the external circuit are still positive.

Therefore, this kind of device called TVNG can generate DC voltage during sliding motion.

Compared with TENG, the typical output characteristics of TVNG are high current density (≈A m−2) and low impedance (≈k Ω ) (20).

*Figure2.7* allows a complete description of the working principle at electron-level in the case $\phi_M < \phi_S$,

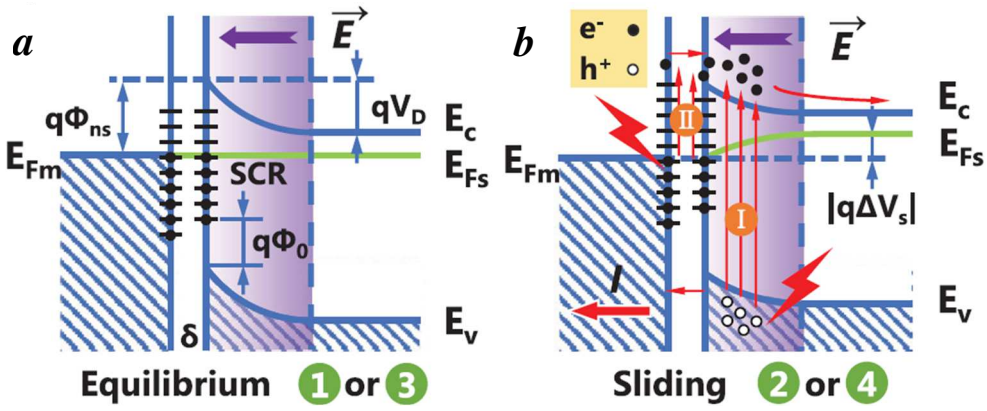



*Figure2.7*: (*a*) Energy band diagram of the metal-semiconductor junction in equilibrium states. (*b*) Energy band diagram of the metal-semiconductor junction in sliding states. ($E_V = highest\ energy\ level\ in\ valence\ band, E_C = lowest\ energy\ level\ in\ conduction\ band, q\phi_0 = \phi_S - \phi_M,$ ).

The energy band diagram in *Figure2.7a* represents the equilibrium situation, thus step 1 and step 3: the two counterparts are in contact with an applied load (CE). Since in the representative case, the Fermi energy level of semiconductor $E_{Fs}$ is higher than that of the metal $E_{Fm}$ (because $\phi_M < \phi_S$), thus the electrons with high Fermi energy levels go from semiconductor to the metal side. This results in a negative charge accumulation on the metal surface and a corresponding positive charge on the semiconductor surface ($q\phi_{ns} = net\ surface\ potential$, due to surface charge density after contact). Consequently, the energy band bends upward, and the built-in electric field $\vec{E}$ is established in the extremely thin space charge region $SCR$ on the semiconductor side.

*Figure2.7b* schematizes the energy band related to dynamic steps, step 2 and step 4. There are two ways to generate moving carriers during sliding:

i) Frictional energy can generate the non-equilibrium carriers in the space charge region of the semiconductor. The friction-induced electron–hole pair move along/against the direction of the built-in electric field.

ii) On the surface state of both counterparts, the electrons obtain friction energy to jump to a higher energy level. The high energy electrons overcome the Schottky energy barrier flowing to the semiconductor side. The electrons that have low energy still have a certain probability of tunneling into the semiconductor side as long as the Schottky energy barrier $qV_d$ is thin enough.

As a result of flowing charges, the external circuit measures a current $I$.

Therefore, the non-equilibrium carriers form a potential energy difference $|q\Delta V_S|$ across the metal-semiconductor junction during sliding (22).

As for the mechanisms through which frictional energy can induce charge movement, two primary interpretations have been proposed.

One study by Zhang et al. supports two sources of energy: one is the released energy due to the newly formed atomic bond, called "bindington", which is quickly taken by the electrons at metal side to jump to an energy level significantly higher than Fermi level, followed by flowing to the semiconductor side; the second one is related to interface lattice rigorously vibration due to the mechanical force of friction, increasing the energy of the atomic system and releasing phonons whose energy can excite electron–hole pairs at a metal–semiconductor (MS) junction (22).

A second study by Lin et al. considers only the formation of a new chemical bonds during sliding, that releases an energy quantum ("bindington") as source of excitation of the electron-hole pairs at the interface (15).

There could also be the case $\phi_M > \phi_S$: the mechanism remains the same, but the direction of the built-in electric field generated by the contact is reversed compared to the previous situation $\phi_M < \phi_S$. Therefore, the charges generated by the tribovoltaic effect and the nonequilibrium carriers move in the opposite direction under this built-in electric field, as shown in *Figure2.8* (22).

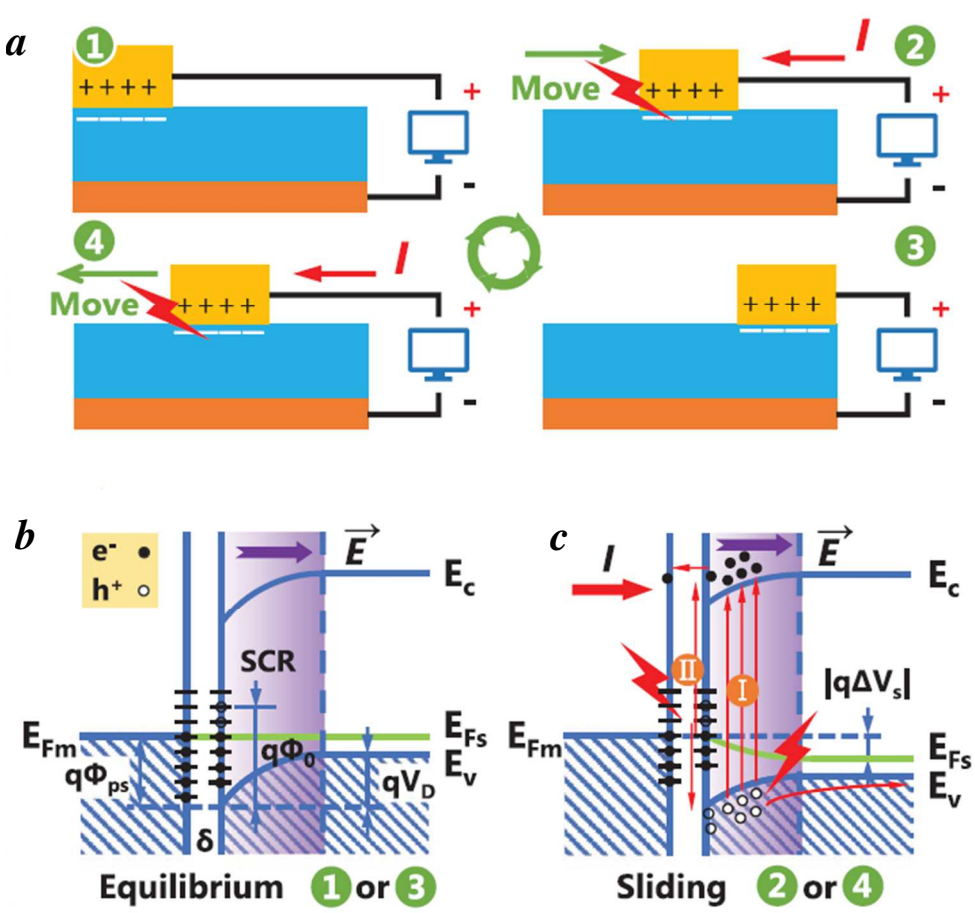



*Figure2.8*: sliding-mode tribovoltaic nanogenerator in the case $\phi_M > \phi_S$.

To summarize *Figure2.9* is the one used by Lin et al. for a clear explanation of the physical mechanisms and demonstration that for a repetition of separated single sliding passage motion in metal-semiconductor junction the expected voltage is a sequence of peaks in correspondence of motion. Here all the possible combinations of semiconductor-metal work functions are considered (35):

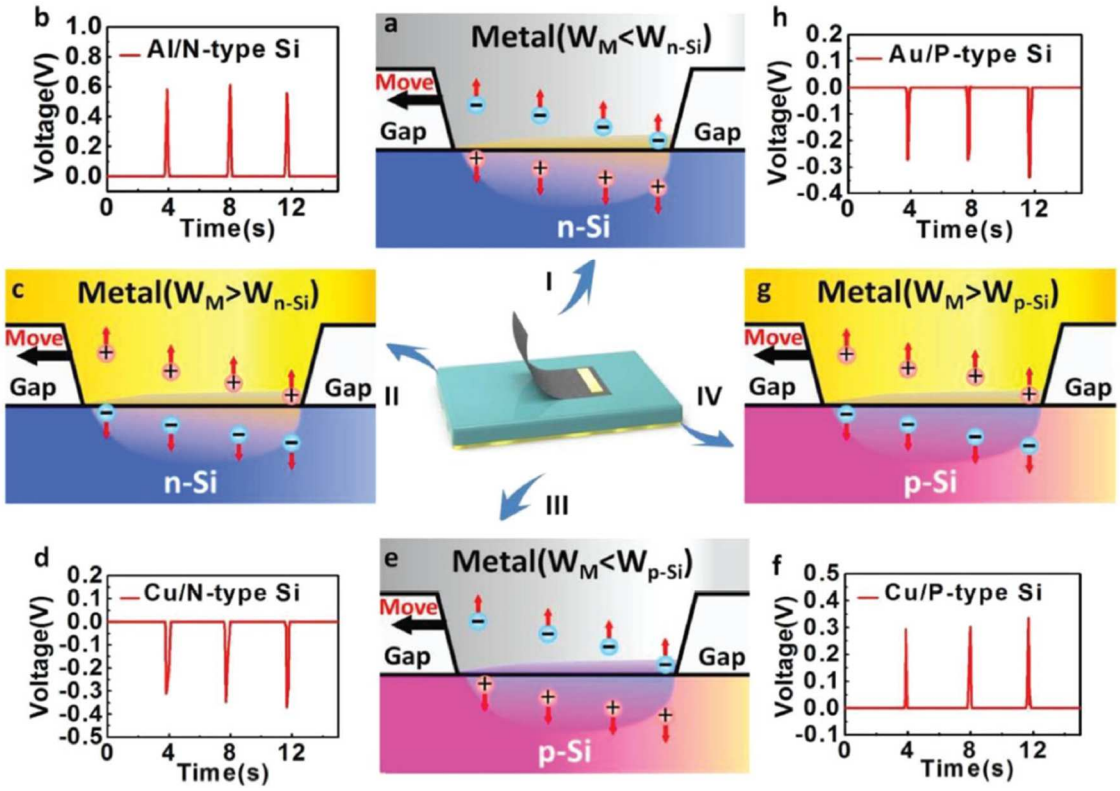



*Figure2.9*: The schematic diagram of the moving Schottky diode–based metal film/Si heterostructure generator with a) $\phi_M < \phi_S$, b) such as Al/N-type Si generator; c) $\phi_M > \phi_S$, d) such as Cu/N-type Si generator; e) $\phi_M < \phi_S$, f) such as Cu/P-type Si generator; g) $\phi_M > \phi_S$, h) such as Au/P-type Si generator. All the electrons and holes in the figure are accelerated or bound back by the built-in field at a subsequent time, depending on the Fermi.

## 2.5 Tribovoltaic effect in Al-Si pair

Over the last years, significant research efforts have been directed toward improving the understanding of the influence of different parameters such as the applied load, the velocity and the humidity on the generated tribovoltage. Through the analysis of recent advancements, it is possible to outline the current state of knowledge and identify areas where further investigation is required.

This study aims to investigate the dependence of the generated tribovoltaic voltage on various tribological parameters. The examinated system involves a metal-semiconductor coupling, specifically an Aluminum ball and a DLC (diamond-like carbon) ball against Silicon substrate, with measurements taken using a standard tribometer. Therefore, only those articles that share relevant aspects with the current work are reviewed.

In 2018, Lin et al. demonstrated a novel continuous DC generator based on the moving Schottky diode, capable of converting mechanical energy into electrical energy through lateral movement between a graphene/metal film and a semiconductor. They proposed the mechanism previously illustrated in *Figure2.9* They analyzed the sliding

motion of an Aluminum foil over n-doped Silicon substrate obtaining maximum voltages peaks of the order of $\sim 10^{-1} V$. Studing the dependence of the electrical output as a function of the sliding velocity, they obtained an increase of the generated voltage with increasing velocity, *Figure2.10* (35).

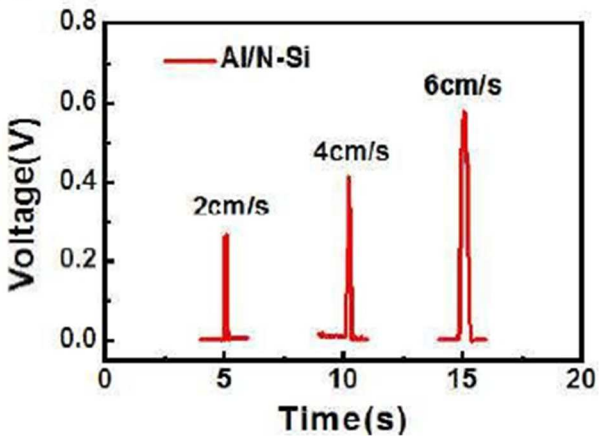



*Figure2.10*: The voltage output of Al/N-Si generator with different speed.

In 2020, Zhang et al. studied the tribovoltaic effect in a metal-semiconductor DC voltage nanogenerator, which consisted of an n-type doped silicon wafer and a stainless-steel block subjected to linear sliding reciprocating motion (*Figure2.11a*). The measured voltage exhibits a continuous and periodic waveform, characterized by a series of peaks with the same period $\Delta t$ of sliding motion between the surfaces, as shown in *Figure2.11b* and *Figure2.11c*.

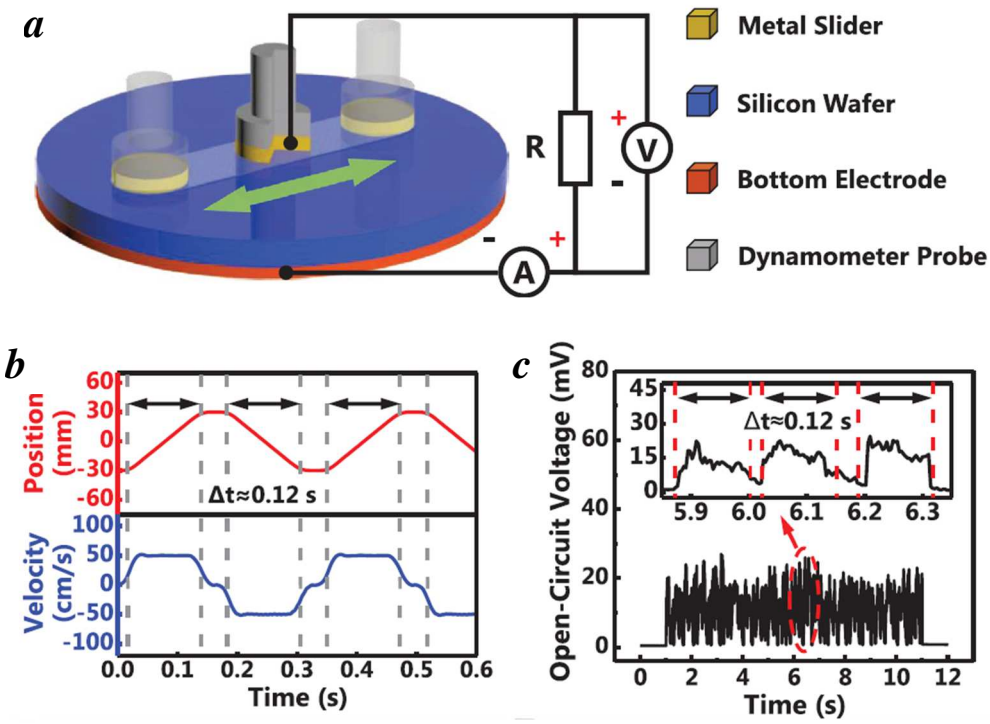



*Figure2.11*: The electric output characteristics of the metal-semiconductor-based DC triboelectric nanogenerator. (*a*) The 3D schematic illustrations of the measurement setup and the external circuit. (*b*) The relative position and velocity of the metal slider and the silicon wafer as a function of time. (*c*) Open-circuit voltage graph. Inset: partial magnified view of the voltage.

They investigated the influence on the generated open-circuit voltage $V_{OC}$ and on the short-circuit current $I_{SC}$ of working parameters, such as the load pressure, sliding velocity and block area. They found that varying the load pressure in the range [2, 18]N resulted in increasing $I_{SC}$ peak while constant $V_{OC}$ peak. Instead, an increase in the slider area or in the sliding velocity (in the range [1,5]cm$^2$) enhances the output of the generator. The obtained $V_{OC}$ and $I_{SC}$ are of the order of $\sim mV$ and $\sim \mu A$, respectively (22).

In 2022, Xu et al. conducted an extensive research on the DC tribovoltaic generator developing a physical model based on semiconductor physics to analyze the effects of several parameters on performance of the tribovoltaic generator. In part of their work they measure the output performances of a nanogenerator in resiprocating sliding motion, formed by different Al meshes/plate and Si sliding wafer (*Figure2.12*).

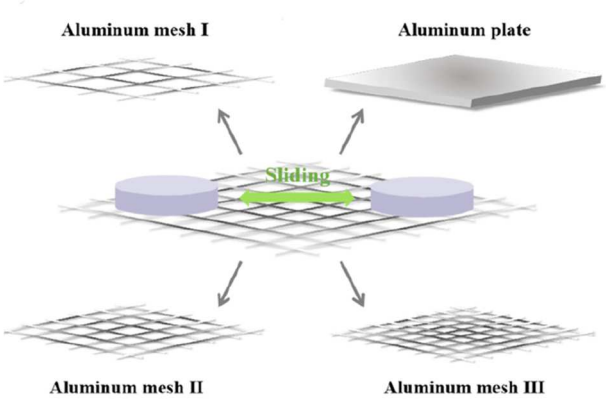



*Figure2.12*: Sketch of Si wafer sliding with four kinds of substrates which have different mesh densities.

Their results show that an increase of contact area, load force in the range [0, 15]N and sliding speed in the range [10, 40]cm/s results in enhanced output, which is in good agreement with the theoretical model (36).

In 2022, Wang et al. demonstrated a humidity-enhanced semiconductor tribovoltaic direct-current nanogenerator (TVNG) using a Cu/Si heterojunction during sliding motion: the open-circuit voltage at RH 90% (0.3 V) is about three times that at RH 30% (0.1 V), and the shortcircuit current at RH 90% (6 mA) is 60 times that at RH 30% (0.1mA). *Figure2.13* represents the experimental data (37):

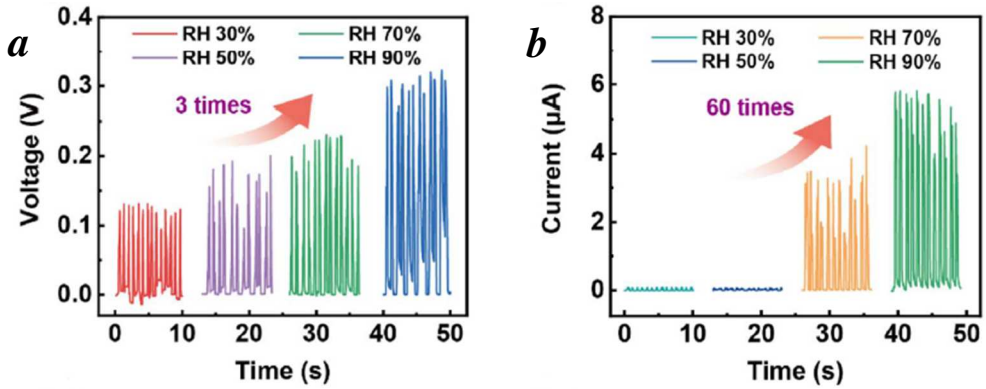



*Figure2.13*: (*a*) Open-circuit voltage and (*b*) short-circuit current of the TVNG in different humidities.

## 2.6 Triboelectric effect with DLC

Diamond-like carbon (DLC) is a family of amorphous carbon (a-C) or amorphous hydrogenated carbon (a-C:H) compounds that contain both $sp^3$ and $sp^2$ bonds. DLC has numerous applications due to its properties, including high hardness and elastic modulus,

excellent wear resistance, low coefficient of friction (38), high thermal stability (except for a-C:H), chemical inertness, biocompatibility, the ability to be deposited at room temperature, smoothness, transparency to infrared radiation and partially to visible light, wide bandgap, high resistivity, and good thermal conductivity (39). Depending on the proportion between the $sp^3$ and $sp^2$ bonds, it behaves like a dielectric if the percentual of $sp^3$ bonds is higher than the one of $sp^2$ bonds, otherwise it is considered like semiconductor (40).

Thanks to its benefits, DLC is one of the most widely used materials for enhancing the mechanical properties of other substrates; if a practical use were also found in triboelectric applications, it would represent an innovative and advantageous development.

Regarding DLC as part of a coupling for TVNG, there are no articles specifically addressing the use of DLC as semiconductor in combination with another semiconductor under sliding motion. Most studies focus on a triboelectric generator with a dielectric material as the opposite counterpart. In 2022, S. Tremmel et al. investigated the triboelectric performance of hydrogenated DLC films, both doped and undoped, when applied as protective coatings on PTFE surfaces in TENGs. They found that undoped a-C:H films exhibited superior output in sliding mode compared to tungsten-doped DLC, primarily due to their higher electronegativity and stability under long-term operation (41). Liu et al. in their article explored the potential of DLC films as active triboelectric materials in contact-separation and sliding-mode TENGs: among the tested configurations, hydrogenated DLC (H-DLC) paired with PTFE yielded the highest power output. They also listed several advantages in using DLC films, such as the increased TENG durability, the anti-friction properties, the cost-effective thickness control and the chemical inertness and resistance in using DLC as TENG counterpart (42).

However, in this Thesis the used DLC is more likely to exhibit semiconducting behavior, and it is analyzed against a semiconductor for TVNG analysis: this represents an innovative aspect with respect to the existing literature.

# 3. Experimentals

This Master Thesis focuses on the experimental measurement of the voltage induced by metal–semiconductor couplings in reciprocating linear sliding motion. The study is parametric, analyzing the influence of sliding conditions, such as applied load, sliding frequency and relative humidity, and material pairings on the generated voltage. To this end, a dedicated experimental set-up was assembled to simultaneously measure the electrical output and the tribological behavior: a standard tribometer was integrated with an external electrical circuit. Thus, tribological tests were carried out with simultaneous measurement of the electrical response. The collected data have been analyzed through a dedicated Matlab script and Excel template.
For a complete characterization, surface topography was analyzed through profilometry, optical microscopy, and scanning electron microscopy (SEM), while chemical analysis was performed via energy-dispersive X-ray spectroscopy (EDX).

In this chapter, the employed tools are described, as well as the testing and analysis procedures used in the experiment. A detailed description of the set-up implementation will be provided in the subsequent chapters.

## 3.1 Tribometer

The tribometer is an instrument that measures the CoF of tribological couplings. In this study CETR-UMT-3 tribometer (Universal Mechanical Tester, Bruker) belonging to the SUP&RMAN laboratory (UniMORE, Modena), was used.(*Figure 3.1*).




*Figure3.1:* CETR-UMT3

The above mentioned tribometer has a modular architecture, meaning that, using the same basic motor, it is possible to set-up different sliding configurations simply by changing the module of the motion. Specifically, the configurations that can be selected are (*Figure3.2*):
- rotary ball/pin-on-disc: the ball/pin slider is kept stationary with respect to a rotating circular surface (disc) while a set load is applied;
- reciprocating ball/pin on plate: a specific load is applied on the ball/pin slider, while it is kept stationary with respect to a back-and-forth motion of the flat surface (plate);
- block-on-ring: a stationary block specimen is pressed against a rotating ring specimen.

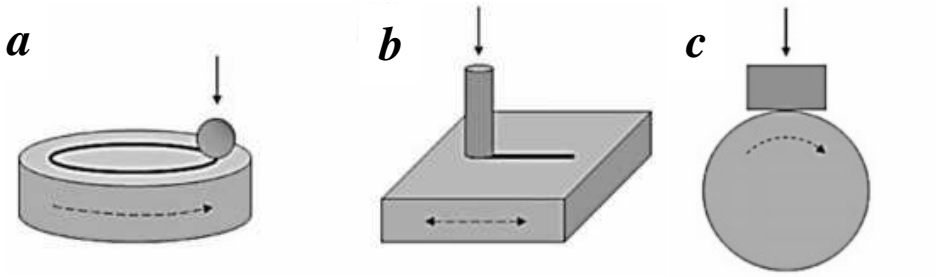



*Figure3.2*: Schematic representation of the possible configuration of the tribometer used: (*a*) Rotary ball/pin on disk. (*b*) Reciprocating ball/pin on plate. (*c*) Block on ring (43)

In the present study the selected configuration was the reciprocating ball-on-flat. This choice is related to the electrical connections necessary to measure the tribovoltaic effect

(see below), that cannot fit with a rotary configuration (in that case, the set-up of sliding contacts would have been mandatory, introducing electrical noise to the system and complicating the set-up). The reciprocating module converts the rotary motion of the basic motor into a linear back-and-forth motion of two contacting surfaces. Indeed, in the bottom part, the instrument features a rectangular base connected to a motor that can move laterally with the set sliding speed. On this base, a ceramic plate and a steel vise are fixed to the holder of the flat counterpart. The other counterbody consists in pin or sphere of different diameter which is set inside a designed cylindric holder (*Figure3.3b).* The ball-holder is maintained perfectly perpendicular to the substrate by two mechanical arms, as shown in *Figure3.3a*.

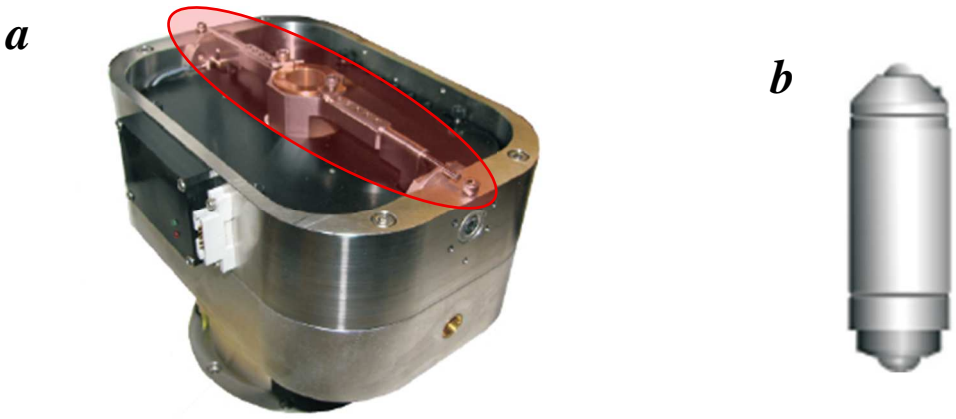



*Figure3.3*: (*a*) Chamber with a UMT-3 Linear Reciprocating Drive. On the top, the two mechanical arms with the specific location of the ball holder are highlighted.
(*b*) the cylindrical ball holder: the bottom extreme corresponds to the pin/ball counterpart.

In this work, the setup has been specifically adapted to fit the experimental purpose. As a result, the architecture of the instrument plays a crucial role in ensuring proper functionality for the measurement. In the following, the main and critical parts (for the purpose of this activity) of the set-up will be described; in that way the importance of the forthcoming implementations will be more evident.
The two mechanical arms are fixed in height, and in order to have the ball holder centered in its support, a precise height of the flat sample is necessary.
Both the original and the designed grabbing system allow the sample to be shifted laterally, allowing multiple tracks to be performed on different areas of the same surface, as shown in *Figure3.4*. Additionally, the fixing mechanism for the ball does not cause any damage, making it possible to reuse the same ball for several tests by rotating it to expose a fresh contact area.

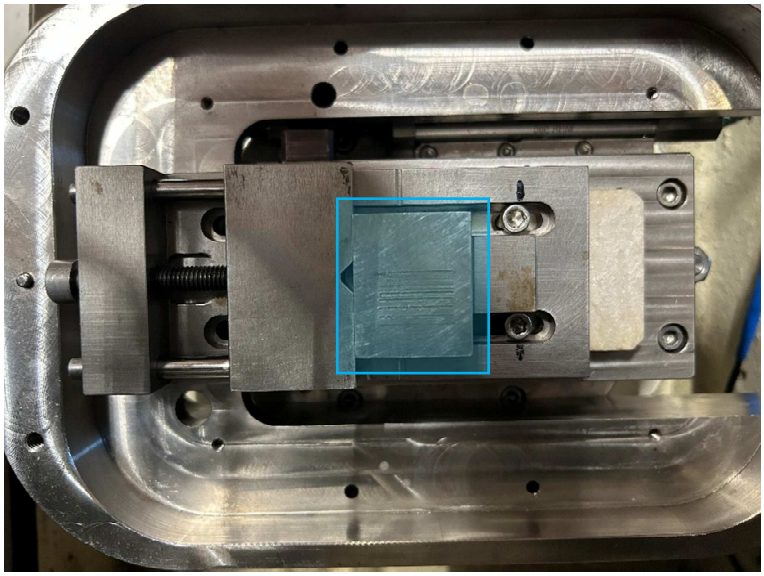


*Figure3.4*: the original set-up comprehending the ceramic plate for thermal isolation and the steel vise. Multiple tests are performed on the same specimen, which is indicated by the blue box.

The top part of the tribometer consists of the head, a mechanical part which drives the lateral and vertical motion of the upper counterbody (ball/pin-holder). The vertical load is applied by the head through the action of an endless screw and of a force sensor, controlled by a PI feedback circuit. On the head, a DFH-100 dual-axis force sensor is situated. The sensor measures the normal force (Fz), which are in a force range (1–1000 N), with a resolution of 50 mN. The sensor is based on strain gauge technology: when a force is applied, the generated mechanical deformation of this element is proportional to its electrical resistance, enabling a precise estimation of the force. Concerning the measurement of the lateral force (Fx), the sensor is situated on the lower drive, specifically along the two horizontal arms.

In the following table (*Table2.1*), the technical specifications of the vertical (Z axis) and horizontal positioning system are reported:

| Characteristic | Z – axis system | horizontal system |
|---|---|---|
| Maximum travel | Up to 150 mm | 120 mm |
| Speed | 0.001 to 10 mm/s | 0.001 to 10 mm/s |
| Position Resolution | 2 micron | 1 micron |
| Encoder Resolution | 0.5 micron | 0.25 micron |

*Table2.1*: technical specifications of the vertical (Z axis) and horizontal positioning system.

The UMT software provides full control of all the motors, both semi-automatic and fully automatic modes with easy to write test sequence, referred to as “recipes”. A recipe consists of a series of steps, each defined by specific mechanical actions, such as sliding frequency, applied load, time duration and feedback control parameters. For each test, users can select

which tribological parameters monitor in real-time during a test and which record for subsequent post-processing. These parameters may include normal and lateral forces, the software-calculated CoF, the lateral and vertical displacement of the ball-holder as a function of time.

Since tribo-voltaic behavior should be closely related to external parameters, such as temperature and humidity, the tribometer is located in a sealed chamber equipped with an analog thermometer and hygrometer to monitor environmental conditions during the test. A gas line connected to the chamber enables fluxing of gases in the ambient, giving the possibility to tune the humidity. In particular, in the present study the tests in low humidity conditions were performed fluxing in the chamber compressed air. The typical relative humidity obtained for these low-humidity tests is in the range [5, 12]%.

## 3.2 Electrical set-up

In order to measure the output voltage (DC signal) generated by the sliding motion, the existing tribometer must be wired to specific electrical devices able to measure in real time the tribo-voltage (oscilloscope, amplifier). This requirement was fulfilled by implementing some parts of the existing set-up. Since the voltage must be recorded in real time during the test, a digital oscilloscope (Picoscope, *Figure3.5*) is connected to the moving sample and the static counterpart in order to collect the electric signal simultaneously. So, the signal is visualized and controlled in real time through the Picoscope software on a computer.

The configuration of the oscilloscope probes was adjusted throughout this work based on the analysis of experimental results, which revealed electrical issues. Therefore, two different set-ups were employed. In the first configuration, standard probes equipped with a slide switch are used: one end includes a grounding alligator clip connected to the moving flat sample, while the other end, featuring a hook tip, enables the measurement of the tribovoltage via contact with the ball holder. In the second set-up, the standard probes are replaced with a custom-made cable ends with two rings-terminated wires, designed so that the ball holder is grounded, while the second terminal is connected to the flat counterpart. In both configurations, the measurement of the generated voltage is made possible by the presence of an insulating layer, positioned between the tribometer base and the flat sample.




*Figure3.5*: Picoscope 2000 series

In *Table2.2,* the principal informations of the instrument are listed.

**Picoscope 2000 series**

| | |
|---|---|
| Source | A, B |
| Voltage range | $\{50\ mV; 20\ V\}$ |
| Coupling mode | AC, DC |
| Time division | $\{2\ ns/div; 5000\ s/div\}$ |

*Table2.2*: main characteristics of the used picoscope 2000 series

Due to the very low amplitude of the generated voltage, a low-noise voltage preamplifier (Stanford Research Systems - SR560 low-noise preamplifier, *Figure3.6*) was used to amplify and filter the signal prior to acquisition.




*Figure3.6*: Stanford Research Systems - SR560 low-noise preamplifier

In *Table2.3*, the main charactetistics are listed.

**(SRS) Model SR-560 Low-noise Pre-amplifier**

| | |
|---|---|
| Input | Differential or single ended |
| Input signal | AC or DC coupled |
| Input noise | 4 nV/√Hz |
| Gain | 1, 2, 5 multiplied by 10, $10^2$, $10^3$, $10^4$ |
| Filter cutoffs | [0.03 Hz;1 MHz] |
| Low-pass/high-pass | $\{6; 12\} db/oct$ |
| Operation mode | Line or battery |
| Interface | RS-232 interface |

*Table2.3*: main characteristics of the used low-noise voltage preamplifier

Summarizing, the signal is firstly amplified and then digitalized and visualized in real-time on a connected computer via the PicoScope software.
*Figure3.7* schematically represents the complete electrical circuit, in the two setups.

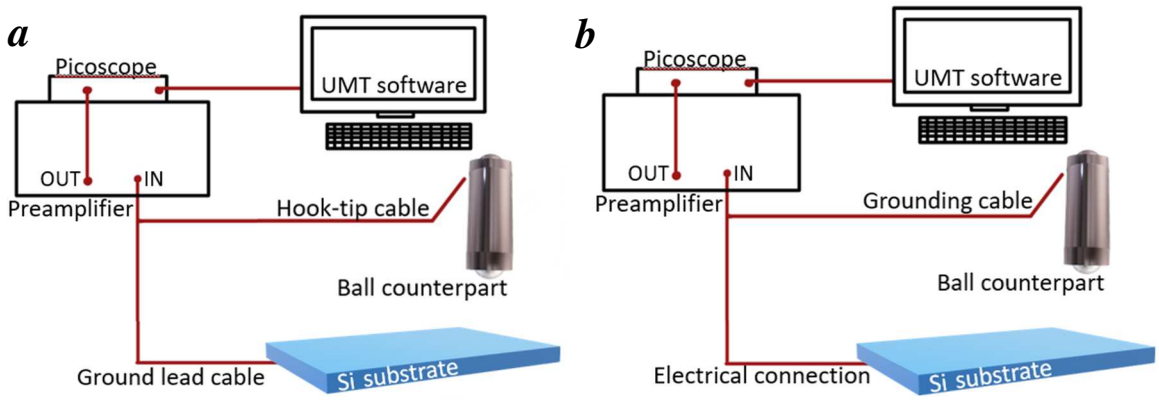



*Figure3.7:* schematic representation of the electrical connections (*a*) in the first set-up and (*b*) in the second one.

## 3.3 Profilometer

The profilometer used in this study is classified as a stylus profilometer, where a "tip" with a radius of curvature of 2 µm gently slides onto the sample tracing its morphology.
Specifically, it is the KLA TENCOR Stylus P6 Profilometer from the SUP&RMAN laboratory, with *Apex 2D and 3D* software.

This instrument consists of a sample holder, a mechanical arm integrated with the stylus, and a capacitive sensor; all of this is associated with the *Profiler* program, which allows for data collection adjustment. The circular sample holder guarantees the stability of the sample, positioned above, during data collection thanks to a pumping system, and allows rotational movements.
The mechanical arm and stylus enable measurement thanks to their mechanical connection to the capacitive sensor, which translates the measured data into an electrical signal. A camera is also available that allows the tip to be positioned on the material, guiding it via the software.

In the following table (*Table2.4*), the main characteristics of the used stylus profilometer are listed:

**Profiler KLA TENCOR Stylus P6**

| | |
|---|---|
| Curvature radius | 2 |
| Angle | 60° |
| Applied force | $[4.9; 49] \cdot 10^{-3}$ N |
| Maximum scan lenght | 150 mm |
| Height range | 1 mm |

*Table2.4*: main characteristics of the used contact profiler

## 3.4 Scanning Electron Microscope (SEM) and Energy Dispersive X-ray Analysis (EDX)

The Scanning Electron Microscope (SEM) allows a magnified view of the sliding surfaces, together with their elemental analysis through the EDX tool. The use of these apparata enables a detailed analysis of the wear processes generated during sliding.

To collect surface structure images and EDX measurements, an *ESEM Quanta-200 from Fei Company - Oxford Instruments*, was used. The instrument has a detector for secondary emitted electrons and one for backscattered electrons, both generated by the interaction between matter and the incident electron beam. Thanks to these appropriate detectors, it is possible to obtain images up to 100000X magnification.

To perform microanalysis, i.e. a compositional analysis with high spatial resolution, an *Oxford INCA-350 X-EDS* system is used. This technique is based on the emission of characteristic X-rays from the sample, excited by the interaction with the incident electron beam. The system is equipped with a thin-window Si(Li) detector for investigations of low-

atomic-number elements, software, and hardware for qualitative and quantitative analyses, and map acquisition.

## 3.5 Coating fabrication

The instrument used for the deposition of the coatings consists of a PVD Magnetron-sputtering apparatus.

The instrument features a high-vacuum chamber (of the order of $10^{-7}$ mbar ) containing two magnetrons Gencoa with target 4" thick 1/4", two shutters to better control the deposition, and system for fixing and moving the plate to which the sample is attached.

To maintain a high vacuum atmosphere, the chamber is connected to a pumping system consisting of a scroll pump for low vacuum, coupled to a turbomolecular pump for high vacuum, and two flow controllers to introduce argon and nitrogen when necessary. The partial pressures of argon and nitrogen are adjustable via a throttling valve.

This technique involves the evaporation of the material to be deposited from a solid source (Cromium and Carbon, in this specific study) in the form of atoms or molecules. These are captures and deflected by the magnetron-generated magnetic field: it stabilizes the plasma that increments the number of impact particles-target and so the sputtering rate. Once the atoms/molecules reach the substrate, they condense and form the desired coating. and the subsequent condensation on the desired substrate. In *Figure3.8* the schematic process in sketched.

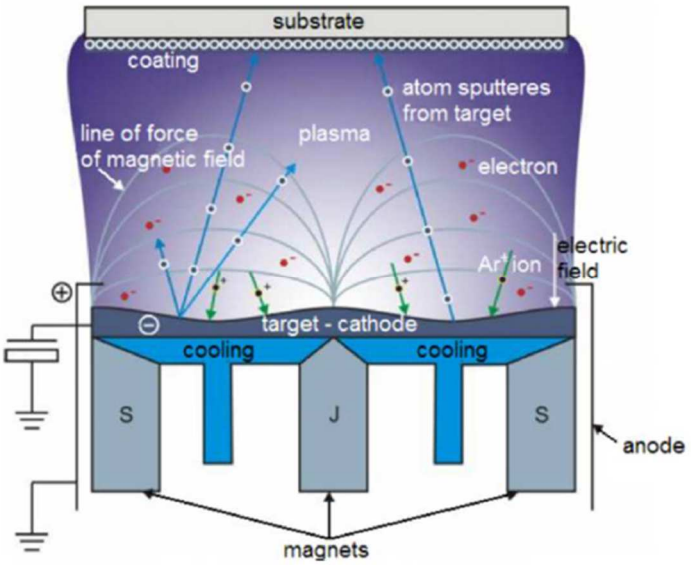



*Figure3.8:* Schematic representation of magnetron sputtering process.

The plasma is triggered by the introduction of an inert gas, in this case Argon, whose atoms are ionized by electrons accelerated by the potential present on the target, which acts as a cathode. The working voltage to sustain plasma is between 500 and 900 V.

The two magnetrons can be powered either by direct current (DC) Huettinger up to a power of 1000W or by an RF Bdiscom power supply, up to a power of 300W with Matching Network.

To improve the adhesion of the coating to the substrate, a technique called "film conditioning" has been used. This technique consists of igniting a plasma on the target before deposition (therefore keeping the shutter positioned on the target): in this way, the impacting ions can remove the surface layers of physisorbed contaminants (formed during the manual positioning of the sample in the deposition chamber).

## 3.6 X-ray Photoemission Spectroscopy (XPS)

X-ray photoemission spectroscopy (XPS) allows a chemical analysis of the first surface layers of the sample.

In XPS technique, an input radiation of intensity I, consisting of photons with energy $h\nu$, excites the solid and estimates the energy of the outcoming electrons. Specifically, it is based on the relationship between the incident radiation, the binding energy of the state from which the electron is photoemitted, and the intensity of the output beam. In fact, if the incident photons have sufficient energy to allow the electrons, which absorb them, to escape from the material, then an output electron beam with energy $E_{cin}$ is detected, such that:

$$E_{cin} = h\nu - E_b - W$$

where $E_b$ is the binding energy of the state from which the emitted electron is photoemitted (estimated by the Fermi level) and $W$ represents the typical work function of the element, i.e., the energy that must be supplied to an electron at the Fermi level to reach the vacuum level.

The collected electrons come from the first surface layers, a few nanometers deep, since these lose energy by inelastically collisions with each other: for this reason, it is a superficial analysis and strongly influenced by contamination. The outgoing beam is then detected by the instrument, that allows the intensity of the output signal to be plotted as a function of the binding energy (*Figure3.9*).

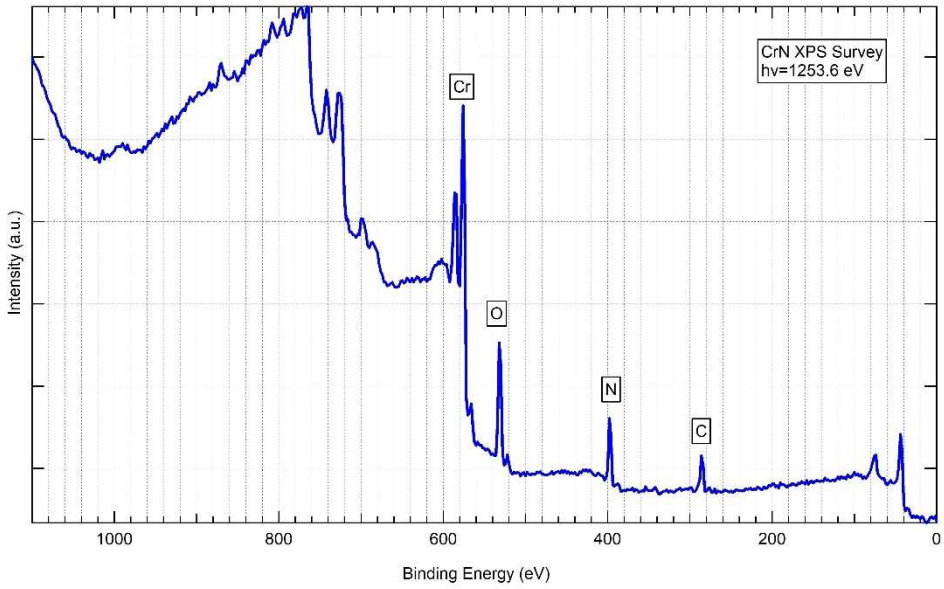



*Figure3.9*: a representative example of XPS survey spectrum.

From the analyses of the resulting spectrum, it is possible to determine the elements that compose the solid and the relative chemical bondings.
Specifically, XPS was used to estimate the chemical characteristic of the films deposited through the magnetron sputtering apparatus above described. The system employed is equipped with a fast-entry chamber, which enables rapid sample introduction without venting the main analysis chamber. After transferring into the analysis chamber, ultra-high vacuum conditions (~$10^{-9}$ Torr) are maintained by a dedicated pumping system. The X-ray source used is a SPECS XRC100, which emits Mg K$\alpha$ radiation (1253.6 eV) generated via thermionic emission from a heated filament that excites a magnesium-coated anode.
The emitted photoelectrons are analyzed by a SPECS Phoibos HSA 3500 hemispherical analyzer, equipped with a 9-channeltron detector.

## 3.7 Test procedure

This project intends to explore the tribovoltaic phenomenon for different material coupling, but this work focuses firstly on Silicon bulk sample as dynamic counterpart tested against Aluminum ball (6.35mm diameter) and subsequently against DLC-coated steel ball (100Cr6, 6.35mm diameter). Due to cost and market availability, the Silicon substrates are purchased with a maximum thickness of 2mm. In *Table2.5* the Silicon characteristics are listed:

| Silicon wafer n- type phosphorus doped | |
|---|---|
| Double side polished | |
| dimensions | 45 x 15 x 2 mm |
| Internal resistance | 0.001 – 0.01 Ω·cm |

*Table2.5*: technical information about Silicon substrate.

To ensure the reliability and accuracy of the experimental results, a proper sample preparation procedure is followed:

- the flat counterpart was blown with compressed air before each test;
- the ball counterpart is first cleaned with ethanol and then blown with compressed air before each test.

Subsequently, the flat substrate is clamped to its support on the tribometer and the ball is placed in its holder. Since the track position must be manually adjusted, careful inspection is done to avoid overlapping with existing tracks.

Once the electrical circuit is connected, the UMT software is employed to configure the test. Through this software, the protocol for the test (i.e. the recipe) can be defined. In this work, multiple tests are performed while varying the working conditions in order to investigate relations between tribological and electrical outputs. The recipe implemented in the tribometer to perform the sliding tests is common to all the explored combinations of parameters, and is composed of the following four steps:

1. Engagement step: the carriage lowers the tribometer head in order to apply to the surface an increasing load up to the set value and then maintain it stable for the selected period $\epsilon\,[10;\ 30]\mathrm{sec}$;
2. Sliding step: the two counterparts start their relative and cyclic motion for the set time $\epsilon\ [100;\ 300]sec$, maintaining a constant load;
3. Final step A: the sliding stops and the tribometer head restores the set load in a period of $\epsilon\,[10;\ 30]\mathrm{sec}$;
4. Final step B: in the following period of $[10;\ 30]sec$, the load is applied steadily to guarantee the finale electric contact.

The recipe simulates the loading and movement conditions of the tribological test, and throughout this work, it has been modified based on the considerations derived from the analysis.

Once the recipe is selected, the test is manually initiated via the tribometer software, which also begins the acquisition of the tribological parameters: Fz, Fx, and the software-calculated CoF. The electrical data acquisition is manually initiated through the Picoscope software. The non-simultaneous start of the tribo-voltaic acquisition results in a time delay between the signals, necessitating appropriate post-processing to synchronize them.

Once a test is completed, the ball holder is electrically disconnected to allow for the optical imaging of the wear scar, enabling post-processing evaluation of the wear rate. To conduct a subsequent test, the substrate is shifted horizontally on the base, and the ball is rotated within its holder to ensure a fresh surface as contact interface for the following test.

The aim of this work is to investigate the relations between tribological and electrical outputs, thus an extensive tribo-electric test campaign is performed.

One combination of parameters is assumed as the standard one (called *Std*) and, starting from this choice, the other conditions are defined by changing one parameter between load, frequency and humidity at a time. In this way, it is possible to define the influence of each one of these on the electrical output.
In *Table2.6*, all the exploited test conditions are listed.

| Denomination | Load [$N$] | Frequency [$Hz$] | RH [$\%$] |
|---|---|---|---|
| *Std* | 20 | 0.5 | ambient ~ 53/55 |
| *Load 30N* | 30 | 0.5 | ambient ~ 53/55 |
| *Load 40N* | 40 | 0.5 | ambient ~ 53/55 |
| *Freq0.8* | 20 | 0.8 | ambient ~ 53/55 |
| *Freq* (1° set-up)<br>*Freq1* (2° set-up) | 20 | 1 | ambient ~ 53/55 |
| *lowRH* | 20 | 0.5 | 5 |
| *RH7* | 20 | 0.5 | 7 |
| *RH12* | 20 | 0.5 | 12 |

*Table2.6*: test conditions are listed with the set parameters

For all the conditions shown in the *Table2.5*, tests of a maximum duration of 300s are performed to study the evolution of the frictional and electric behaviour. Longer duration has been discarded because of the onset of overvoltages (i.e. signal over the set range, so not measurable), tipically after 100s. To obtain sufficient statistical data, 3 tests are performed under the same condition. For this reason, also shorter duration tests (100s) are consequently done to focus on this region. Also in this case, 3 tests are performed for each condition.
To summarize, to obtain sufficient statistical data, 3 tests are performed under the same condition, for each time duration of the tests. With this procedure, six tests for each condition are performed.

The triboelectrical measurements are combined with the topographical and chemical analysis. Thus, for each test, the corresponding track on the substrate is measured using the profiler to evaluate the changes in topography and to assess the wear.
Concerning the chemical characterization, EDX analysis is performed for both the track and the ball, only for the *Std* condition. To obtain reliable elemental composition, both the counterparts are analyzed immediately after the test to minimize the exposure to the environment, which could cause the growth of an oxide layer.

## 3.8 Procedure for tribovoltaic analysis

In this work, the tribological analysis plays a crucial role, as in the literature it is demonstrated that the generated voltage is dependent on tribological parameters. The coefficient of friction, which is a key factor in these interactions, is commonly evaluated using the following formula (*Formula 2.1)*, which considers both the normal force $F_z$ and the lateral force $F_x$:

$$CoF = \left|\frac{F_x}{F_z}\right| \qquad (Formula\ 2.1)$$

In the studied system, the reciprocating linear sliding module is employed, thus the typical shape of the CoF is represented in *Figure3.10.*

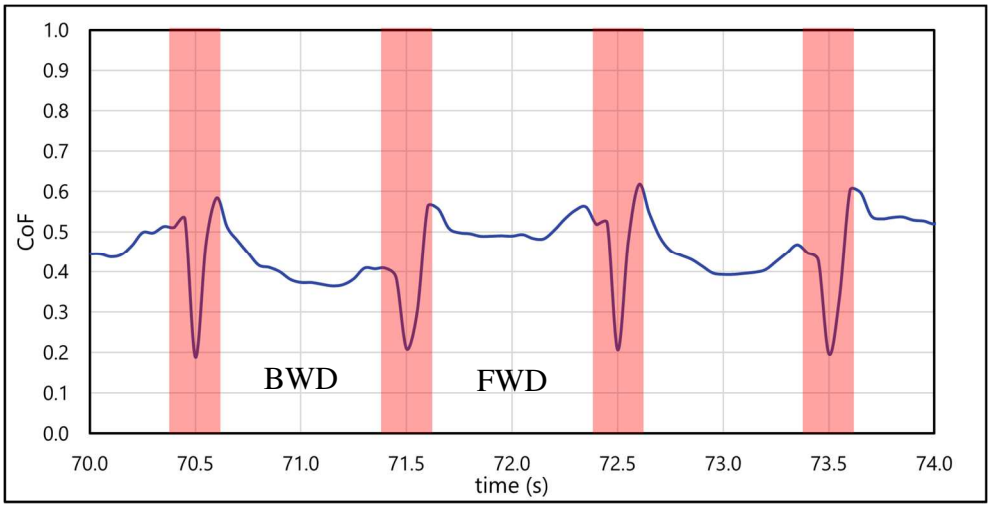



*Figure3.10*: CoF as a function of time: few sliding passages are represented, and the changes in direction are highlighted qualitatively in red. BWD = backward direction, FWD = forward direction.

Reciprocating motion corresponds to a back and forth sliding motion along a stroke: in the central part of the stroke the speed is constant while approaching the extremes the speed changes to allow for the change in motion direction. Consequently, the CoF features negative spikes in corresponding of the changes in motion direction and an ideally-constant average value when the speed is constant.
While performing a test, due to the progressive wearing the CoF increases, as shown in *Figure3.11.*

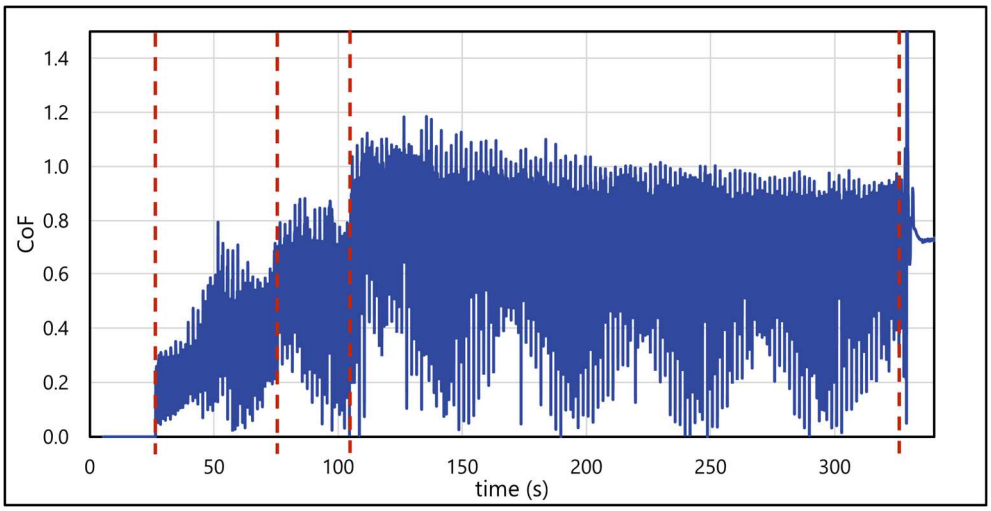



*Figure3.11*: CoF as a function of time during test. The changes in CoF are indicated with red dotted lines.

With the aim of identifying distinct regions within a single test, characterized by different CoF values, a Matlab script is implemented. The script processes the raw tribometer data, specifically Fx, Fz as a function of time t, and at each time instant it computes the CoF using its usual *Formula 2.1*.

The CoF values are then grouped into individual sliding passages, where each passage is defined as a continuous region in which $F_x$ maintains the same sign. For each sliding passage, the average value of the Cof is calculated after discarding the first and last 10% of data points (the extreme of one sliding passage indicated with red boxes in *Figure3.10*).

Subsequently, using a series of *for* loops, the script extracts the CoF average value between forward and backward sliding motions for each cycle. These averages are then compared with the next ones. A transition between friction regions is identified when the difference between the average CoF of one cycle exceeds the average from the previous ones of 30%.

In this case, a global average and standard deviation is extracted from each region. In order to reduce the sensitivity of this method to sudden variations, averages from consecutive regions are finally compared. Only those differing more than their respective standard deviations are effectively considered as separate regions.

To enable rapid visualization of the collected curves, specifically the voltage signal and the Fx, Fz and CoF plots, an Excel template is developed. This template is structured to allow manual identification of key time instants of the test sequence directly on the voltage curve (*Figure3.12)*; in contrast, for the friction this operation is automatized basing it on the calculation of the average and standard deviation of Fx. *Figure3.13* illustrates the sequence of engagement and sliding steps: the average value of Fx is stable, except for minor oscillations, while the onset of sliding is characterized by a deviation in Fx from the average value observed in the previous step.

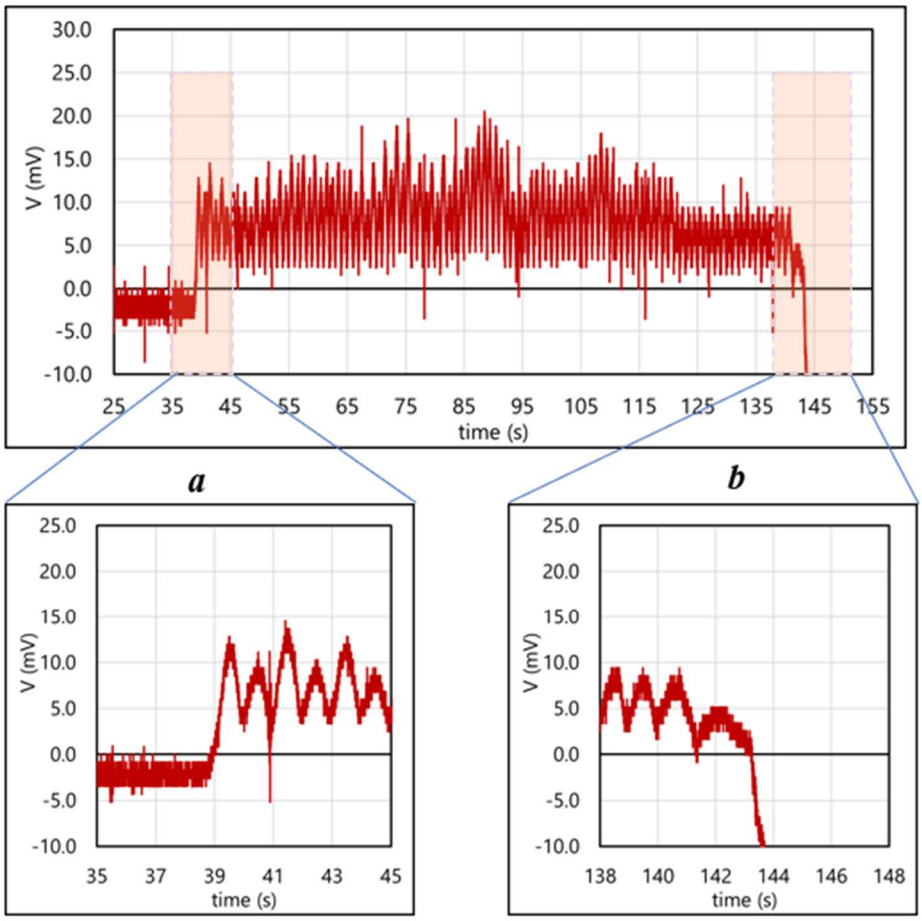



*Figure3.12*: typical voltage signal as a function of time where the key points are highlighted with orange boxes. Insets: (*a*) the start of sliding, (*b*) the end of sliding

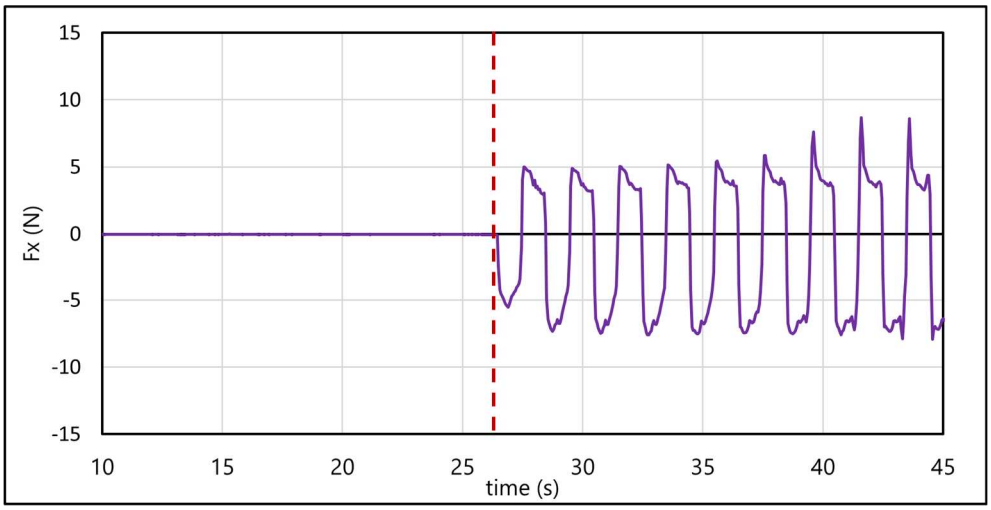



*Figure3.13*: lateral force Fx as a function of time. The red dashed line represents the end of engagement step and the start of sliding.

The identified time instants are subsequently used to temporally align the voltage curve with the friction one. The regions previously identified via Matlab are then imported in the Excel sheet to automatically extract the statistical data of the voltage. These include the average value and the average of the maxima with their respective standard deviation and the absolute maxima value. In this calculation, any overvoltage points (where the voltage exceeds the measured range) are automatically excluded.

Moreover, this Excel sheet allows the selection of specific regions in order to evaluate the presence of possible residual offsets in voltage signal. This enables voltage levels to be zeroed during the step preceding the onset of sliding.

The topographical analysis is performed on both the counterparts by different means.

Focusing on the flat counterpart, the lab Profiler is used.
The wear tracks profiles are measured, and their changes in topography are evaluated. For each track, the height profile is acquired at six positions along the track length. Once one acquisition is completed, the mean height of the pristine surface can be set and levelled using dedicated software and the worn area can be calculated.
In *Figure3.14* an example of profile measure through the instrument and the area calculation directly performed by the dedicated software. It is related to test *Std.2,* a 300s test.

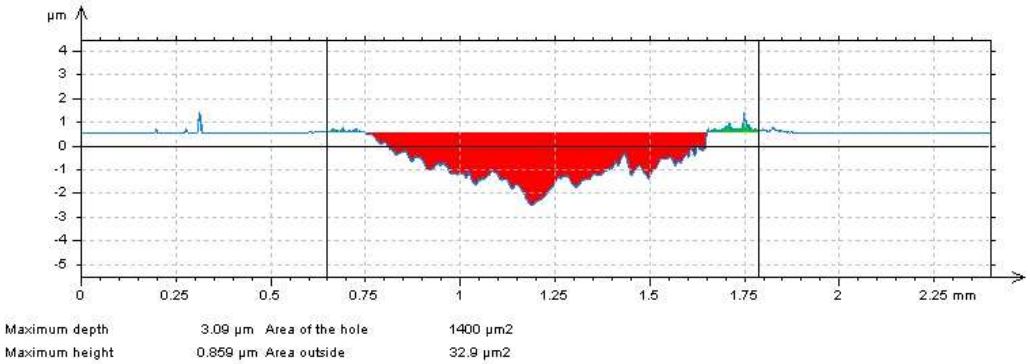



*Figure3.14*: track profile of test *Std.2*. The red area corresponds to the evaluated area for the holes, while the green one is relative to the outside pile-up.

Once the above operations have been performed for each track, it is possible to evaluate the average value of the wear rate $k$, to associate at each test; the relative wear rates are evaluated using the following procedure:

$$k = \frac{V}{F_z \cdot L} \qquad (Formula\ 2.2)$$

where $V$ represents the worn volume by the tribological test

$$V = A \cdot s$$

with $A$ = *worn area from the profiles* and $s$ = *stroke length*, $F_z$ identifies the magnitude of the normal component of the force applied to the surface and $L$ is the linear distance traveled in the tribological experiment

$$L = 2s \cdot f \cdot t_s \qquad \textit{(Formula 2.3)}$$

with $f$ = *sliding frequency* and $t_s$ = *total duration of the test*.

Substituting, we obtain:

$$k = \frac{A \cdot s}{F_z\,(2s \cdot f \cdot t_s)} = \frac{A}{2F_z \cdot f \cdot t_s}$$

For each track, the associated error is calculated following the error propagation theory, accounting for time duration test and Fz error (since it is not negligible), and the standard deviation of the different measured profiles. The error on frequency is supposed to be negligible. Thus, the used formula is the following:

$$\delta k \approx \sqrt{\left|\frac{\partial k}{\partial A}\delta A\right|^2 + \left|\frac{\partial k}{\partial F_z}\delta F_z\right|^2 + \left|\frac{\partial k}{\partial t_s}\delta t_s\right|^2} = \sqrt{\left(\frac{\delta A}{A}\right)^2 + \left(\frac{\delta F_z}{F_z}\right)^2 + \left(\frac{\delta t_s}{t_s}\right)^2} \cdot k$$

For each tribological condition, tests with durations of 300s and 100s are performed. However, according to the wear rate definition, the evaluated wear rate is expected to be independent of test duration. Therefore, 100s and 300s duration tests are grouped in calculating the average wear rate. A single representative value per condition is obtained using a weighted average and the associated error is evaluated following the error propagation theory.
Once all the wear rates for each condition have been determined, they can be compared to identify possible correlations.

With the same purpose, the wear rate is also calculated on the spherical counterpart but with a different analysis. The worn area is calculated through ImageJ software on the images of the optical microscope.
The worn areas are measured on the optical images of the tested balls through the tools of ImageJ software, and their removed volumes are evaluated. The optical images of the wear scar on the ball are taken at 5x magnification, after the removal of debris. For each scar, the area is measured using two selection methods, polygonal and ellipse combination, in order to calculate an average value.

In *Figure3.15*, the optical image of test *Std.2* is reported over which the two selection methods are indicated.

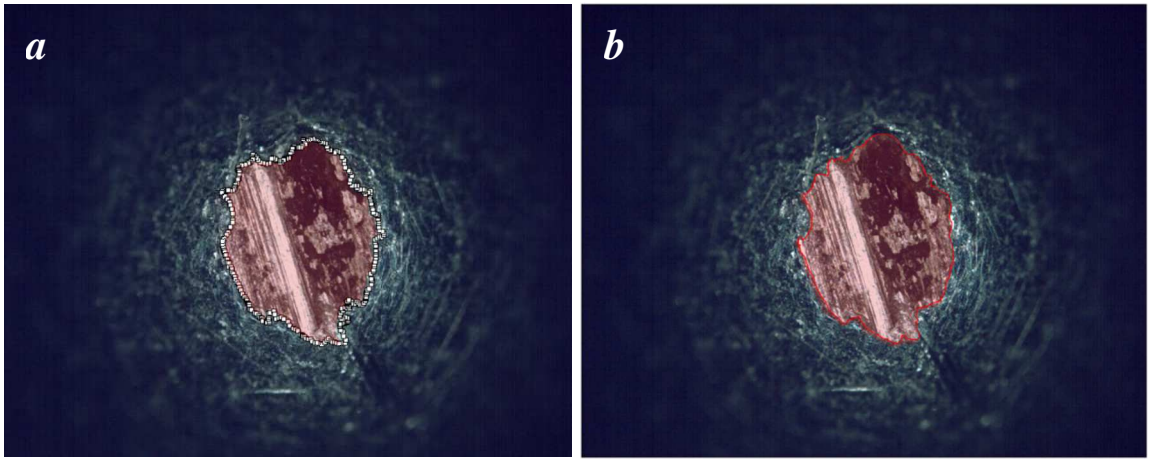



*Figure3.15*: optical microscope image at 5x magnification of test *Std.2*: (*a*) represents the polygonal selection of the worn area while (*b*) represents the elliptical one.

Once the above operations have been performed for each ball, it is possible to evaluate the average value of the wear rate $k$ to associate at each test; the relative wear rates are evaluated using *Formula 2.2*, which becomes through the appropriate substitution (*Formula 2.3*) as follows:

$$k = \frac{V}{F_z\,(2s \cdot f \cdot t_s)}$$

For the volume expression, consider the schematic draw in *Figure3.16*:

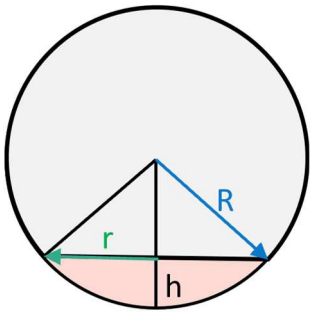



*Figure3.16*: schematic draw of a ball: the pink selection represents the eroded volume.

Calling $h = height\ of\ the\ spherical\ cap = R - \sqrt{R^2 - r^2} = R - \sqrt{R^2 - A/\pi}$, with $A$ = *worn area from the scar*, the worn volume has the following expression in terms of h:

$$V = \pi h^2 (R - h/3)$$

and in terms of A:

$$V = \pi(R - \sqrt{R^2 - A/\pi})^2(R - \frac{R}{3} + \frac{\sqrt{R^2 - A/\pi}}{3})$$
$$= \frac{\pi}{3}[2R^3 - \sqrt{R^2 - A/\pi}\ (2R^2 + A/\pi)]$$

For each ball, the associated error is calculated following the error propagation theory, accounting for time duration test and Fz error, and the standard deviation of the different measured areas, as previously done for the track profiles. The error on frequency and on the stroke is supposed to be negligible. Thus, the used formula is the following:

$$\delta k \approx \sqrt{\left|\frac{\partial k}{\partial V}\frac{\partial V}{\partial A}\delta A\right|^2 + \left|\frac{\partial k}{\partial F_z}\delta F_z\right|^2 + \left|\frac{\partial k}{\partial t_s}\delta t_s\right|^2}$$
$$= \sqrt{\left(\frac{\delta A}{V}\cdot\frac{A/\pi}{2\sqrt{R^2 - A/\pi}}\right)^2 + \left(\frac{\delta F_z}{F_z}\right)^2 + \left(\frac{\delta t_s}{t_s}\right)^2}\cdot k$$

As discussed above, the evaluated wear rate is independent of test duration, according to the wear rate definition, thus 100s and 300s duration tests can be considered together in calculating the average wear rate. A single representative value per condition is obtained using a weighted average and the associated error is evaluated following the error propagation theory. Operating in this way, the wear rate of different tribological conditions can be compared.

# 4. Set-up 1

## 4.1 Implementation of the standard set-up

Due to the mechanical constraints of the tribometer related to the centering of the ball holder (see section 3.7), specifically the required height of the flat sample, the 2 mm thick silicon substrate is too thin for the existing grabbing/insulating system. For this reason, the design of a new sample holder is necessary. To ensure the required height for proper positioning of the ball holder with respect to the sensor arms, a sample holder made of Delrin® polymer has been fabricated (*Figure4.1)*. The use of this support fulfils also the requirement of insulating the samples from the ground, necessary in order to be able to measure the generated tribo-voltage. Unfortunately, the other pole of the circuit, i.e. the Al ball, cannot be insulated from the ground for the mechanical design of the tribometer.

As shown in *Figure4.1a,* the lower block features precise holes in order to mount the whole sample holder to the base of the tribometer. On the upper block, instead, two holes are designed to accommodate metallic clamps for holding the sample in place (*Figure4.1c)*. To ensure proper alignment and stability, the clamps are parallelepipeds with notches that match the shape of the sample. In *Figure4.1b*, the upper block with the fixing clamps.

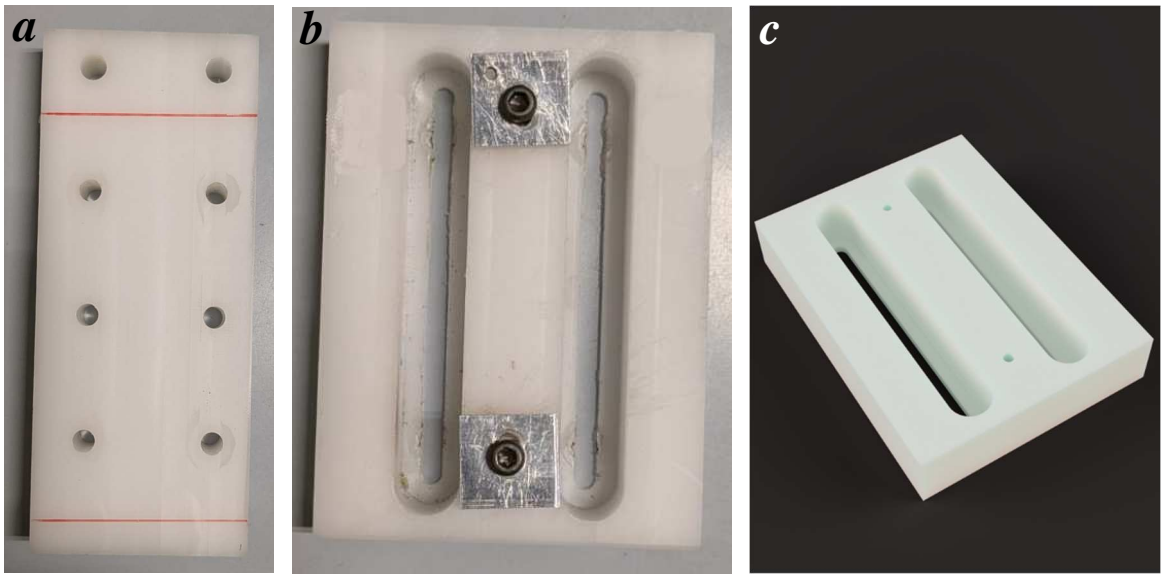


*Figure4.1:* image of the(*a*) lower block and (*b*) upper block of the set-up. (*c*) Designed rendering of the upper block.

Since it is necessary to acquire the voltage signal, the experimental setup must allow one cable to be connected to the substrate and another to the ball counterpart. To achieve this, the ground lead is used to collect the signal from the substrate; specifically, it is attached to an aluminum foil placed under the sample in order to gather all the generated charges (indicated by the green box in *Figure4.2)*. The hook tip, on the other hand, is connected to a secondary smaller cable, which is mechanically fixed to the ball holder using a screw (indicated by the yellow arrow in *Figure 3.2*).

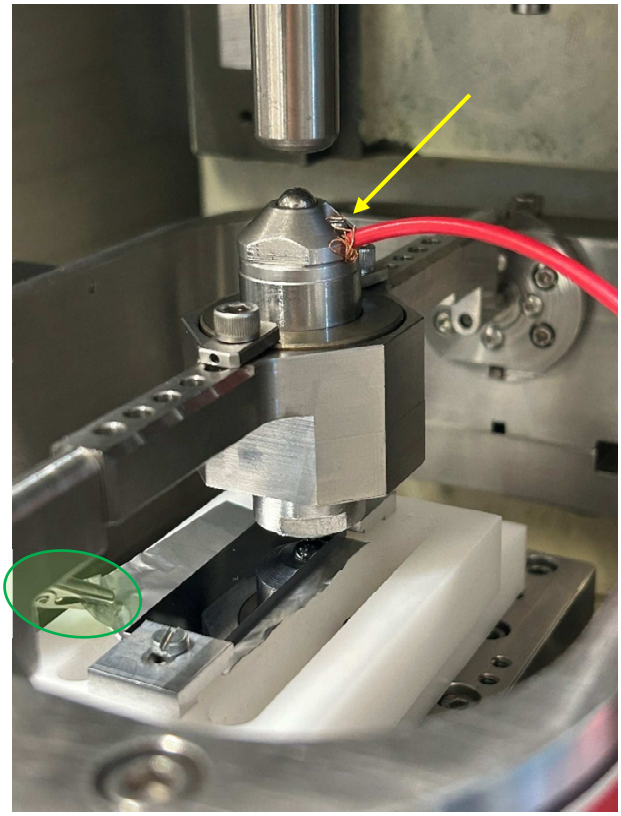


*Figure4.2*: the used set-up. The yellow arrow indicates the cable connected to the ball counterpart, while the green box contains the electrical connection to the Al foil.

The following drawing (*Figure4.3*) represents a scheme of the set up in reciprocating module:

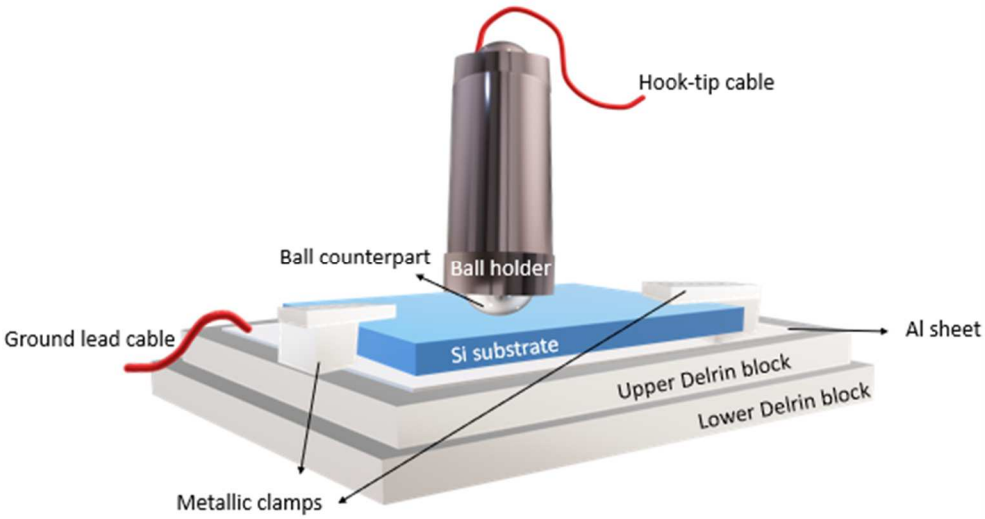



*Figure4.3*: schematic representation of the set-up.

## 4.2 Preliminary investigation of the tribo-electric properties of Al-Si pair

The first analyzed coupling was Aluminum ball against Silicon substrate (Al-Si).
In *Table4.1*, all the test conditions investigated with this set-up are relabeled:

| Denomination | Load [*N*] | Frequency [*Hz*] | RH [%] |
|---|---|---|---|
| *Std* | 20 | 0.5 | 55 |
| *Load30* | 30 | 0.5 | 55 |
| *Load40* | 40 | 0.5 | 55 |
| *Freq* | 20 | 1 | 55 |
| *lowRH* | 20 | 0.5 | 5 |

*Table4.1*: test conditions are listed with the set parameters

For all the tests, the time duration of the following steps of the recipe is maintained fixed:

1. Engagement step: 20s
2. Final part A: 30s
3. Final part B: 30s

Before starting with the measurements, preliminary tests were conducted to determine the optimal set-up parameters for the electrical circuit. The low noise pre-amplifier was configured with the following base settings:

- Coupling: DC
- Filter cutoff frequency: 1Hz
- Rolloff slope: -6Db/octave

The gain (on the pre-amplifier) and voltage range for acquisition (on the digital oscilloscope) were then adjusted based on the analysis of the preliminary tests to ensure both the measurement of a finite voltage signal and the maximization of resolution. During the tests, it was observed that significant electrical noise is generated when the ball is in contact with the sample, mainly when no load is applied. Furthermore, a strong negative peak appears when sliding begins. These behaviors result in overvoltage occurring unless a small gain and a large voltage range are selected. However, selecting a large voltage range needs an increase in gain during sliding in order to appreciate some periodicity. As sliding continues, the progressively increasing friction and the production of wear debris imply additional voltage spikes, leading to further overvoltage unless the gain is decreased.
To compromise between measuring a finite signal over the entire test, and detecting a periodicity also in the low-friction region, a fixed voltage range of 500 mV was set for all test condition; the gain was set to 1 during engagement step, then increased to 100 after the sliding start (or 50 for *Freq* condition) and it is no longer modified up to the test end. This recipe has been developed after many preliminary tests.

The set-up implementation enables the analyses of the tribological behavior between two counterparts, particularly the CoF value, and the electrical signal generated during the test (i.e. as a function of time).

In *Figure4.4*, the instantaneous CoF values and voltage signal for one typical test made in *Std* condition are plotted as a function of time, being a representative example of the observed behavior:

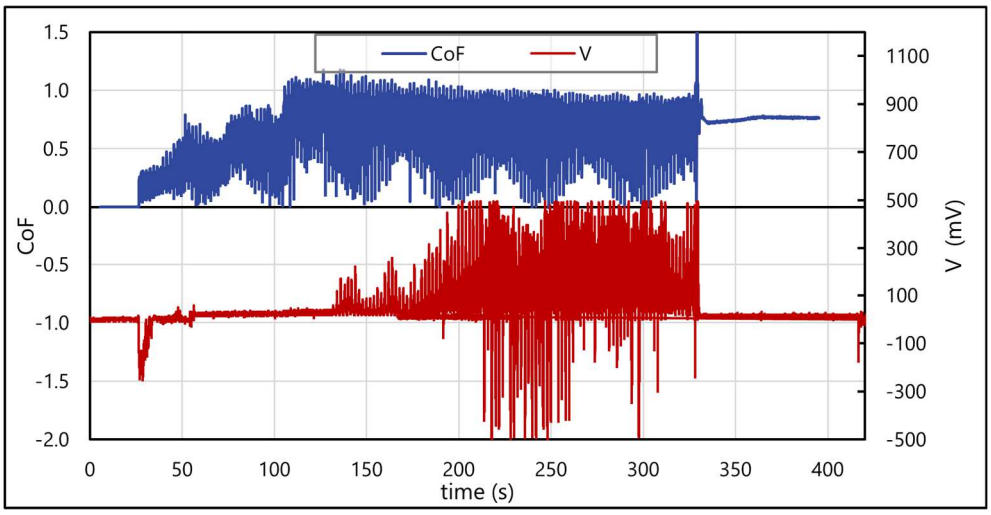



*Figure4.4*: Typical behavior of the CoF and voltage signal.

The upper graph highlights the evolution of the CoF during sliding motion. Through Matlab analysis, several distinct regions can be identified, each reflecting different tribological

behaviors, surface interactions, and material responses (see Matlab routine described in section 3.8):

- Region I: no friction

Corresponds to the pre-sliding phase, where the normal load is already applied but no relative motion occurs.

- Region II: initial sliding (running-in)

Represents the transition from static to dynamic contact. Initial deformation of the mating surfaces occurs. This stage is often characterized by transient frictional behavior.

- Region III: low-friction regime

A steady state where surfaces have adapted and particles formation may form a tribolayer, reducing direct asperity contact and stabilizing the CoF.

- Region IV: high-friction regime

Significant surface degradation and debris formation occur, leading to CoF increase.

*Figure4.5* illustrates the subdivision, which is delineated by the green lines.

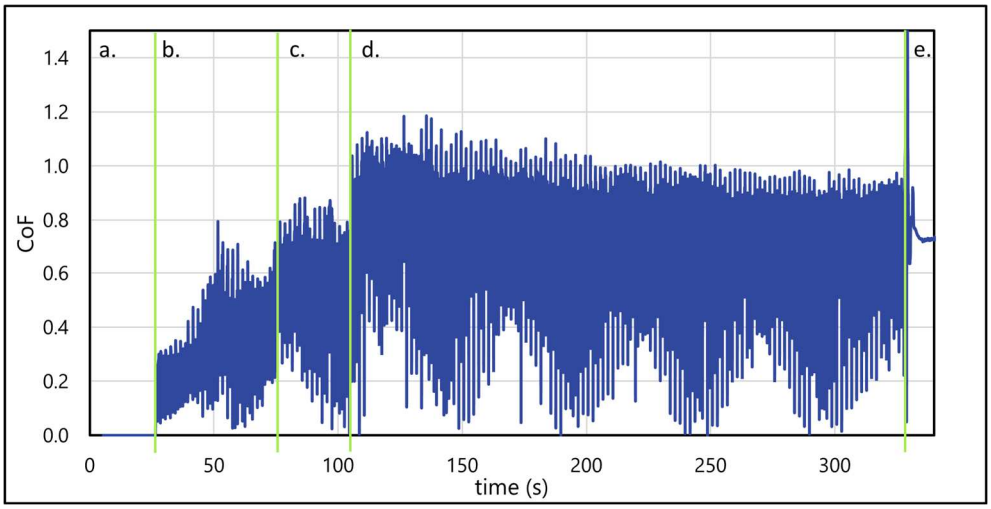



*Figure4.5*: Time division of the CoF, with regions defined by the Matlab code. a. no-friction b. running in c. low-friction d. high-friction e. end of the test.

Focusing on the behavior of the CoF, ideally it would be characterized by a peculiar shape shown in *Figure4.6*, since the reciprocating module is adopted: due to the nature of the motion, the CoF would show a flat portion in correspondence of the central part of the stroke where the speed is constant. When the system approaches the end of the stroke the velocity must decrease to reach zero before reversing direction, and then increase again in the opposite one: this translates in the curve with negative peaks.




*Figure4.6*: the ideal shape of the CoF.

However, the actual behavior exhibits spikes near the points where the direction of motion changes, both immediately before and after these reversal points, as shown in *Figure4.7*. This is attributed to variations of surface wear in those regions.
Additionally, it is possible to observe fluctuations or peaks in the CoF even in regions where it is expected to remain stable. These irregularities may be related to progressive wear of the contacting surfaces and the possible generation of debris.

In *Figure4.7* the actual behavior of the CoF is shown for few seconds of motion:

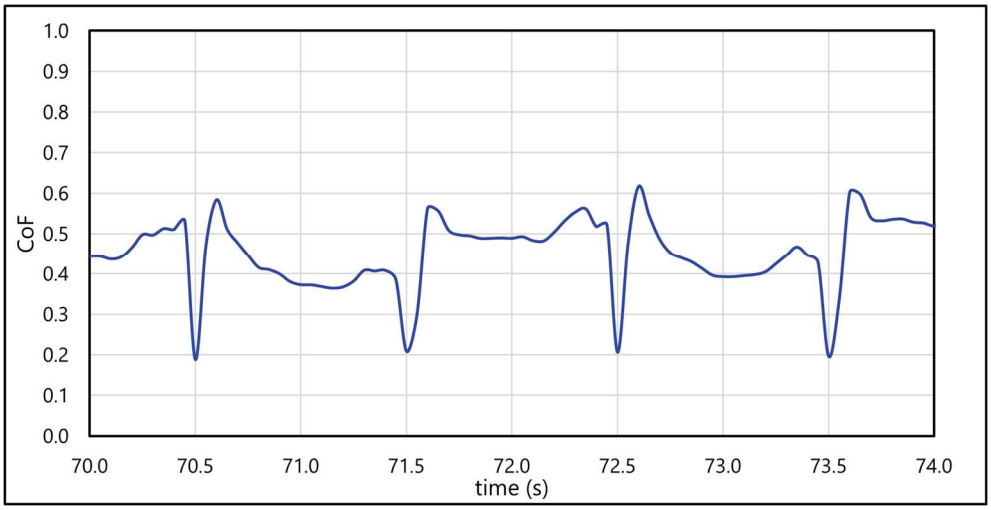



*Figure4.7*: real behavior of the CoF during Al-Si test (20N applied load, 0.5Hz sliding frequency, ambient humidity).

In certain tests the analysis of the wear track evidences an asymmetry along it, suggesting that the base was not perfectly parallel to the plane of motion. This leads to different average values of the CoF depending on direction of motion (forward-backward).
However, this issue is solved using a Matlab code, consisting in the calculation of the average value between the two opposite sliding passages.

The voltage signal measured in parallel is influenced by the contact phenomena at the interface. In *Figure4.8* an example of voltage signal acquired with this first set up is represented. Vertical lines indicate the temporal limits of the recipe steps.

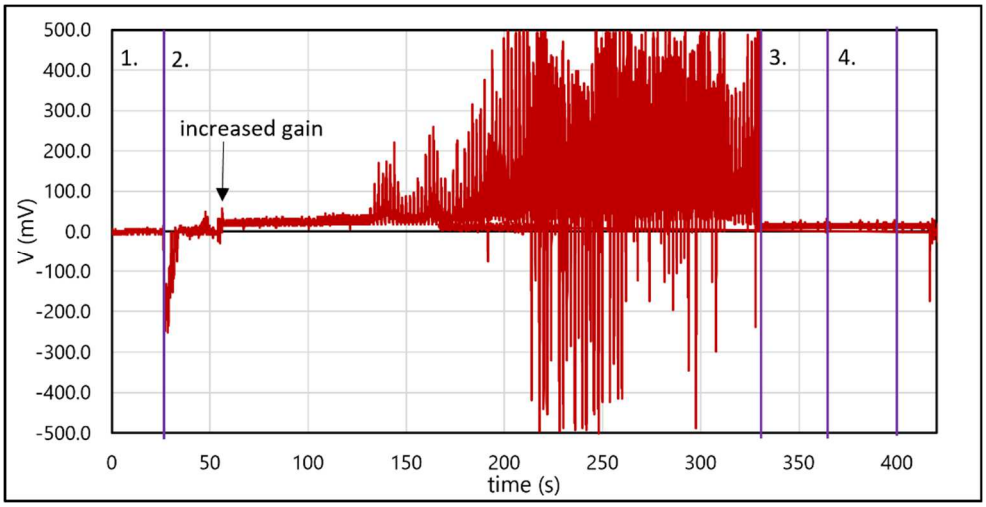



*Figure4.8*: Time division of the voltage signal, according to the used recipe. 1. Engagement 2. Sliding 3. Final part A 4. Final part B.

In the time instants preceding the engagement step, a largely noisy voltage signal is generated (data not shown) given by the unstable mechanical contact of the two counterparts, with no load applied. For this reason, no gain (i.e. gain level = 1) is applied here, to avoid overvoltages obscuring the next passages. During the engagement step (region 1), the real mechanical contact is achieved, so charge transfer between the two surfaces can occur (contact electrification): this leads to constant voltage signal. As already mentioned, the value of CE is influenced by differences in work function, material conductivity, and surface roughness. In the present activity, due to the limited resolution of the set-up, the CE signal is indistinguishable from the background noise. The start of sliding motion (region 2) is featured by a negative voltage spike, in some cases: this transient behavior may result from the disruption of thin oxide films on the surface of the silicon wafer, causing a sudden shift in the contact potential difference. After this initial transient, voltage stabilizes, indicating a steady tribological regime with consistent charge generation mechanisms. At this point, the gain is increased according to the selected configuration. As expected, the voltage is characterized by DC signal both for forward and backward motions. Since reciprocating module is exploited, its shape is characterized by a sequence of peaks, each corresponding to one relative slide between the two counterparts.
*Figure4.9* shows the acquired voltage curve: in this case, the gain and the voltage range are optimized in order to appreciate the features in a short range of time.

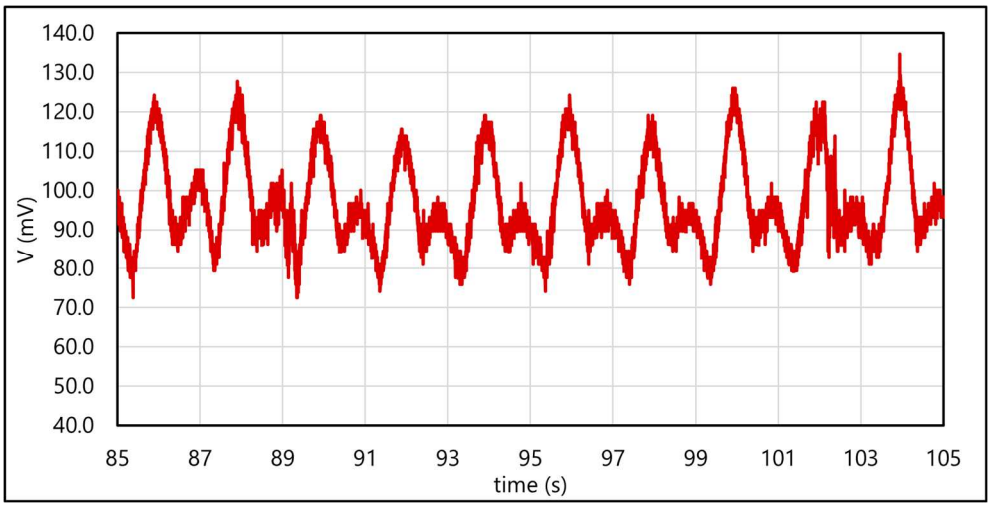



*Figure4.9:* voltage curve as a function of time in a *Std* test, done to appreciate the features. Thus 200 gain and voltage range of ±200mV are set and only 30 seconds of motion are shown.

In each period (i.e., 2 seconds in this *Std* condition), two voltage peaks are observed, corresponding to the forward and backward sliding motions. The asymmetry between the two peak amplitudes suggests a possible misalignment between the contacting surfaces. This could be attributed to a slight tilt, resulting in different contact conditions depending on the sliding direction, similarly to CoF issue (*Figure4.10).*

However, a more in-depth analysis of the phenomenon requires a longer temporal window (100-300s). Consequently, the gain/voltage range settings need to be adjusted, which prevents such a high resolution of all the signal features. For this second case, a typical signal is shown in *Figure4.10*, where the reduced resolution is clearly visible.

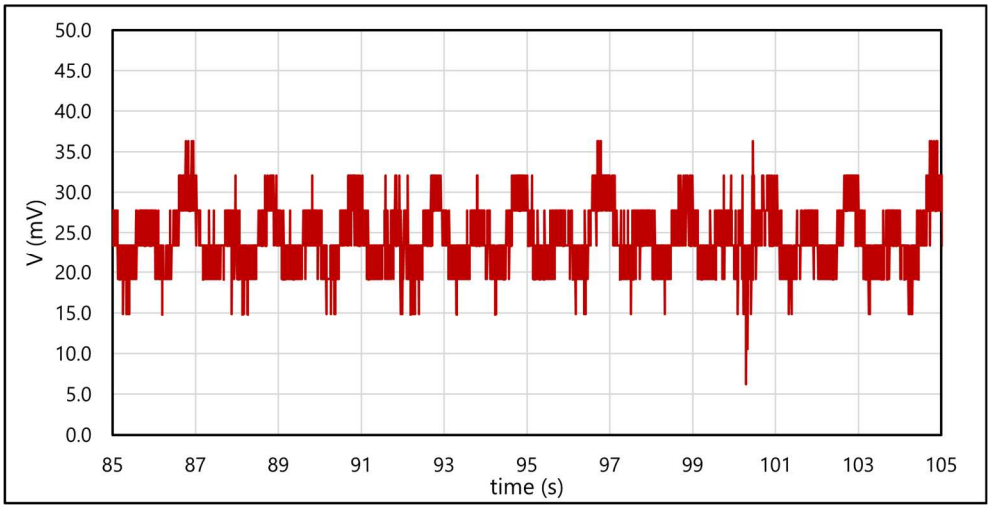



*Figure4.10:* voltage curve as a function of time in a *Std.1* test.

Despite the lower resolution, the peaks are still recognizable.
As presented in the next chapters, the further modification of the set-up strongly improve the resolution of the voltage signal.

In test 300s long, after typically 100-150s, the voltage peaks intensity increases. This could be due to enhanced wear in both the counterparts. At certain point, overvoltages arise, reflecting extreme tribological conditions where CoF values approach 1.
The last section corresponds to the disengagement phase. In this step, the sliding motion ceases, and the tribometer head has 30 seconds to return to the nominal static load (region 3), followed by an additional 30 seconds of steady load (region 4).
To evaluate the quantitative values in the regions defined by the Matlab code, the dedicated Excel template is used (see section 3.8)

### 4.2.1 Tribological characterization: coefficient of friction measurement

Since the tribological properties of the Al-Si pair are expected to be strictly connected to the outcoming tribovoltage, friction and wear of both the Si substrate and the Al ball have been estimated, and compared with the corresponding generated voltage.
As discussed above, a Matlab script is employed to divide the CoF in distinct regions and to calculate their average values. Considering the evolution of the CoF during sliding (running-in, low friction and high friction), the following graphs represent the different CoF values for each region and test.

Focusing on the *Std* condition, *Figure4.11* shows the CoF average values extracted via Matlab. The first three tests (*Std.1, Std.2, Std.3*) correspond to 100-second tests, while *Std.4*, *Std.5*, and *Std.6* refer to 300-second tests.

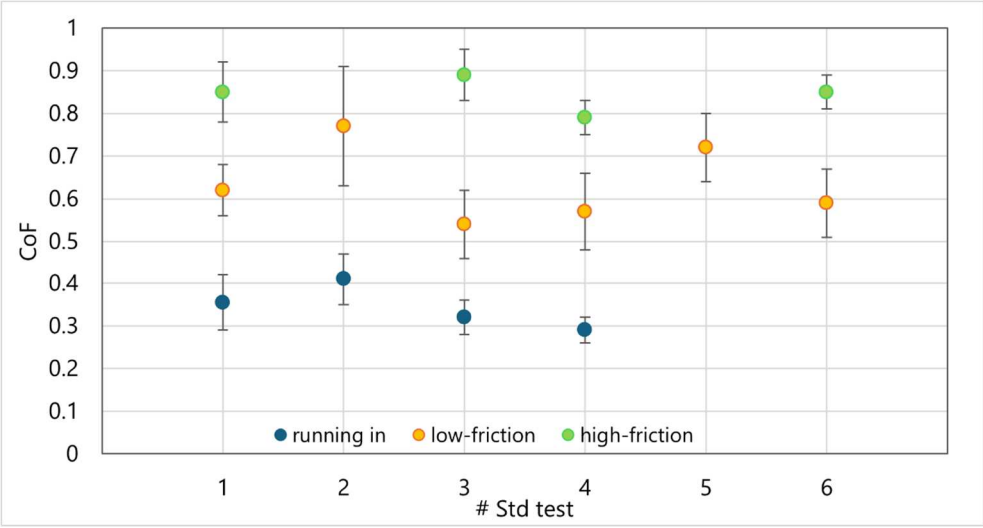



*Figure4.11*: CoF average values extracted via Matlab are reported for each *Std* test.

For each region, running-in, low friction, high friction, a CoF average value is extracted using weighted average and the corresponding error δCoF when the values are compatible within the error bars. As will be discussed in more detail in chapter 5, fluctuations in the

load, which became increasingly evident during the experimental campaign, led to the exclusion of some tests from the final average calculations, particularly those where such variations are most pronounced: *Std.5, Std.6, Freq.1, Freq.2, lowRH.2.*
The same calculations are performed for the other four conditions: *Load30*, *Load40*, *Freq*, *lowRH*. *Figure4.12* provides a rapid visualization of the average CoF and the associated error extracted via Matlab.

Notice that for *Load40* condition, only three tests are performed since instabilities in Fz signal occur with load of 40N: *Load40.1, Load40.2* are 300sec tests, while *Load40.3* is 100sec test.

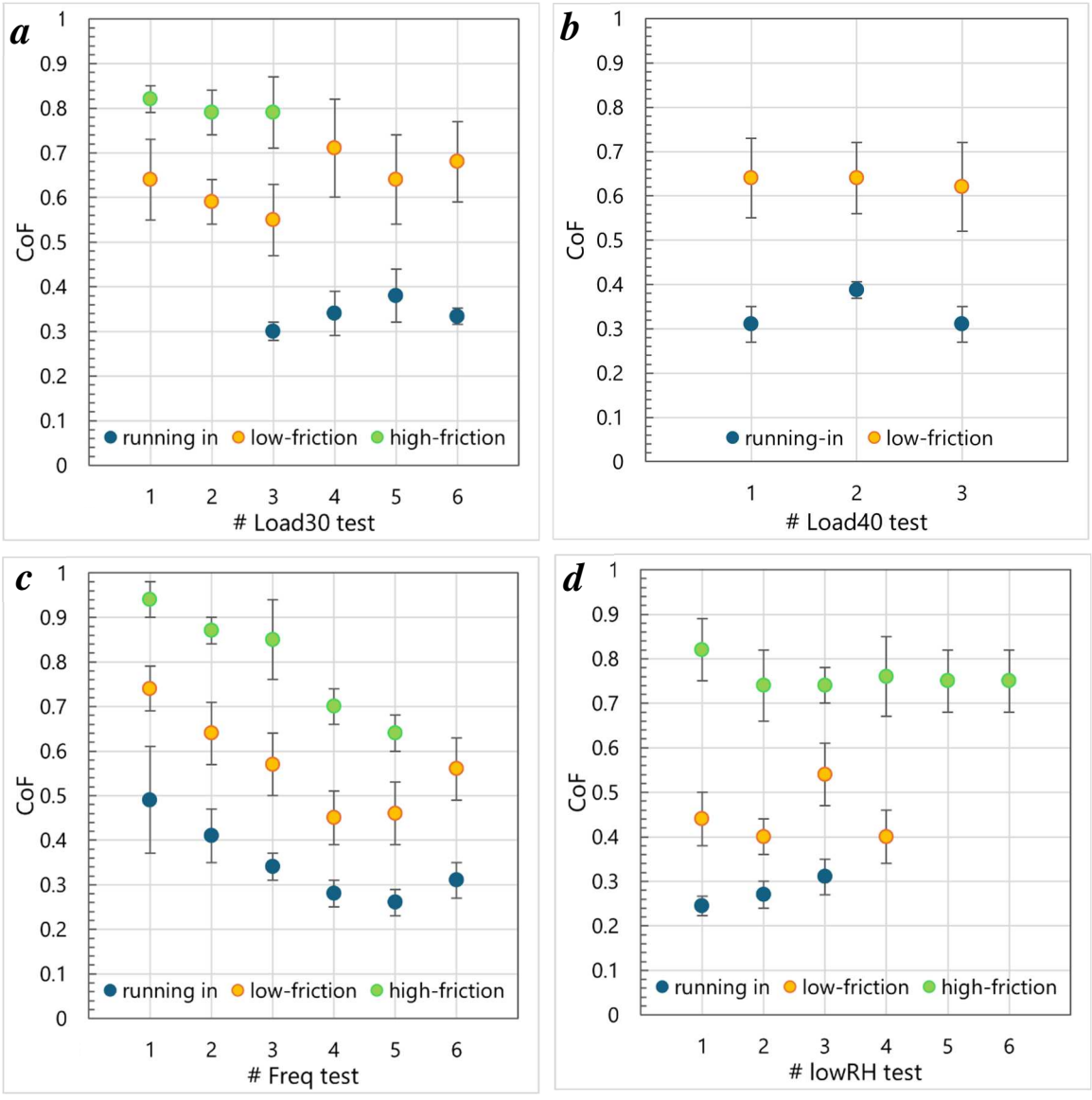



*Figure4.12*: CoF average values extracted via Matlab are reported for all (*a*) *Load30*, (*b*) *Load40*, (*c*) *Freq*, (*d*) *lowRH* tests.

To explicitly show the dependence of the CoF on different tribological parameters (load, frequency, humidity), the above shown plots are summarized in figures below, together with the corresponding in *Std* condition.

In *Figure4.13* the CoF as a function of the load is shown:

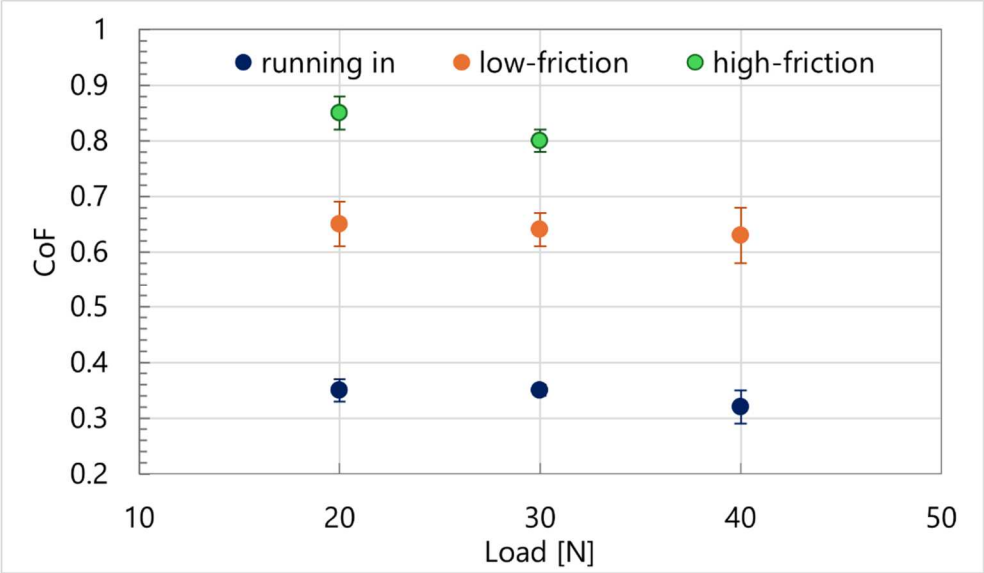



*Figure4.14*: CoF average values calculated for each tribological region are reported for *Std*, *Load30*, *Load40* tests.

Within the error bars, the CoF doesn't show a significant dependence on the applied load in any tribological regions. The only noticeable difference is that, under higher load conditions, the CoF doesn't reach the high-friction regime (i.e., values close to 0.8); however, this observation cannot be considered conclusive due to the limited statistical data.

As previously done for the load, the dependence of the CoF on the sliding frequency is also investigated. In this case, the frequency varies between 0.5 Hz and 1 Hz, while keeping all other tribological parameters constant. The corresponding analysis is presented in *Figure4.15*.

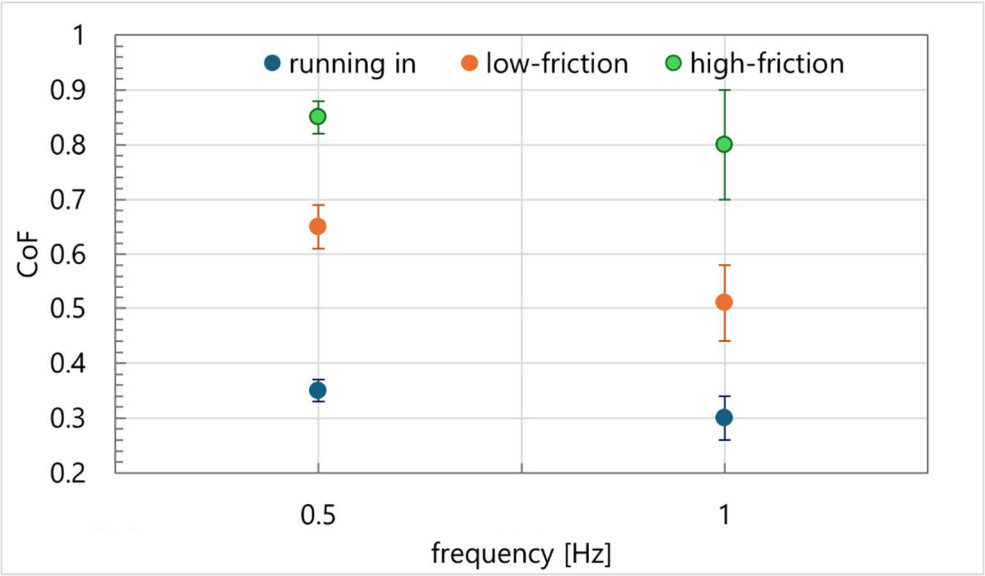



*Figure4.15*: CoF average values calculated for each tribological region are reported for *Std*, *Freq* tests.

The difference between the two conditions is visible only in low-friction regime, while in the other case, the resulting CoF are compatible within the error bars.

The same procedure is applied to investigate the influence of relative humidity on the CoF. In this study, tests are carried out under two different conditions: ambient humidity (~55%) and low humidity (~5%). In *Figure4.16* it is possible to compare the results:

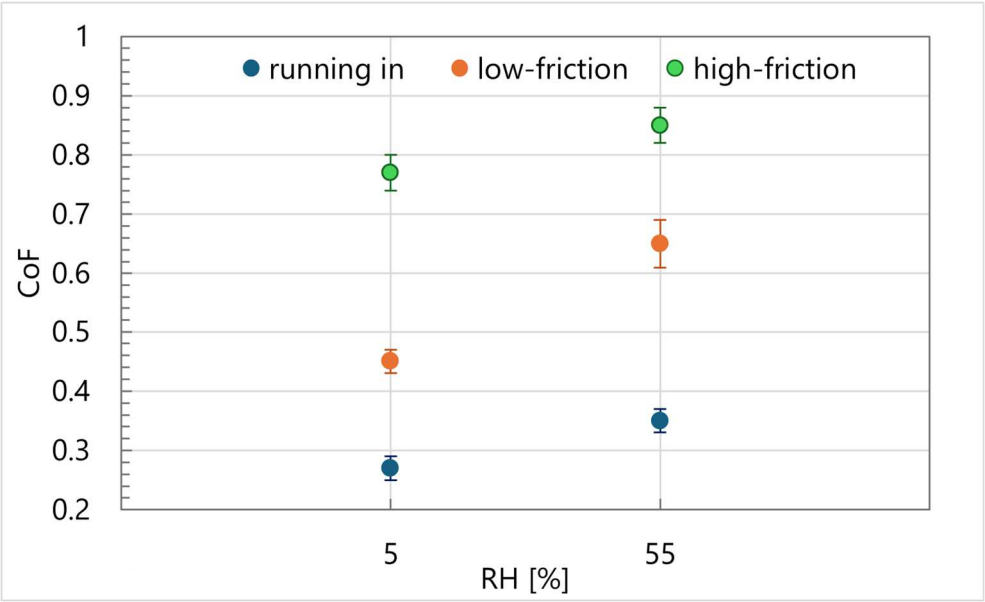



*Figure4.16*: CoF average values calculated for each tribological region are reported for *Std*, *lowRH* tests.

Compared with the previous cases, the dependence on relative humidity appears more evident. In all the identified regions, the CoF values are higher under higher humidity conditions.

From this first set of tests, it can be inferred that the CoF shows a clear dependence on the relative humidity of the environment. In contrast, no significant dependence is observed with respect to the applied load or sliding frequency.

In the end, all test conditions results in a running-in phase with $CoF \lesssim 0.4$, a low-friction regime with CoF in the range $\sim [0.4;\ 0.75]$ and a high-friction one with $CoF \gtrsim 0.75$.

### 4.2.2 Morphological characterization: wear rate evaluation

Another important parameter that contributes to evaluate the tribo-electrical performance of the system is the wear rate, both of the track of the flat counterpart and on the ball.
The stylus profilometer is used to compare the wear rates of the tracks, while the ImageJ analysis on the optical microscope images allows the comparison of the ball wear rate.

**Silicon substrate**

The wear tracks profiles are measured in order to evaluate their changes in topography. A single representative value of the wear rate per condition is calculated, to compare different conditions and identify possible correlations.

In *Figure4.17* and in *Table4.2*, the wear rates as a function of the tribological condition are summarized.

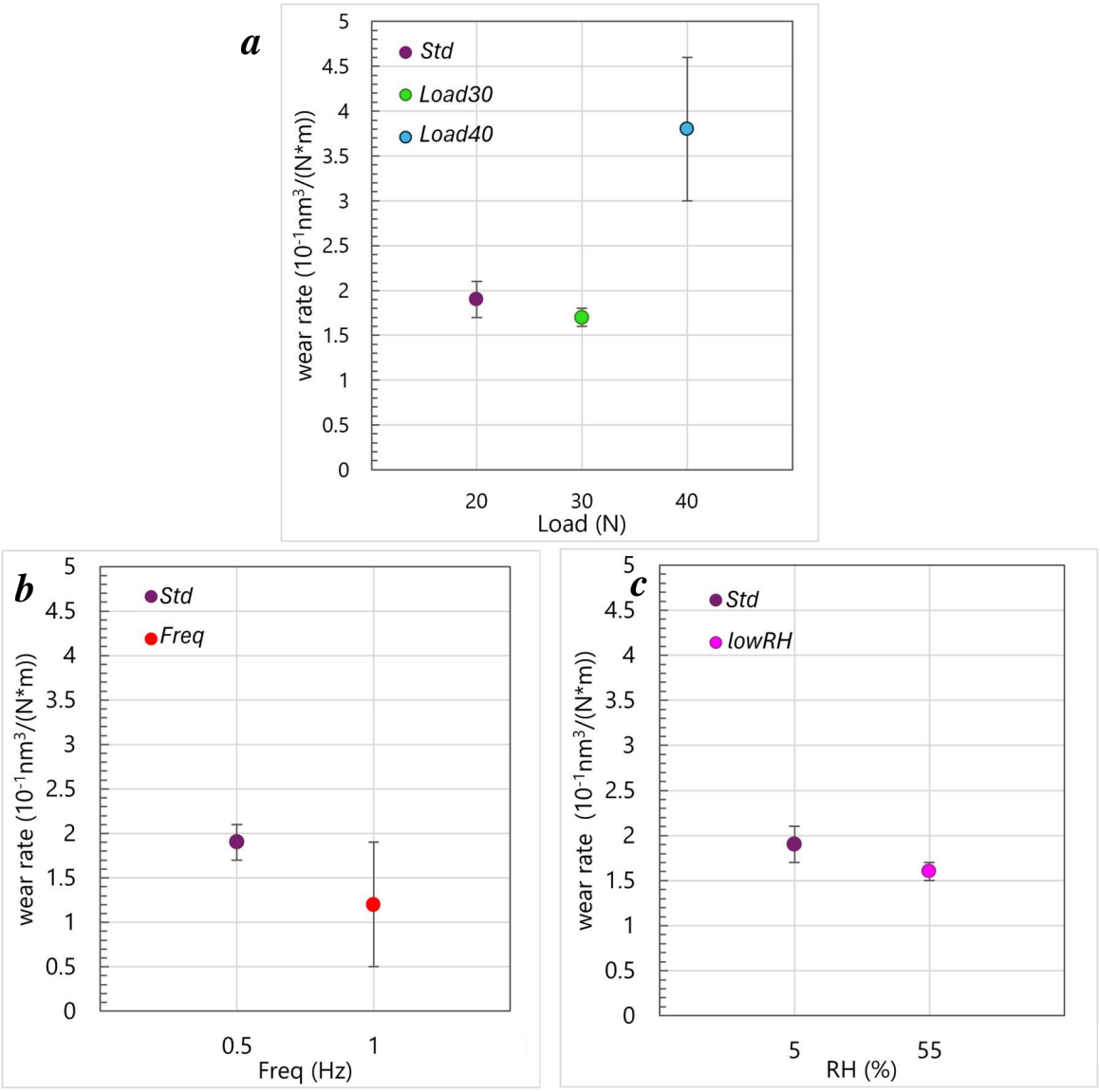



*Figure4.17*: wear rates of Silicon substrate as a function of the (*a*) applied load, (*b*) sliding frequency and (*c*) relative humidity.

**Wear rate on Silicon substrate ($10^{-1}nm^3/(N*m)$)**

| Load | | Freq | | RH | |
|---|---|---|---|---|---|
| 20N | (1.9 ± 0.2) | 0.5Hz | (1.9 ± 0.2) | 5% | (1.9 ± 0.2) |
| 30N | (1.7 ± 0.1) | 1Hz | (1.2 ± 0.7) | 55% | (1.6 ± 0.1) |
| 40N | (3.8 ± 0.8) | | | | |

*Table4.2*: wear rates of Silicon substrate as a function of the applied load, sliding frequency and relative humidity.

From the comparison, no significant variations are observed within the error bar range considering changes in frequency and humidity. In contrast, increasing the applied load up to 40 N (test *Load40N*) results in a noticeably higher estimated wear rate, whereas at 30 N

(test *Load30N*) this increase is not appreciable. This finding contrasts with the CoF measurements, which do not indicate a high-friction regime at 40 N.

### Ball counterpart

Focusing on the spherical counterpart, the ImageJ software is used.
Through the optical microscope the images of the ball scar are taken, and their removed volumes are evaluated, calculating the worn area. To compare different conditions, one representative value per condition is obtained using a weighted average.

In *Figure4.18* and in *Table4.3*, the wear rates of the spherical counterparts as a function of the tribological condition are summarized.

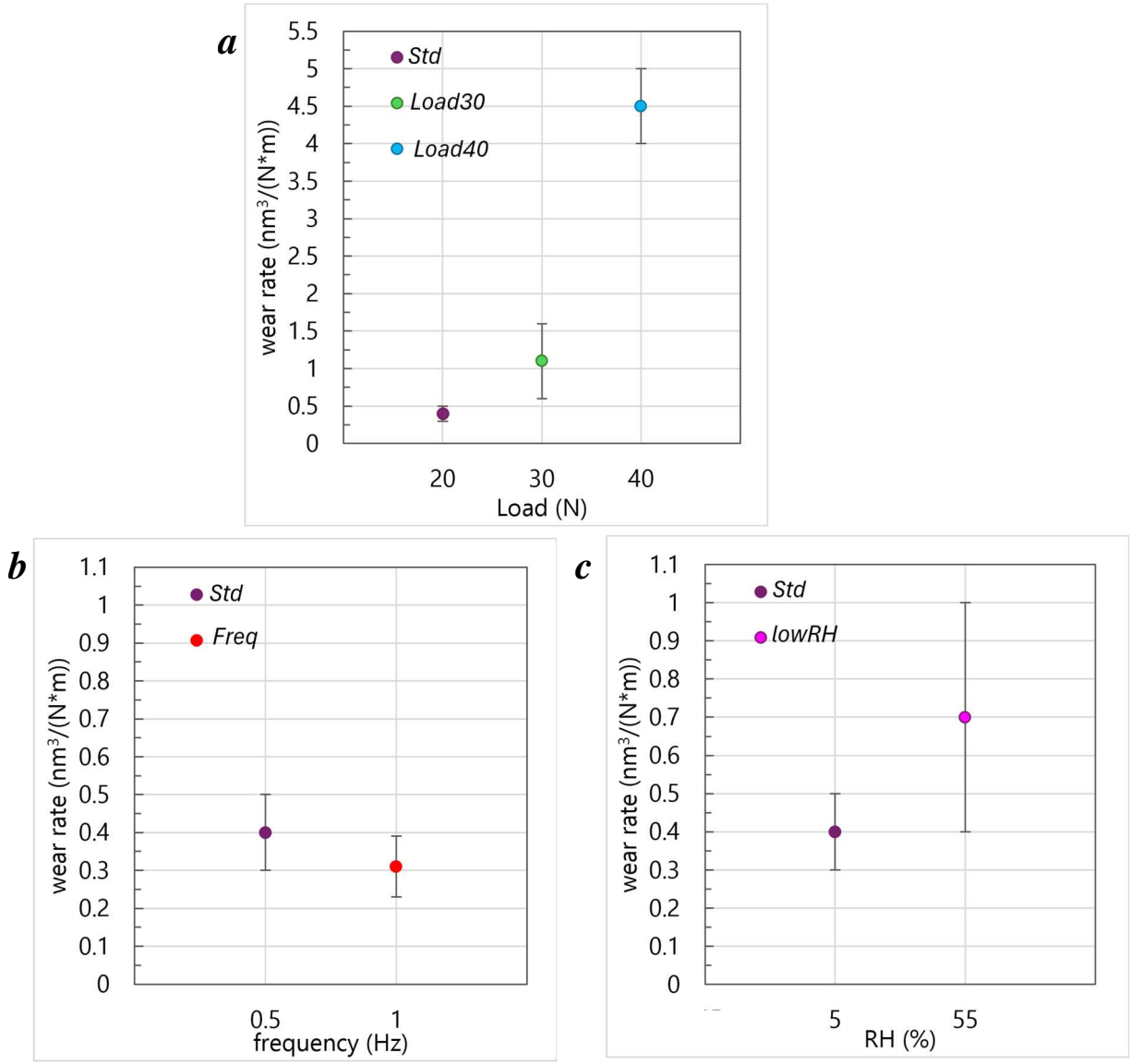



*Figure4.18*: wear rates of Al ball as a function of the (*a*) applied load, (*b*) sliding frequency and (*c*) relative humidity.

**Wear rate on Silicon substrate ( $nm^3/(N*m)$)**

| Load | | Freq | | RH | |
|---|---|---|---|---|---|
| 20N | (0.4 ± 0.1) | 0.5Hz | (0.4 ± 0.1) | 5% | (0.4 ± 0.1) |
| 30N | (1.1 ± 0.1) | 1Hz | (0.31 ± 0.08) | 55% | (0.7 ± 0.3) |
| 40N | (4.5 ± 0.5) | | | | |

*Table4.3*: wear rates of Silicon substrate as a function of the applied load, sliding frequency and relative humidity.

As inferred from the wear track analysis, also for the ball the wear rate does not appear to depend on frequency or humidity under the conditions investigated, considering the error bars. In contrast, variations in load do affect the ball's wear: an increase in applied load leads to a corresponding increase in wear rate, particularly approaching load = 40N. Thus, the same considerations made for the wear rate on the Si substrate can be also extended to the wear of the Al ball.

### 4.2.3 Morphological characterization: EDX

The tribological analysis conducted so far has highlighted a progressive evolution of the CoF throughout the duration of the tests, accompanied by evident debris formation in both the 100s and 300s test duration. In order to investigate the origin of the observed wear debris and to identify which of the two mating surfaces contributed to its formation, an Energy Dispersive X-ray Spectroscopy (EDX) analysis is performed on both counterparts, in *Std* condition tests. This compositional analysis enables the identification of the elements associated with the debris particles and the worn area, thereby providing insight into the dominant wear mechanism and the material removal process occurring during sliding.
*Figure4.19* shows the surface of the wear region on the ball counterpart, acquired using two different imaging techniques:

- An optical microscope at 5× magnification, providing a general overview of the worn area;
- A Scanning Electron Microscope (SEM) at 100× magnification, using a backscattered electron detector and an incident electron beam of 25 kV; in *Table4.4* the morphological informations, as the atomic percentual, are displayed.

These are related to *Std.2*, a 300s test.

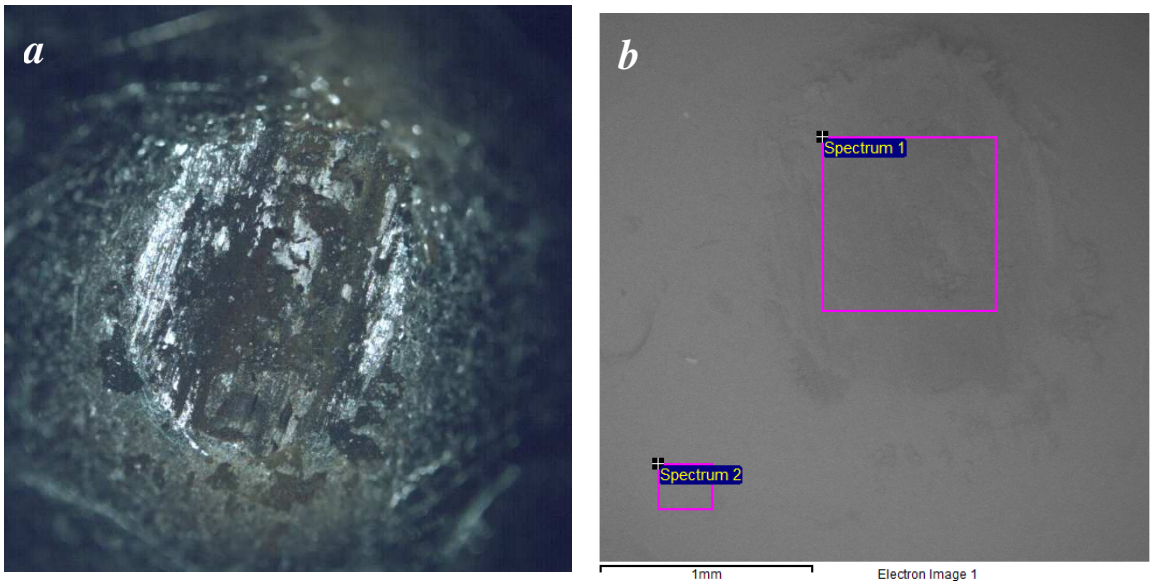



*Figure4.19*: image of the ball scar related to test *Std.2* taken (*a*) with optical microscope (5X magnification) and (*b*) with SEM (100X magnification, BSE detector).

*Figure4.19a* confirms that the motion corresponds to a pure sliding mechanism without rotation of the ball during the test, as evidenced by the circular shape of the worn area. Debris formation is also observed both within the wear track and along its edges, but this is clearly visible even to the naked eye

In the SEM image, the regions selected for compositional analysis are indicated by pink squares: *Spectrum 1* corresponds to the central area of the wear region, while *Spectrum 2* refers to the pristine surface.

*Figure4.20* and *Figure4.21* reports the EDX spectra associated with both regions, where the detected elements are identified by their characteristic peaks. The intensity of each peak is proportional to the relative abundance of the corresponding element within the analyzed area.

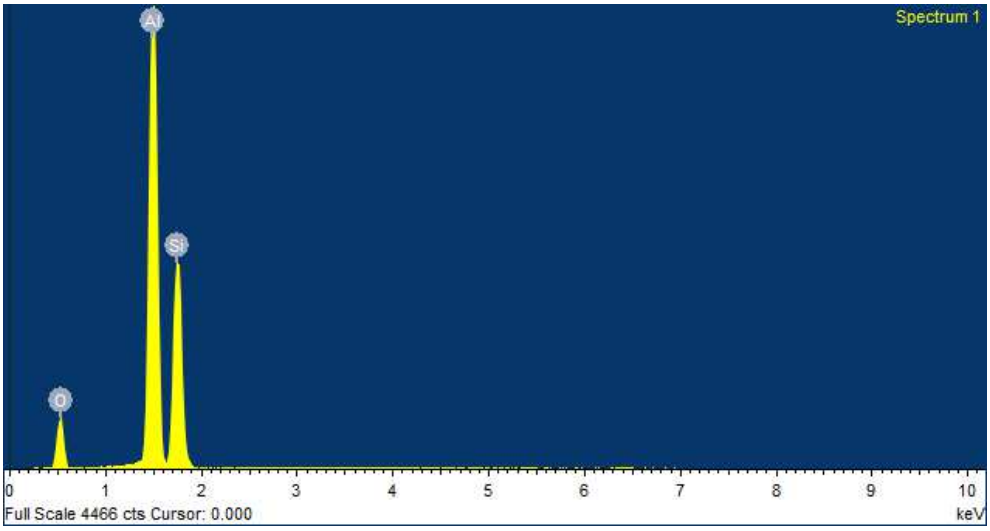



*Figure4.20*: EDX spectrum related to *Spectrum 1* of the ball scar.

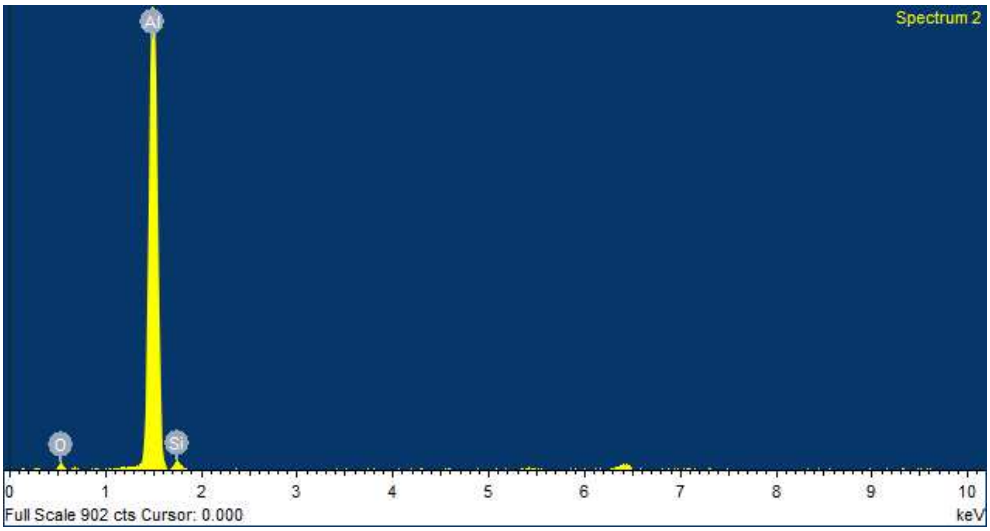



*Figure4.21*: EDX spectrum related to *Spectrum 2* of the ball scar.

In *Table4.4* the elements percentages are listed for each spectrum:

| | Element atomic % | | |
|---|---|---|---|
| | O | Al | Si |
| *Spectrum 1* | 42.63 | 31.8 | 25.57 |
| *Spectrum 2* | 15.47 | 79.98 | 4.55 |

*Table4.4*: atomic percentages of the elements in all the spectrum, evaluated by EDX technique.

From the EDX data, it can be inferred that Silicon of the other counterpart is transferred to both the wear region and the pristine surface, with a higher concentration where contact occurs.

Surface oxidation is observed in both areas, although it is more pronounced within the contact region.

Focusing now on the wear track on the Si substrate, *Figure4.22* shows the relative optical microscope image (with 5X magnification) and the SEM image (at 150X magnification, using a backscattered electron detector and an incident electron beam of 25 kV).

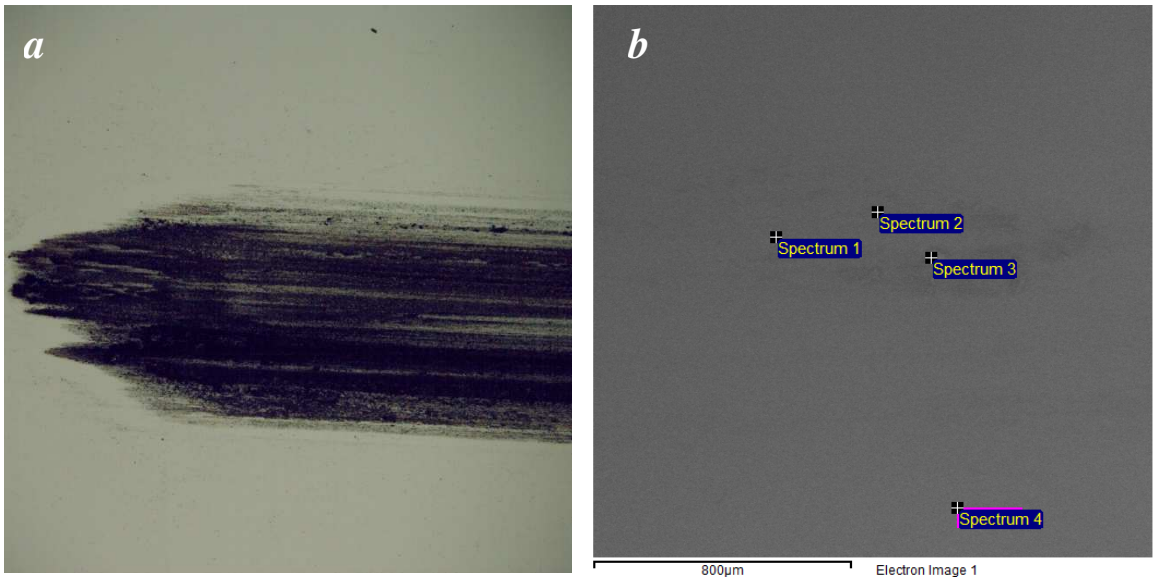



*Figure4.22*: image of the wear track related to test *Std.2* on Si substrate taken (*a*) with optical microscope (5X magnification) and (*b*) with SEM (150X magnification, BSE detector).

*Figure4.22a* is acquired near the edge of the sliding track. The difference in color between the pristine surface and the wear track suggests variation in surface chemistry. Debris formation is also evident, both within the wear track and along its edges, but this is clearly visible even to the naked eye.

Although the SEM image (*Figure4.22b)* doesn't provide strong contrast, several regions are selected for EDX chemical analysis and are indicated by pink squares or crosses: *Spectrum 1* corresponds to the central area of the wear region and *Spectrum 2* refers to its edge, *Spectrum 3* is related to one visible debris, while *Spectrum 4* corresponds to the pristine surface.

*Figure4.23*, *Figure4.24, Figure4.25*, *Figure4.26* report the EDX spectra acquired from all the indicated regions. The detected elements are identified by their characteristic peaks and, as previously discussed, their intensity is proportional to the relative abundance of the corresponding element within the analyzed area.

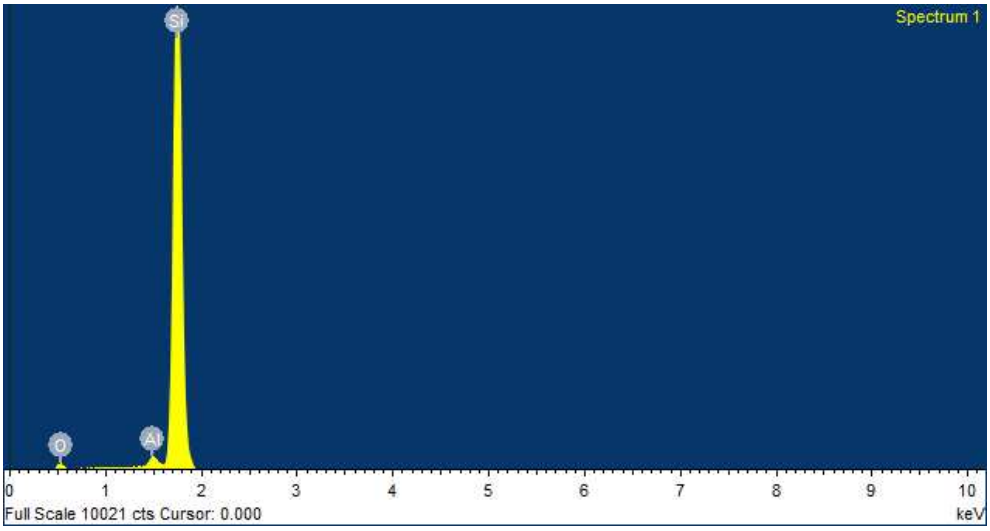



*Figure4.24*: EDX spectrum related to *Spectrum 1* of the wear track on Si substrate.

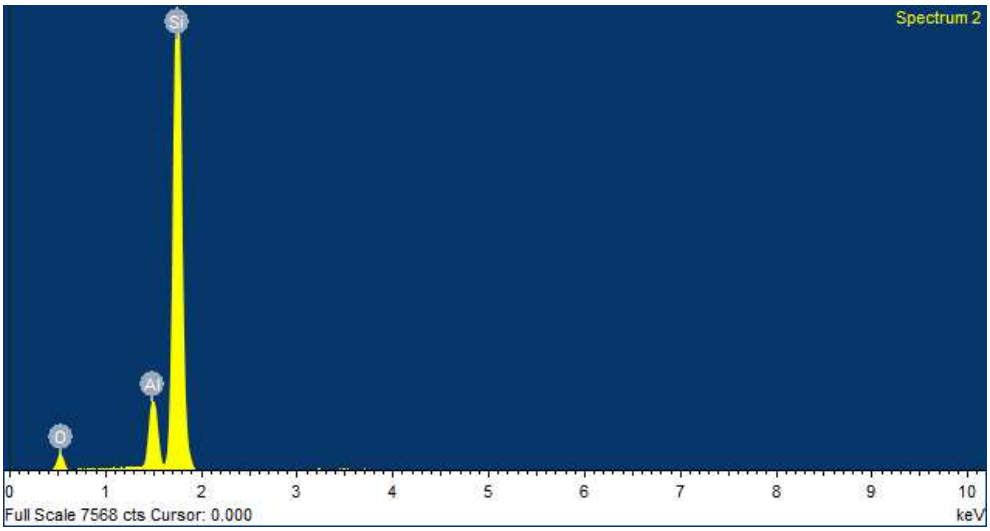



*Figure4.24*: EDX spectrum related to *Spectrum 2* of the wear track on Si substrate.

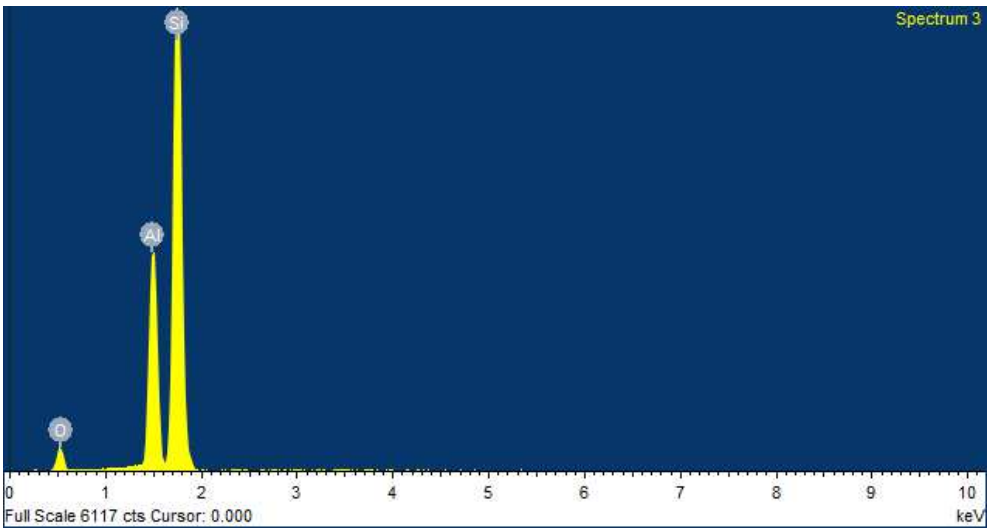



*Figure4.25*: EDX spectrum related to *Spectrum 3* of the wear track on Si substrate.

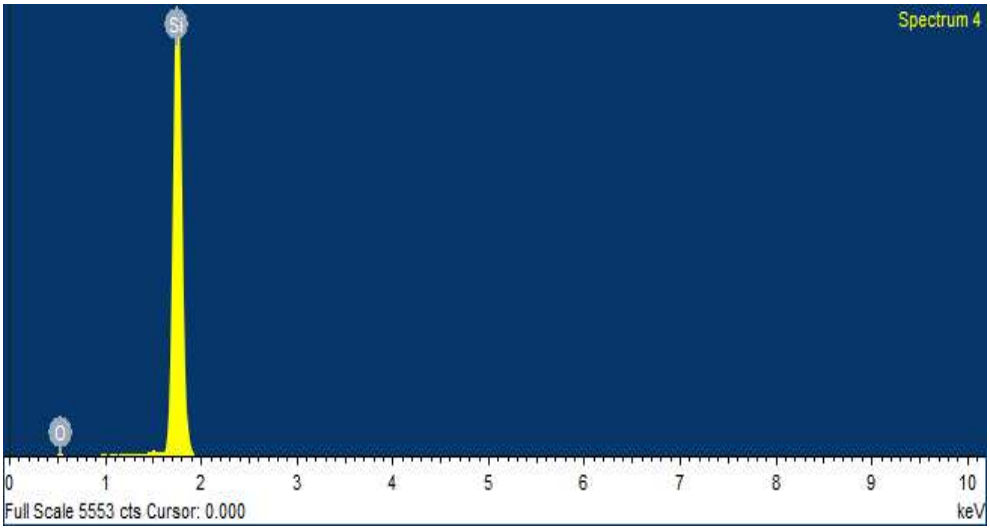



*Figure4.26*: EDX spectrum related to *Spectrum 4* of the wear track on Si substrate.

In *Table4.5* the elements percentages are listed for *Spectrum 1*, *Spectrum 2, Spectrum 3, Spectrum 4*:

| | Element atomic % | | |
|---|---|---|---|
| | O | Al | Si |
| *Spectrum 1* | 18.50 | 1.40 | 80.10 |
| *Spectrum 2* | 30.61 | 7.50 | 61.89 |
| *Spectrum 3* | 30.33 | 16.84 | 52.84 |
| *Spectrum 4* | 7.86 | 0 | 92.14 |

*Table4.5:* atomic percentages of the elements in all the spectrum, evaluated by EDX technique

Aluminum appears to be transferred across the entire wear track, as confirmed by the spectra acquired in both *Spectrum 1* and *Spectrum 2*. The debris particle analyzed (*Spectrum 3*) seems to be primarily composed of Silicon and its oxide, indicating material removal from the analyzed substrate. *Spectrum* 4 confirms that the sample is composed of Silicon and reveals slight Oxygen signal, suggesting the presence of a thin oxide layer on the surface, which is less significant than the one inside the track.

As for the 100s test, Si transfer is already detectable, although with a lower concentration due to the shorter test duration.

### 4.2.4 Electrical characterization: tribovoltaic effect

In this section, the voltage generated during tribological tests is analyzed with the aim of correlating it with the mechanical parameters, load, sliding frequency and relative humidity, and wear mechanism of the contact pair.
The initial part of section 4.2 introduces the evolution of the voltage signal over time in qualitative terms. Here quantitative analysis is discussed. To ensure reliable data interpretation, the raw voltage signals are post-processed using dedicated analysis templates, described in section 3.8. This tool allows the extraction of statistical parameters, such as the average and the maxima average with the corresponding error and the absolute maxima. In *Figure4.27*, one complete voltage signal is represented:

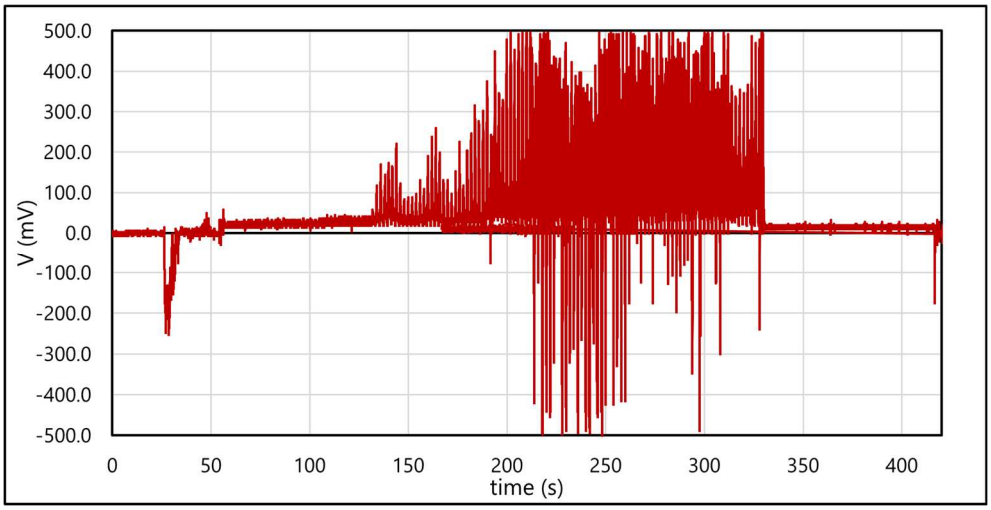



*Figure4.27*: voltage signal as a function of time. This is related to test *Std.1*

The plot shows that, aside from the initial part of the sliding, the voltage signal exhibits strong fluctuations and reaches overvoltage levels early in the test.
The overvoltages occurring early during sliding and some incompatibility between the tribovoltage averages mainly between *Std* tests, arising from the analysis of the data, may indicate a potential malfunction or misconfiguration within the electrical circuit, possibly resulting in a high noise-to-signal ratio. Consequently, additional investigations are conducted to verify the correct operating mode of the measurement system, as discussed in the chapter 5.

The issue is related to the calibration of the pre-amplifier, because it has an internal offset that varies from day to day and depends on the gain settings. This offset has been evaluated in the next chapter to be of the same order of magnitude (sometimes one order higher) as the generated tribovoltage. The dedicated Excel template accounts for the possible presence of an offset by shifting all data based on a reference value determined from the engagement step, where contact between the surfaces is well established and tribovoltage generation has not yet started. However, due to the fact that the engagement step is acquired with a different gain compared to the sliding step, this offset correction is not accurate. As a result,

it is not possible to determine a precise average voltage for each test condition, but only to estimate its overall behavior and order of magnitude.

Let us consider the average voltages computed by the Excel template for each region identified in the Matlab analysis. Starting from the *Std* condition, the corresponding values are displayed in *Figure4.28*. Overvoltage values are excluded, as they do not provide meaningful information for the analysis. Similarly, data from the running-in phase are not included because this phase is sometimes very short and could coincide with the period before gain adjustment (*Figure4.8*), resulting in gain value =1, which is different from the set one during the low-friction and high-friction regimes (i.e gain = 50 or 100, depending on the condition).

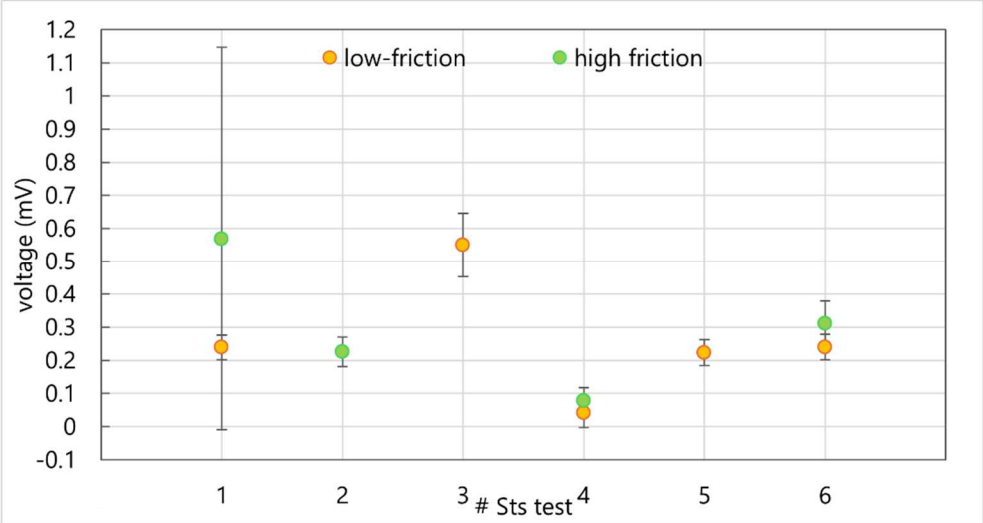



*Figure4.28*: average values of the voltage divided in running in, low-friction and high-friction.

Considering the error bars, no significant differences are observed between the average voltages across the three regions within each test: this suggests that changes in the CoF do not significantly affect the voltage. Therefore, a single representative voltage value per test is extracted by computing a weighted average (*Figure4.29*). Within each individual test, computing a weighted average is meaningful since the instrumental offset remains constant throughout the measurement. However, when comparing different tests, the offset varies, making it inappropriate to average results across separate tests.

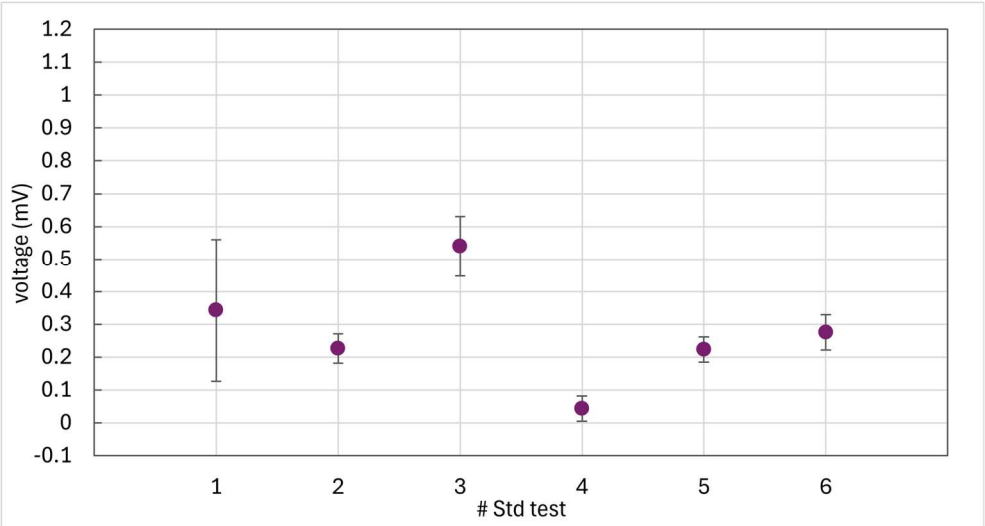



*Figure4.29*: Weighted average voltage measured for each test under *Std* condition.

The same procedure is applied to the other test conditions, as comparable behavior is observed. In following *Figure4.30,* all the resulting values are displayed for a rapid visualization. The actual values for the voltage are not listed due to the missing calibration of the pre-amplifier.

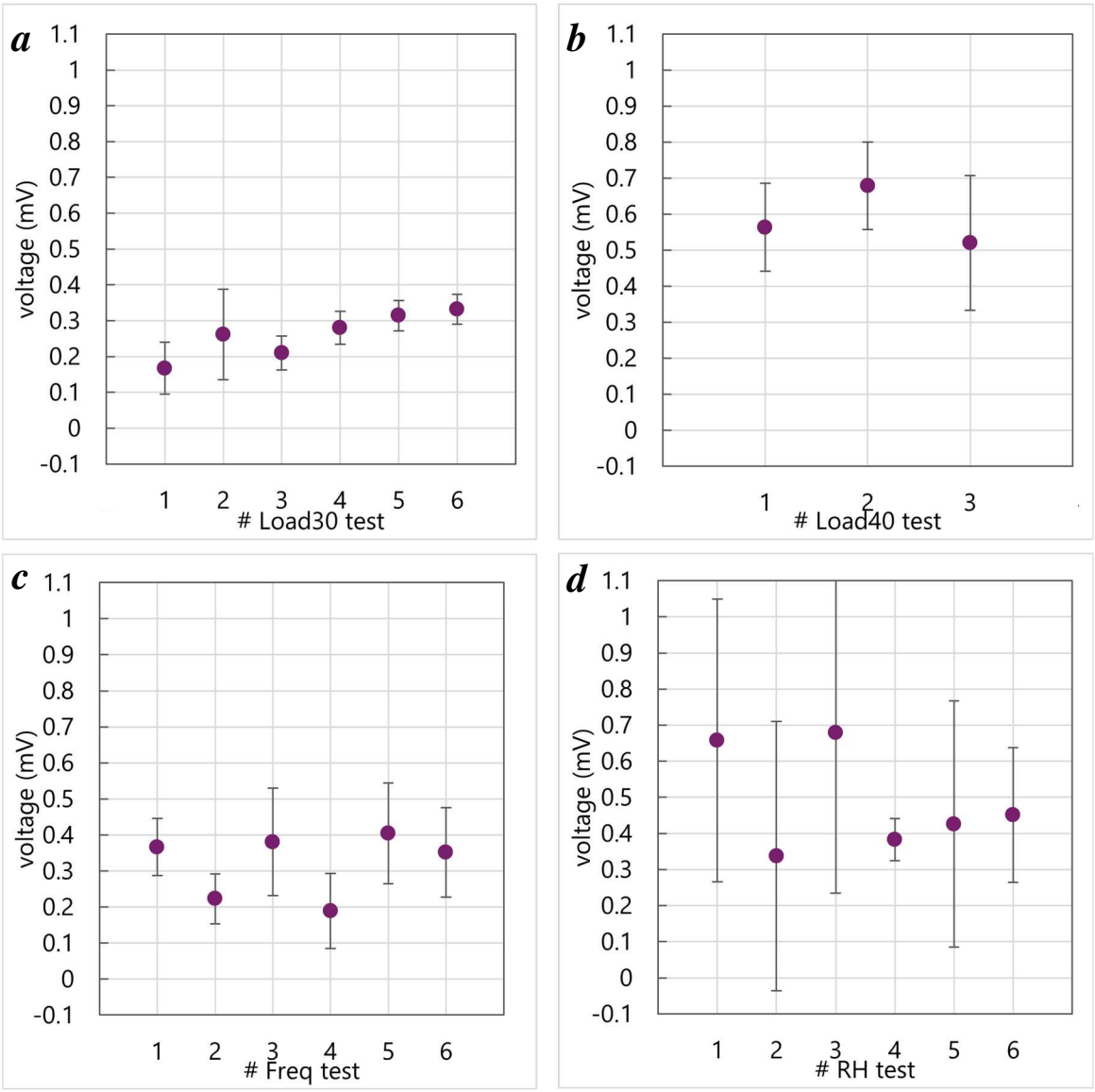



*Figure4.30*: Weighted average voltage measured for each test under (*a*) *Load30,* (*b*) *Load40,* (*c*) *Freq,* (*d*) *lowRH* conditions.

Due to the presence of the offset error, it is not possible to reliably compare the results or to identify any clear dependence on the tribological parameters, but only an order of magnitude, which is $\sim 10^{-1}mV = 10^{-4}V$.

From the qualitative observation made in section 4.2, the voltage peaks seem to increase during the test, passing from low-friction regime to high-friction regime. These considerations have a correspondence in quantitative analysis only in certain tests: in *Figure4.31* the averages for the maxima values of the voltage in *Std* condition are shown as a representative test condition.

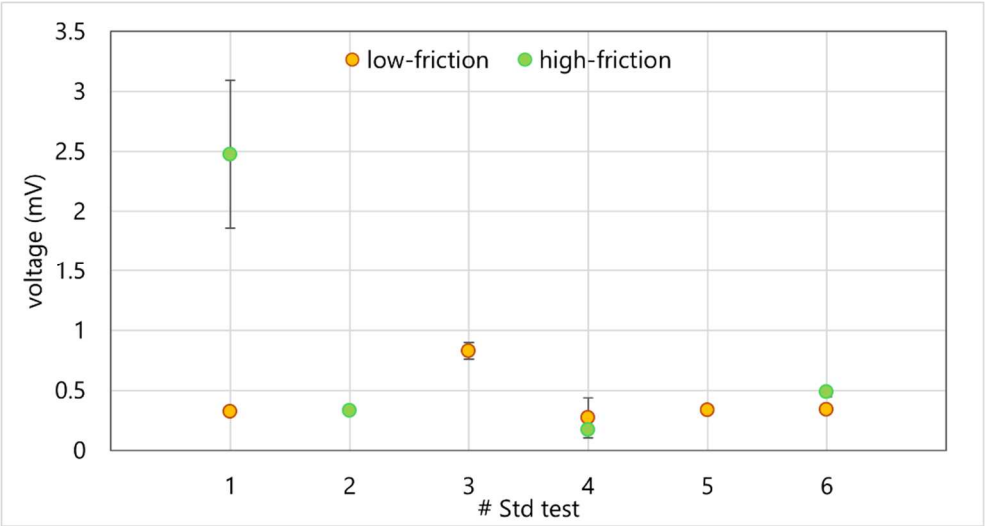



*Figure4.31*: Averages of the voltage maxima measured in low-friction and high-friction regimes.

Considering also the other test conditions, the behavior is the same.

Since the large variation of the voltage peaks appear only in certain tests, mainly in the 300s duration one, more tests with long duration should be performed to have a larger statistic and to deeply analyze the phenomenon. However, the focus of this study is on the low-friction regime.

In the next chapter, the criticisms related to offset and overvoltages are faced.

# 5. Issues related to set-up 1

## 5.1 Electrical issue

As previously introduced, a precise evaluation of the tribovoltage and the definition of a dependence on the tribological parameters aren't possible with this initial set-up, because of the problems with the offset of the pre-amplifier.

While trying to analyze the voltage signals, some incompatibilities arise, as shown in section 4.2.4 and some controversial points have come into light:

- When changing the gain at the start of sliding, the references of the voltage scale are lost due to the amplification altering the offset in a non-deterministic way. This is an important point for the measurement of the real value of the tribovoltaic voltage (*Figure4.8*).

- In some cases, high electrical noise peaks and overvoltage randomly appear at the beginning or at the end of the test, disturbing the acquisition and the synchronization of the electrical signal.

Thus, systematic experiments have been performed at progressively increasing steps of complexity, to explore the causes of the inspected behaviors and to counteract them. As a result, it can be stated that the measured signal is physically meaningful only when the load is applied, as the load ensures stable contact between the surfaces.

The internal offset of the instrument when in DC coupling must be considered. The ground level changes with the set gain in an apparently unpredictable way. Actually, there are two separate units which control the gain, the total gain being the product of a factor 1, 2 or 5 (unit A) and a multiplier (1, 10, 100, 1,000 or 10,000, unit B). It is possible that one or both the gain units are no longer calibrated, so representing a second offset source which is specific for the selected combination of factors and is decoupled from the DC offset.

Moreover, as physics theory suggests, when performing electrical measurements everything should be grounded to the same physical point by adjusting the connections. In the initial used set-up, the grounding alligator clip had to be connected to the circuit's

ground, that is to the ball holder (since it is in touch with the tribometer chassis). Having different grounding points may add noise and offset to the system.

For this reason, the initial connections have been modified: the hook-alligator probe has been replaced with a dedicated probe ending with two ring-terminated wires, fastened to the screw on the ball holder and on the metal clamp, respectively. In this way, more stable contact is ensured.

Experiments on the offset dependence on the gain have been performed with the initial configuration (with hook-alligator probe) and the implemented one (with the custom-made probe) in static condition. The results indicate that up to gain 20 the offset is reproducible and zero or of the order of $\sim mV$ in both cases, while more variability is found for gain $\geq 50$ between different tests (even if the configuration is the same). To assess the correct grounding of the system with the new configuration, data have been acquired both in ground and unground mode, in static condition. The unground mode consists in the introduction of external input which could add some offset if the connections have not been made properly.

For gain $\leq 20$, the data confirm the proper ground, since there is no appreciable difference between the offset of the amplifier (ground mode) and the offset of the complete system (ungrounded mode). For higher gains some differences are present.

Consequently, some recommendations arise:

- Nulling the offset produced by the preamp is required to properly quantify the tribovoltaic effect. This operation could be done by acting on the instrument, but for our purpose, it is sufficient to remove it during post-processing. In principle, the offset experienced during the engagement (stable contact ensured by loading, static conditions) should be subtracted from the voltage data measured during sliding to separate the effect of the tribogenerated component.

The tests performed demonstrate that this procedure, which corresponds to what performed up to now, is correct when maintaining the same gain throughout the whole tests, independently of the value of the gain and when varying it during the tests, provided that gains $\leq 20$ are used (this is true with the new electrical set-up, since reproducible offsets were measured for this range of gains). When working with gains $\geq 50$, the corresponding offset must be measured for each test, since it is quite variable.

For this reason, it is simpler to keep the same gain throughout the whole test. Otherwise, the signal must be grounded before and after any gain change, in order to quantify the current offset shift. Again, this is true only with the new electrical set-up, since the system and the preamp have the same ground level.

As a further consequence, reprocessing the old data using the offsets reported above is unfeasible because of the lack in reproducibility and the improper connections that possibly represent additional sources of offsets. For this reason, a new tests campaign is being carried out, as described in chapter 6.

## 5.2 Mechanical issue

In parallel, implementation of the tribometer was necessarily because large fluctuations in Fz are obtained.

The lasts tests performed after the optimization of the electrical circuit present an increasing oscillation in Fz up to ±100% instead of ±30% with respect to the set value, the variation obtained in the first set of tests. Even if ±30% variation with respect to the set value is higher than the usual ±10% variation obtained with the standard set-up of the tribometer, it is still acceptable for the purpose of this work. In *Figure5.1* the three observed fluctuations of Fz in few seconds of motion:

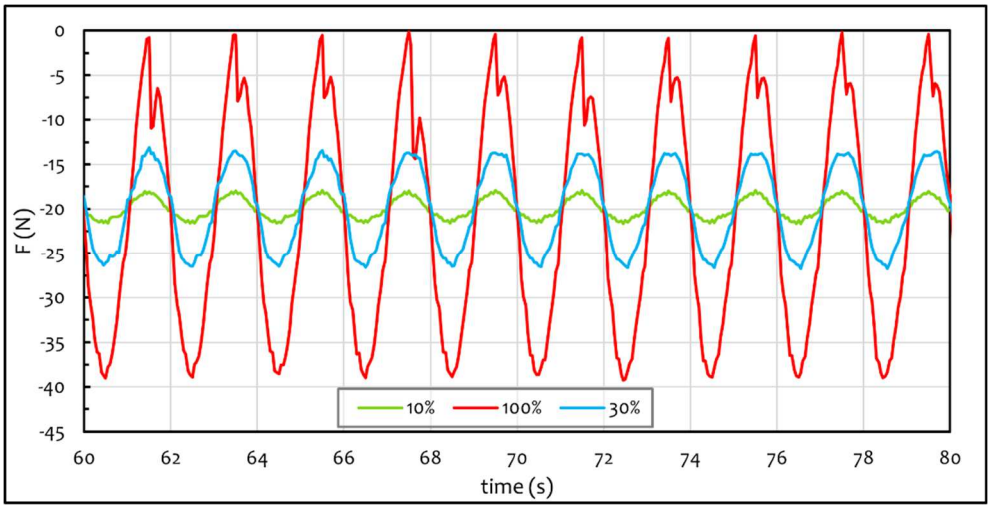



*Figure5.1*: representative example of Fz fluctuation in 20s of sliding. The percentuals are relative to the Fz set value = 20N.

Systematic tests are performed with the reciprocating module in standard configuration (without the implementation for the detection of the tribo-current). With this set-up, the measured Fz presents ±10% variation, as declared by the manufactures.
Thus, further experiments have been performed at progressively increasing steps towards the used set-up, to explore the causes of the oscillations and to remove them.

After some considerations and check of the apparatus, the solution that achieves success is given by the combination of

- refabrication of the Delrin sample holder: the used one appears vertically bent, probably the consequence of the previously performed tests;
- introduction of a suspension (*Figure5.2*), specific for sensor model DFH (the used one) but not recommended by the producer for standard tribological test. Dedicated tests shows that the Delrin undergoes to nanometer deformation that the solely tribometer's feedback system is unable to adequately compensate for.

This combination allows to restore the system to the original stability levels (±10%), even better than ±30% variation obtained with set-up 1.

The used suspension is represented in *Figure5.2*:



*Figure5.2*: Suspension for sensors model DFH.

It is directly screwed to the moving head, where the Fz sensor is present, and it can introduce a correct mechanism of adjustment towards the deformation of the Delrin block (*Figure5.3*). This new set-up allows to restore a ±10% variation with respect to the set value, even better than the beginning obtained variations.

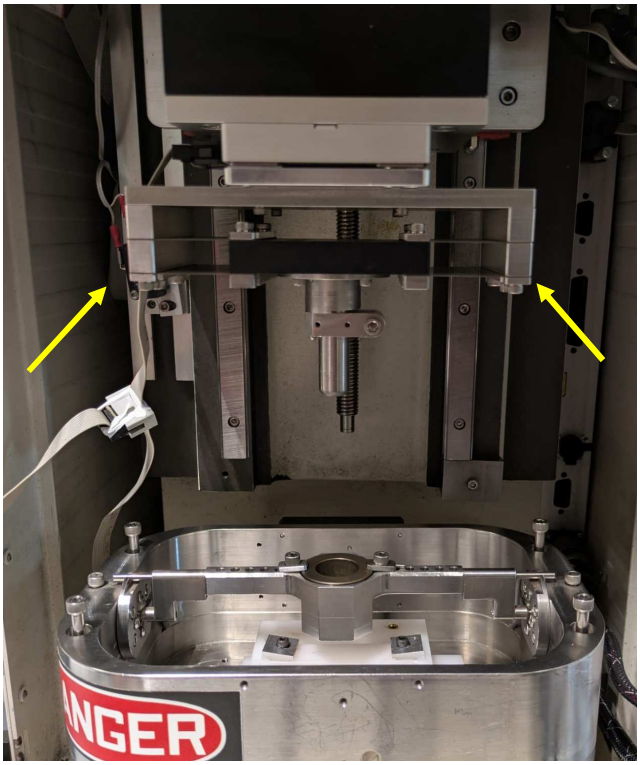



*Figure5.3*: Tribometer set-up with the introduction of the suspension (indicated by the yellow arrows).

# 6. Set-up 2

## 6.1 Implementation of set up 1

The solution of the issues outlined in the previous chapter 5 led to a series of improvements in the experimental set-up. Although the overall configuration remains similar to the initial one, specific modifications were introduced to address the identified instabilities. As a result, the normal force (Fz) now exhibits fluctuations of only around 10% of the set value, the voltage signal is interpreted considering a systematic offset, and the overall signal quality has improved due to reduced noise. This enhanced set-up provides more reliable and consistent measurements.
The set-up is still made by two Delrin blocks with specific holes in order to fix them to the base of the tribometer and to hold the flat counterpart. Since the clamping mechanism in set-up 1 is screwed directly in the Delrin, this is getting ruined, thus it is decided to improve the fixing mechanism by inserting a bushing.

To counteract the deformation of the Delrin block during the test, the suspension is introduced. The connections of the electrical circuit are re-arranged: with a custom-made probe, which ends with two rings-terminated wires, the spherical counterpart is grounded through the connection with its holder, while the flat sample is connected with the other termination through the metal clamp. *Figure6.1* schematizes the connections:

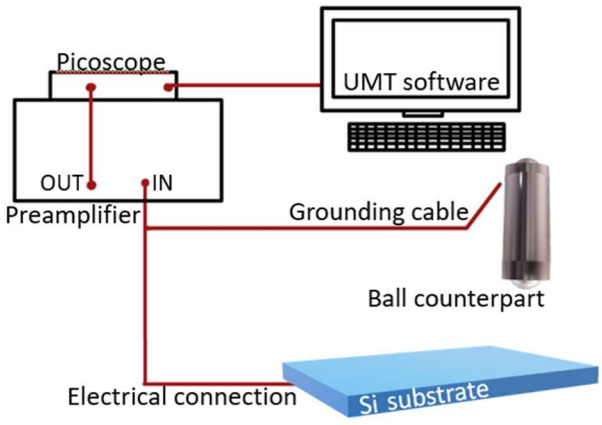



*Figure6.1*: schematic representation of the electrical circuit.

In *Figure6.2*, the new set-up is represented:

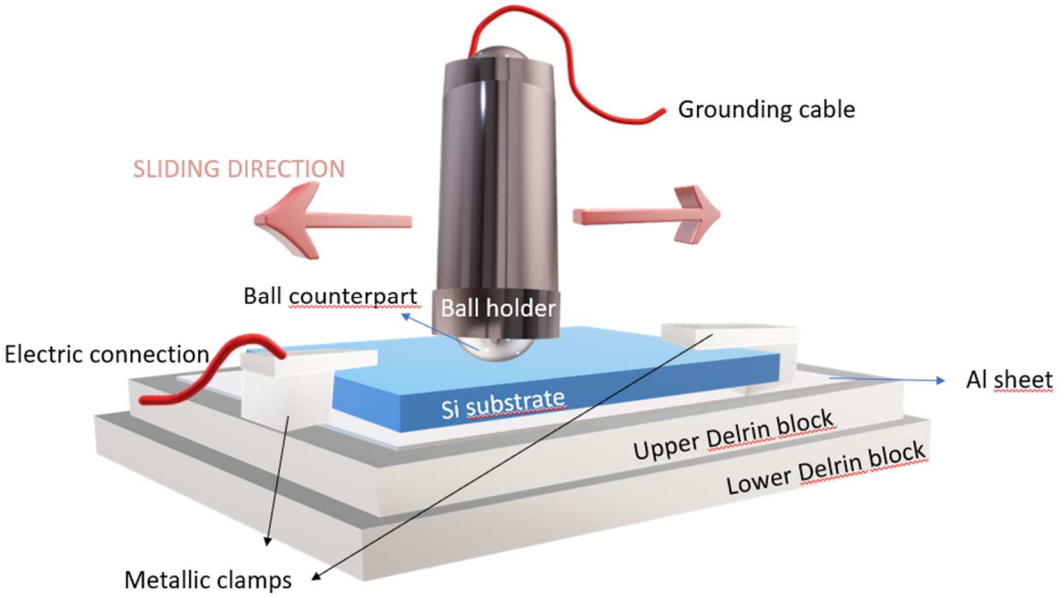



*Figure6.2:* schematic representation of the set-up.

## 6.2 Resulting tribo-electric properties of Al-Si pair

Once solved the problems with the electrical circuit and with Fz stabilization, an additional tribo-electric test campaign is performed, again studying the material coupling Aluminum ball against Silicon substrate 2mm thick.

In this campaign, for each parameter three possible values are selected in order to increase the range of study (i.e. load, sliding frequency, humidity).
As in the previous case, one combination of parameters is assumed as the standard one (called *Std*) and, starting from this choice, the other conditions are defined by changing one parameter between load, frequency and humidity at a time. In this way, it is possible to define the influence of the electrical output on each one of these.
In *Table6.1*, all the test conditions with this implemented set-up are listed.

| Denomination | Load [*N*] | Frequency [*Hz*] | RH [%] |
|---|---|---|---|
| *Std* | 20 | 0.5 | 55 |
| *Load30* | 30 | 0.5 | 55 |
| *Load40* | 40 | 0.5 | 55 |
| *Freq0.8* | 20 | 0.8 | 55 |
| *Freq1* | 20 | 1 | 55 |
| *RH7* | 20 | 0.5 | 7 |
| *RH12* | 20 | 0.5 | 12 |

*Table6.1*: test conditions are listed with the set parameters

For all the tests, the time duration of the following steps of the recipe is maintained fixed:

1. Engagement step: 30s
2. Final part A: 10s
3. Final part B: 10s

Compared to the first configuration, the duration of the initial step has been extended in order to provide a larger dataset for the offset correction during post-processing of the voltage curve. The final steps are less relevant for this purpose, thus the time duration is reduced.

Since the main interest would be on the low friction region part because of its stability, the tests are performed only with 100s duration to achieve a better resolution of this region. Following the same established procedure, 3 tests are performed for each condition to obtain sufficient statistical data. Specifically, the tests are carried out once per day for each condition, over a period of three days, yielding three repetitions per condition. This allows for the evaluation of potential influences on the performances such as environmental changes or the impact of switching the instruments off and on between test sessions.

The base settings of the low noise pre-amplifier were not changed; indeed, the configuration was:

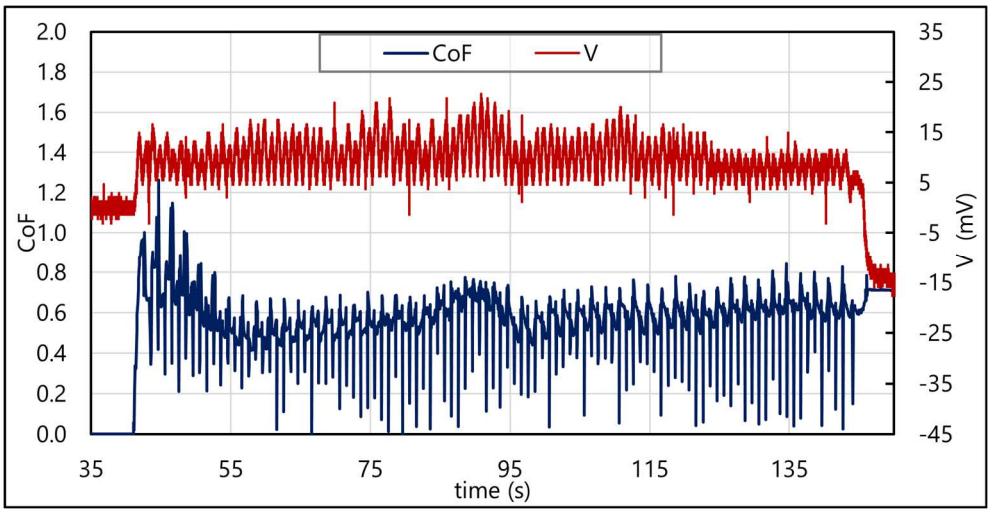
- Coupling: DC
- Filter cutoff frequency: 1Hz
- Rolloff slope: -6dB/octave

Since the tests have 100s duration, the time division for the x-axis on the software was set to 20s/div.

Since the configuration is changed, the gain (on the pre-amplifier) and voltage range for acquisition (on the digital oscilloscope) were re-adjusted, based on the analysis of the new preliminary tests to ensure both the measurement of a finite voltage signal in the interested region and the maximization of resolution. Following the recommendations of "*Issue related to set-up 1*", gain 50 and voltage range of 100mV are set for the whole duration of the test. Due to the internal offset of the pre-amplifier, the gain fixed during the test enables the voltage to be correctly zeroed during the step preceding the onset of sliding and thus shifting the whole curve.

The implemented set-up allows for improved resolution of the output signal and eliminates the offset issue from the electrical measurements, while tribologically, it ensures the application of the set value throughout the entire test.

*Figure6.3*, is a representative example of the observed behavior of the instantaneous CoF values and voltage signal for one test made in *Std* condition plotted as a function of the time:




F*igure6.3:* Typical behavior of the CoF and voltage signal as a function of time. The considered test is *Std.1*.

In the acquired data, CoF plot mainly shows the low-friction regime, and only in certain tests, the increasing CoF is observable.
Indeed, the high-friction regime is either absent or, when present, occurs only for a limited duration. This is consistent with the fact that the studied tests last 100s, which may not be sufficient time for the system to reach a high-friction state every time.
As a representative example of one test in which the increase of the CoF up to the high-friction regime, *Figure6.4* is shown. The represented test is the third one made in *Std* condition, *Std.3*.

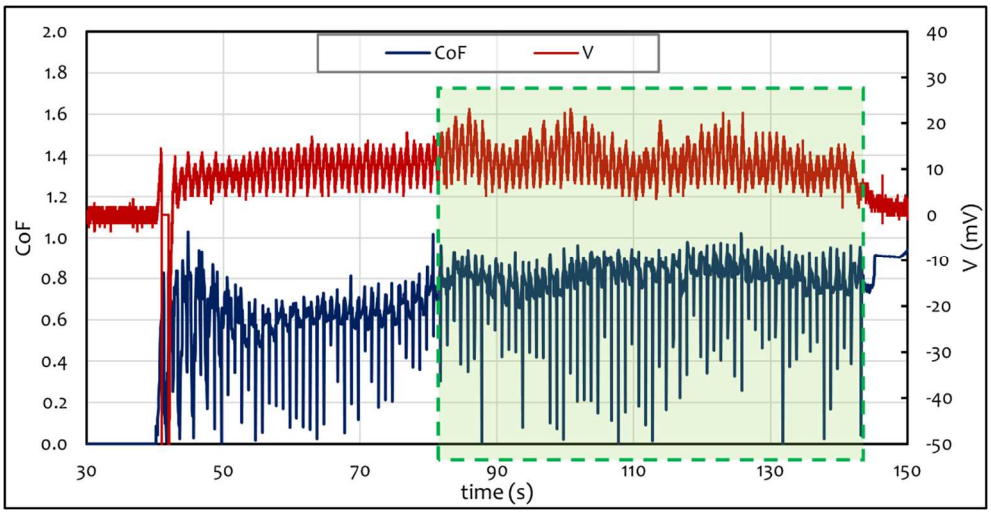



*Figure6.4*: CoF and voltage as a function of time in test *Std.3*. The green box highlights the high-friction regime and the consequent increase in voltage.

In the previous test campaign, the high-friction regime was frequently observed even in short tests: this could be related to the issue related to Fz oscillations, but more tests are needed to verify the hypothesis.
On the other hand, the running in stage seems to be related to the test session, since different general behaviors are collected. The results are discussed in the following section.

Even with the new set-up, the shape of the CoF is maintained; *Figure6.5* represents few sliding passages to appreciate the features: a periodic negative spike in correspondence of the changes in motion direction and a theoretically-flat region, as discussed in section 3.8.

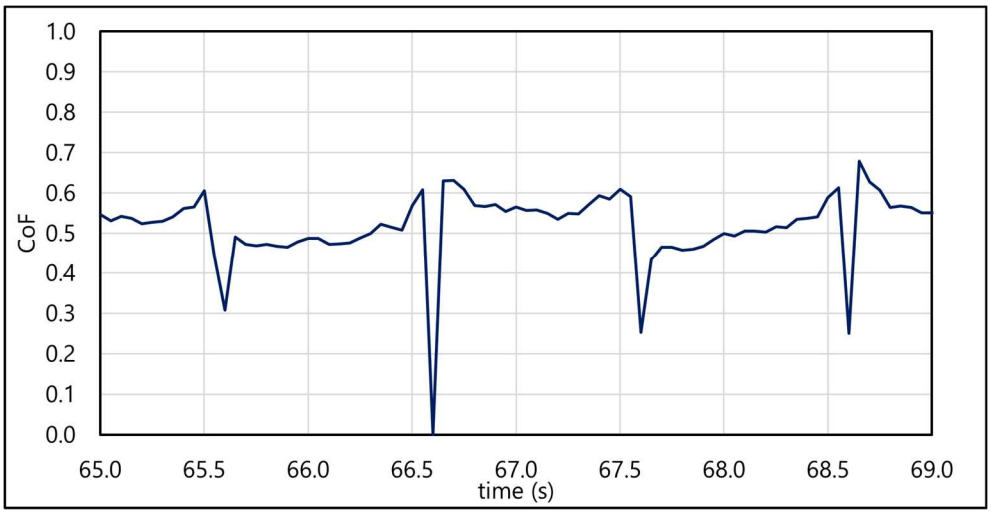



*Figure6.5*: CoF curve as a function of time, in 4s of sliding.

Concerning the generated voltage, the improvements in the electrical connections result in a higher-resolution voltage signal, thereby reducing noise and enhancing the quality of the measurements. *Figure6.6* shows a comparison between signals acquired (*a*) with the first set-up, whose collected curve appears pixelated, and (*b*) with the ultimate set-up, whose collected curve has higher resolution. This comparison is only qualitative; the quantitative

values of the voltage signals are not yet meaningful, as offset correction and gain calibration have not been applied at this stage.

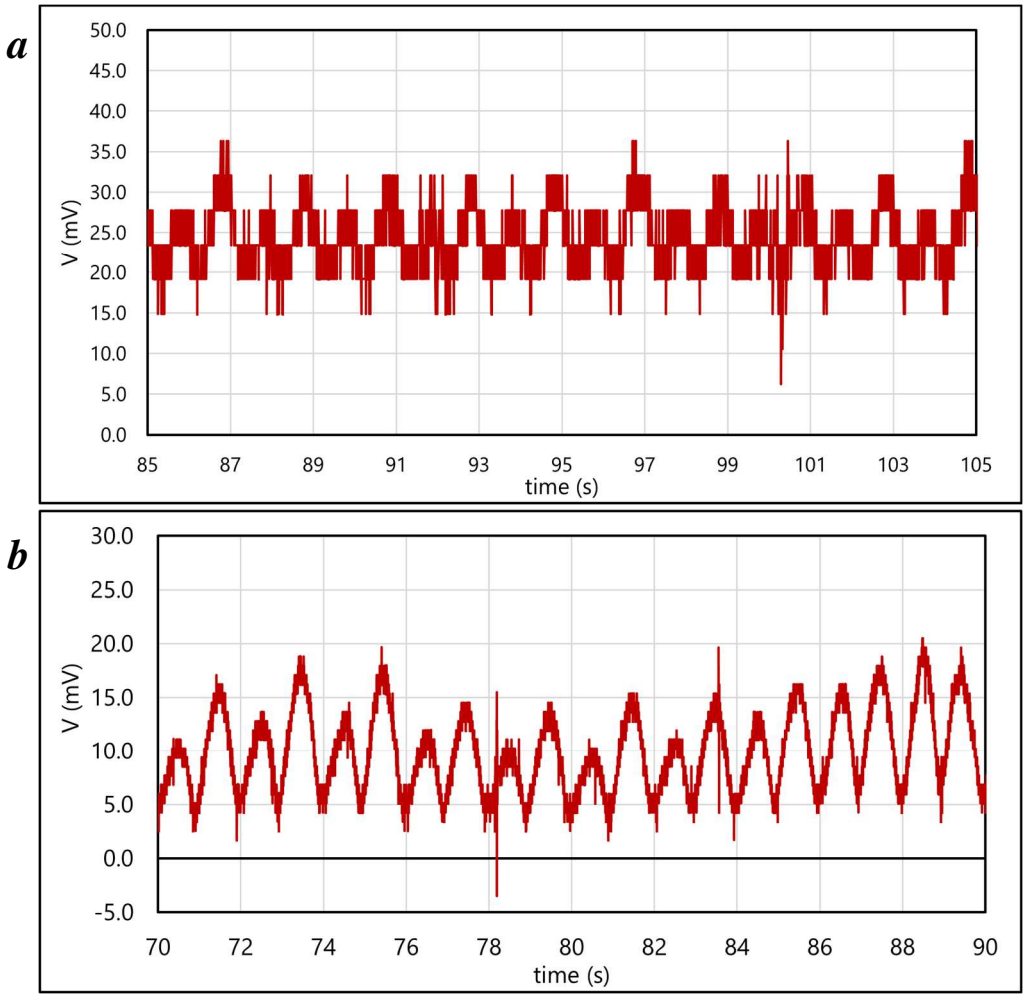



*Figure6.6*: voltage as a function of time with (*a*) the first set-up (test *Std.1*) and (*b*) the ultimate set-up (test *Std.1*). Only 20s are visualized to better appreciate the features.

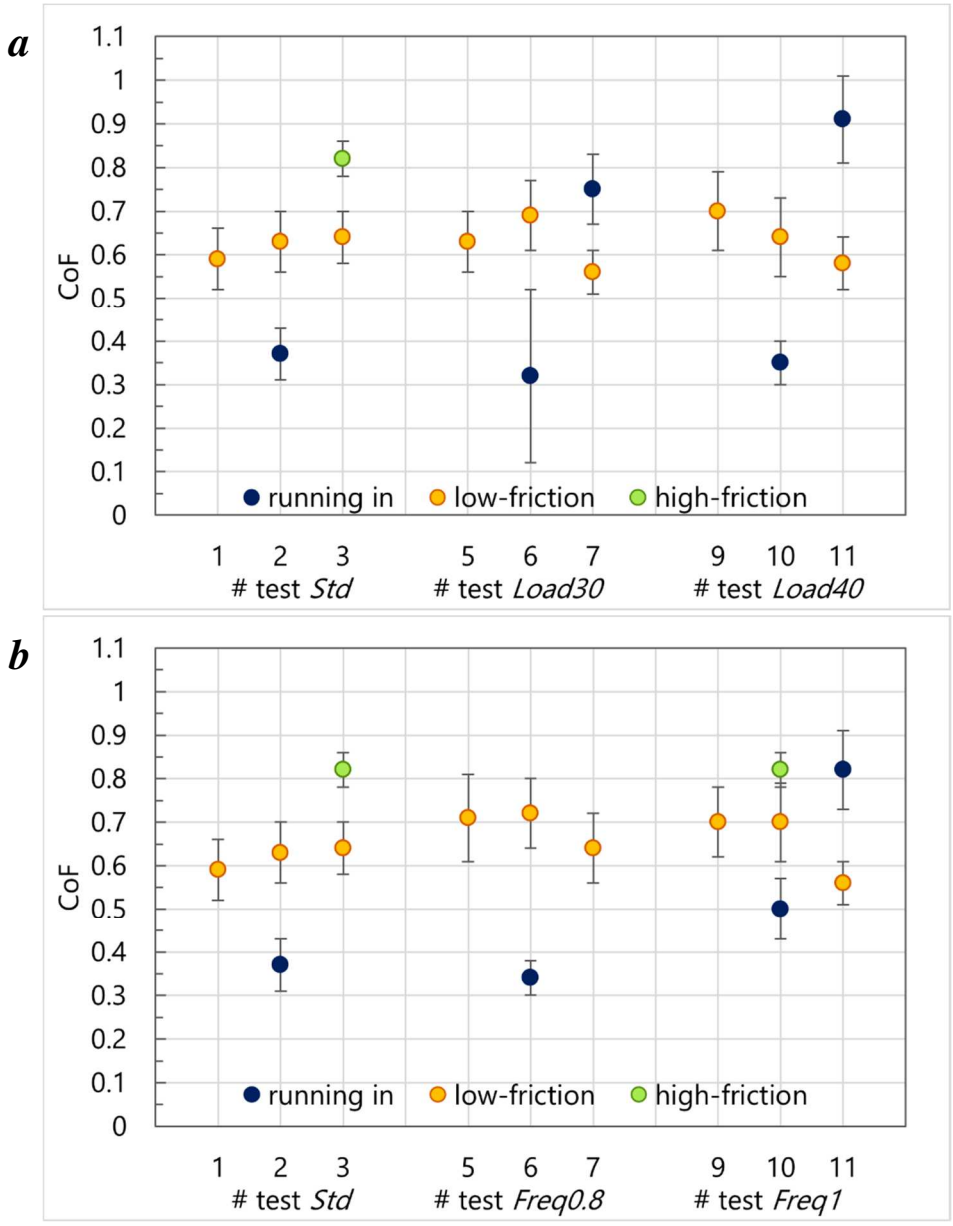
Contrary to the first campaign of 100s tests, overvoltage doesn't occur, except in some isolated cases. Thus, in these tests, overvoltage caused by wear is not measured. The occurrence of overvoltage signal appears only in the first seconds of the sliding motion of some tests, specifically the tests performed in the second session, suggesting a dependence on the test session. It is deeply discussed in the following section.

Even if the selected duration of all the tests of this campaign is 100s in order to avoid high-friction regime, in some tests it is measured. In these cases, the value of the voltage peaks appears to increase, as shown in *Figure6.4*. This result is consistent to what is obtained with the first campaign of tests.
This suggests that, during one test, the voltage depends on the variation of the CoF, but to confirm this assumption further tests should be performed with longer duration, in order to investigate also high-friction regime.

### 6.2.1 Tribological characterization: coefficient of friction measurement

As in the previous analysis, a Matlab script is employed to divide the CoF in distinct regions and to calculate their average values. Considering the evolution of the CoF during sliding (running-in, low friction and high friction), the following graphs represent the different CoF values for each test.

As above anticipated, through the plot it arises that the running in stage is observed to be strictly related to the test session. *Figure6.7* helps with the analysis:



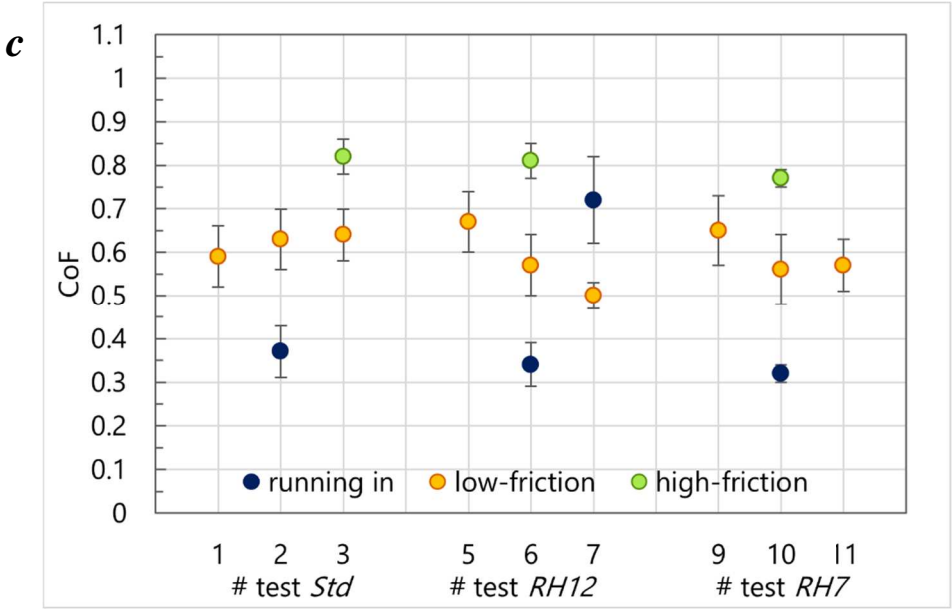



*Figure6.7*: CoF values evaluated through Matlab script for (*a*) *Std* (test 1-3), *Load30* (test 5-7) and *Load40* (test 9-11), (*b*) *Std* (test 1-3), *Freq0.8* (test 5-7) and *Freq1* (test 9-11) and (*c*) *Std* (test 1-3), *RH12* (test 5-7) and *RH7* (test 9-11).

The low-friction regime is the predominant one, while the high-friction regime appears only in certain tests. Concerning the running in phase, some observations are consistent across all conditions:

- Test 1 does not show a CoF value typically associated with the running-in stage in previous analyses (i.e., CoF < 0.4);
- Test 2 exhibits CoF values characteristic of the running-in phase, with $\sim 3/10s$ duration in all the conditions except for *RH7* and *RH12* where it lasts up to $\sim 40s$ of sliding;

  Test 3 shows a running-in phase corresponding to high CoF values ($> 0.8$), which, according to previous analyses, fall within the high-friction regime.

As previously mentioned, tests were performed once per day per condition over three consecutive days, resulting in three repetitions per condition. Therefore, the observed differences in the results could be related to variations between the testing sessions:

- On the first and third days, the analyzed Silicon substrate had never been previously employed and had been stored inside its original packaging. On the second day, however, the opposite face of the sample used on the first day was employed. A potential correlation with substrate oxidation cannot be excluded.
- Relative humidity on the second day was higher ($\sim 59\%$) compared to the other two days ($\sim 53\%$), while no significant differences in temperature were recorded. Considering the results showing the influence of humidity on the CoF, described in the next paragraph, this variation does not appear to be particularly relevant. Clearly, in *RH7* and *RH12* conditions the influence of the environmental humidity is absent since the tests were conducted in a chamber with controlled relative humidity.

However, this aspect should be further investigated through dedicated tests, combined with a chemical analysis via EDX technique.

Focusing on the low-friction region for all the conditions, the average value is extracted using weighted average and the corresponding error δCoF because the values are compatible within the error bars.

To explicitly show the dependence of the CoF on different tribological parameters, the following plots report the calculated CoF values as functions of load, sliding frequency, and relative humidity.

To investigate the dependence of the CoF on the applied load, tests were performed by varying the normal load (20N corresponding to *Std* condition, 30N corresponding to *Load30* condition, and 40N corresponding to *Load40* condition) while keeping the other tribological parameters constant. For the results, refer to *Figure6.8*:

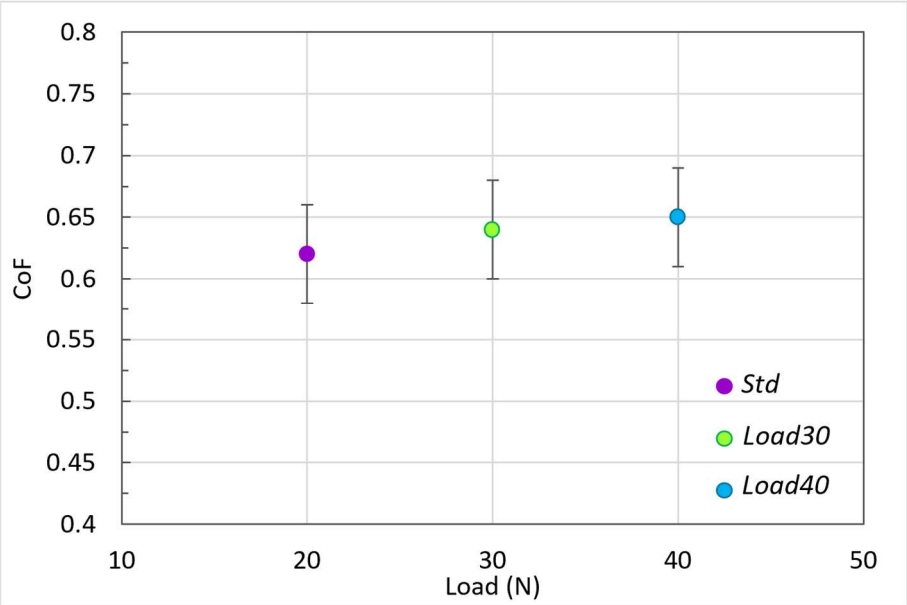



*Figure6.8*: CoF average values calculated for low-friction region are displayed for *Std*, *Load30* and *Load40* tests.

Despite the average values showing an increasing trend with load, the large error bars prevent any definitive conclusion regarding a correlation between load and CoF.

As previously done for the load, the dependence of the CoF on the sliding frequency is also investigated. In this case, the frequency assumes three values: 0.5Hz in *Std* condition, 0.8Hz in *Freq0.8* and 1Hz in *Freq1*, while keeping all other tribological parameters constant. The corresponding analysis is presented in *Figure6.9*:

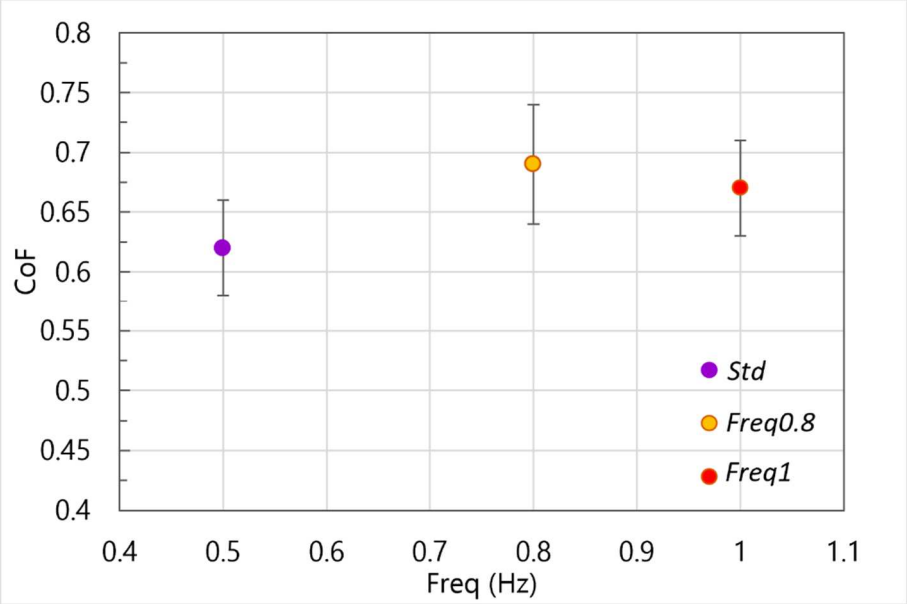



*Figure6.9*: CoF average values calculated for low-friction region are displayed for *Std*, *Freq0.8* and *Freq1* tests.

There are no differences between the three conditions within the error bars.

The same procedure is applied to investigate the influence of relative humidity on the CoF. As previously introduced, three parameters are selected: the usual ambient humidity (~53%), and two lower humidity (~12% and ~7%). The resulting CoF averages are displayed in *Figure6.10*:

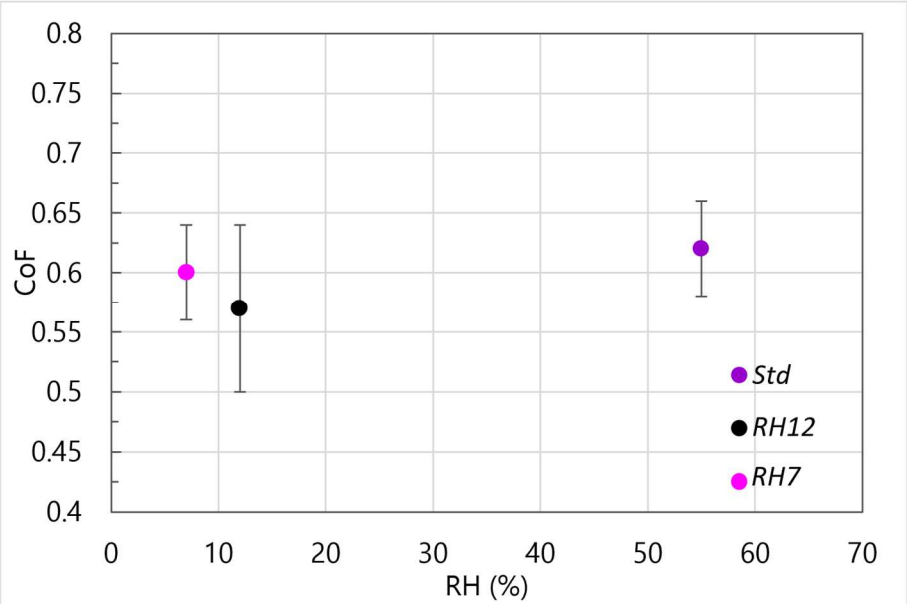



*Figure6.10*: CoF average values calculated for low-friction region are displayed for *Std*, *RH12* and *RH7* tests.

As with the previous parameters, the dependence of the CoF on the relative humidity isn't evident.

From this second set of tests, it can be inferred that the CoF doesn't have a clear dependence on load, sliding frequency and relative humidity. Since the Fz oscillations are reduced, these dependences should be more accurate.

### 6.2.2 CoF comparison between set-up 1 and set-up 2

With the new set-up, the variation in the applied normal force Fz is reduced with the introduction in the tribometer of a suspension, so there could be some differences between the measured CoFs.

In *Table6.2*, the CoF values in the low-friction regime, extracted using the Matlab script, are presented for both the first and second set-ups under all commonly studied conditions. A comparison is also made between the *lowRH* and *RH7* conditions. In the second set-up, which is considered more reliable than the first because the applied normal force exhibits a smaller percentage of variation than in the first set-up, a 5% variation in relative humidity between the *RH7* and *RH12* conditions does not yield any significant differences within the error bars. Consequently, considering that the difference between *RH7* and *lowRH* relative humidities is only 2%, it is reasonable to conclude that this smaller variation in relative humidity would also result in negligible differences in the CoF, if the Fz oscillations are not so relevant.

| **Condition** | **(CoF ± δCoF)** *for 1° set-up* | **(CoF ± δCoF)** *for 2° set-up* |
|---|---|---|
| *Std* | ( 0.65 ± 0.04 ) | ( 0.62 ± 0.04 ) |
| *Load30* | ( 0.64 ± 0.03 ) | ( 0.64 ± 0.04 ) |
| *Load40* | ( 0.63 ± 0.05 ) | ( 0.65 ± 0.04 ) |
| *Freq/Freq1* | ( 0.51 ± 0.07 ) | ( 0.67 ± 0.04 ) |
| *lowRH/RH7* | ( 0.45 ± 0.02 ) | ( 0.60 ± 0.04 ) |

*Table6.2:* average value for the CoF in both the first and second implemented set-up, considering the commonly studied conditions.

The analysis reveals that, under conditions of 1 Hz frequency (*Freq* condition for the first set-up and *Freq1* condition for the second set-up) and low relative humidity (*lowRH* condition for the first set-up and *RH7* condition for the second set-up), the average CoF values obtained from the Matlab script in low-friction regime are lower in the first set-up compared to the second. Given that the second set-up is more reliable, it can be inferred that the observed dependence of the CoF on relative humidity in the first set-up, when considering only the low-friction regime, is likely influenced by the instability of the normal force Fz. Thus, this instability appears to be particularly significant under low humidity and high-frequency conditions.

### 6.2.3 Electrical characterization: tribovoltaic effect

In this section, the voltage generated during tribological tests is analyzed with the aim of correlating it with the applied load, sliding frequency and relative humidity.

For a reliable quantitative analysis, the raw voltage signals are post-processed using dedicated analysis templates, described in section 3.8. This tool allows the extraction of statistical parameters, such as the average and standard deviation, here reported.

As for the CoF, the initial phase shows differences between the tests performed on the first and third days compared to those conducted on the second day. In the tests carried out on the second day, overvoltages are reached within the first few seconds; these are the same tests in which low CoF values are measured during the running-in phase.

A representative example is shown below: *Figure6.11* represents the second test made in *Std* condition (*Std.*2) with the initial overvoltage region.

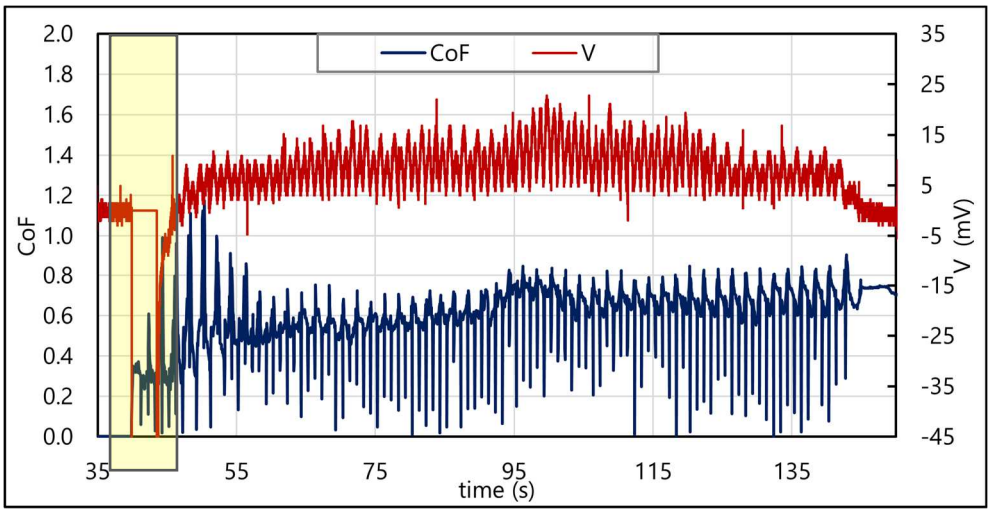



*Figure6.11*: CoF and voltage curves as a function of time in test. The analyzed test is *Std.2*, where negative and no-measurable voltages occurr in the first seconds of motion (indicated with a yellow box).

Additional tests should be performed to have more statistics and to deeply inspect this behavior and its causes.
However, these regions are avoided during the analysis and only those regions with finite output voltage are considered.

For each condition, all tests are comparable in terms of average voltage values, within the margin of error. Therefore, a single average voltage value is computed for each condition using a weighted average formula, along with its associated error. This allows for a straightforward evaluation of the dependence of tribovoltage on applied load, sliding frequency, and relative humidity.

*Figure6.12* shows the tribovoltage as a function of the load. The testes values are 20N in *Std* condition, 30N in *Load30* condition and 40N in *Load40* condition. Thanks to the improvement in the tribological set-up, large Fz oscillations in *Load40* condition don't occur.

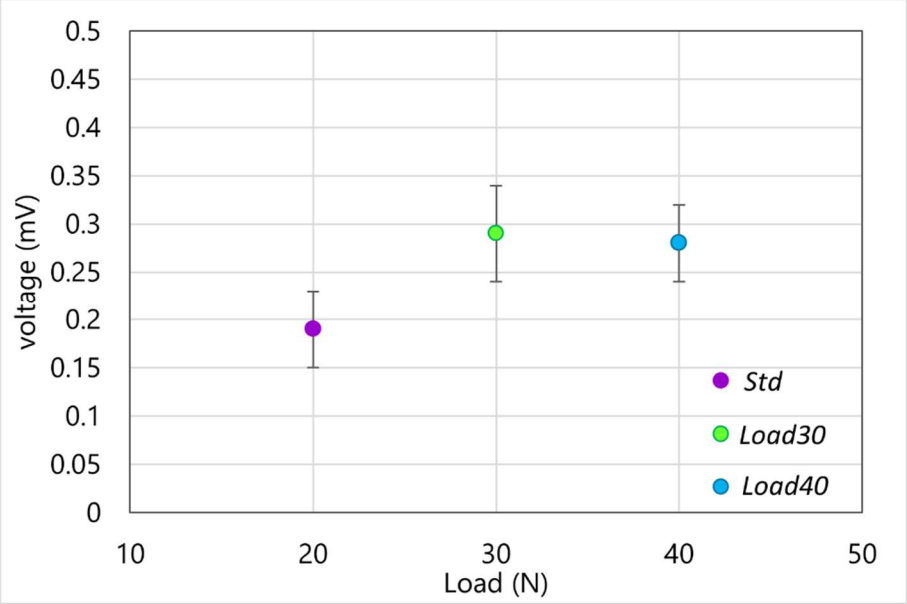



*Figure6.12*: voltage averages values as a function of the applied load. The studied conditions are *Std, Load30* and *Load40*.

The measured tribovoltage increases as the applied load rises from 20 N to 30 N, while no significant differences are observed when the load is further increased to 40 N. This is consistent with the most reliable theory of the tribovoltaic effect (36).
The same procedure is applied also for the dependence on the sliding frequency which varies between 0.5Hz (*Std* condition), 0.8Hz (*Freq0.8* condition) and 1Hz (*Freq1* condition). In *Figure6.13* the average values are shown:

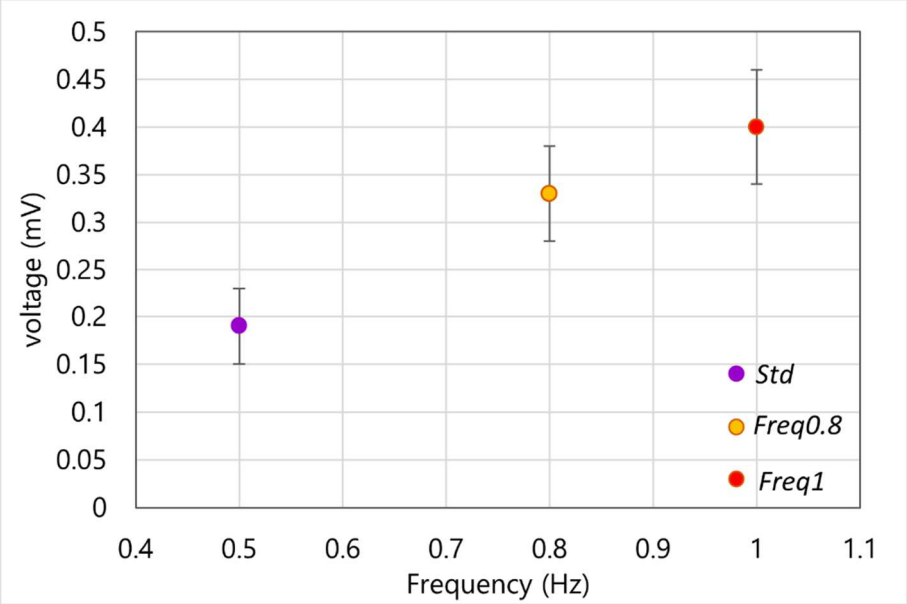



*Figure6.13:* voltage averages values as a function of the sliding frequency. The studied conditions are *Std, Freq0.8,* and *Freq1*.

Despite the larger voltage signal fluctuations observed in *Freq0.8* and *Freq1* conditions (*Figurevoltaggi con box verde?*), the average values show relatively small error bars.
The comparison shows an increase between 0.5 Hz and 0.8 Hz, while no significant variation is observed between 0.8 Hz and 1 Hz within the error range.

The last investigated dependence is on the relative humidity. The chosen values are ~53%, ~12% and ~7%: the respective average CoFs are displayed in *Figure6.14* to simplify the qualitative comparison.

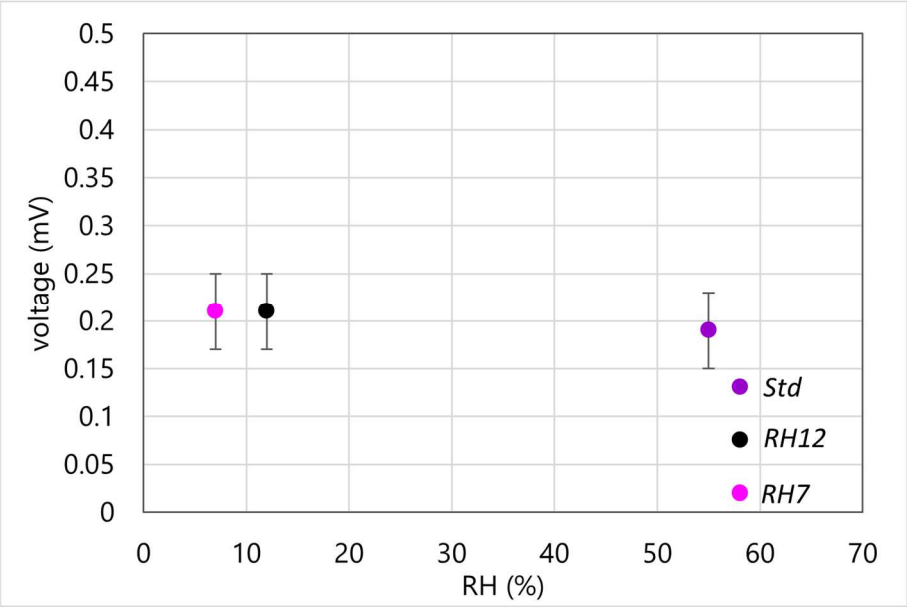



*Figure6.14*: voltage averages values as a function of the relative humidity. The studied conditions are *Std, RH12* and *RH7*.

Tribovoltage does not exhibit a clear dependence on relative humidity.

In summary, no evident correlation between the generated voltage in low-friction region and the investigated tribological parameters is observed, except for the sliding frequency in the range between 0.5 Hz and 0.8 Hz. Further dedicated investigations are required to confirm this trend, possibly by extending the range of tested sliding frequencies.

By comparing these results with those obtained using the previous set-up, it is evident that the order of magnitude remains the same, approximately $\sim 10^{-1}$ mV $= 10^{-4}$ V. Therefore, although the first set-up was not optimal, the measured values can still be considered approximately correct in terms of their order of magnitude.

Concerning the high-friction regime, it is observed only in a limited number of tests. It is expected because the tests perfomed for this campaign have 100s duration in order to focus on low-friction regime and exclude the high-friction one. However, in four test it is recordered and the qualitative observation of the corresponding voltage reports that its peaks seem to increase with the increase of CoF. These considerations have a correspondence in quantitative analysis, excepting for one test (*RH12.6*): in *Figure6.15* the averages for the maxima values of the voltage in all the test where high-friction regime occur are shown. Considering the fact that the tests are performed in different conditions, the plot wants just to show the qualitative behavior of the average voltage maxima in each test, not to compare quantitative the results.

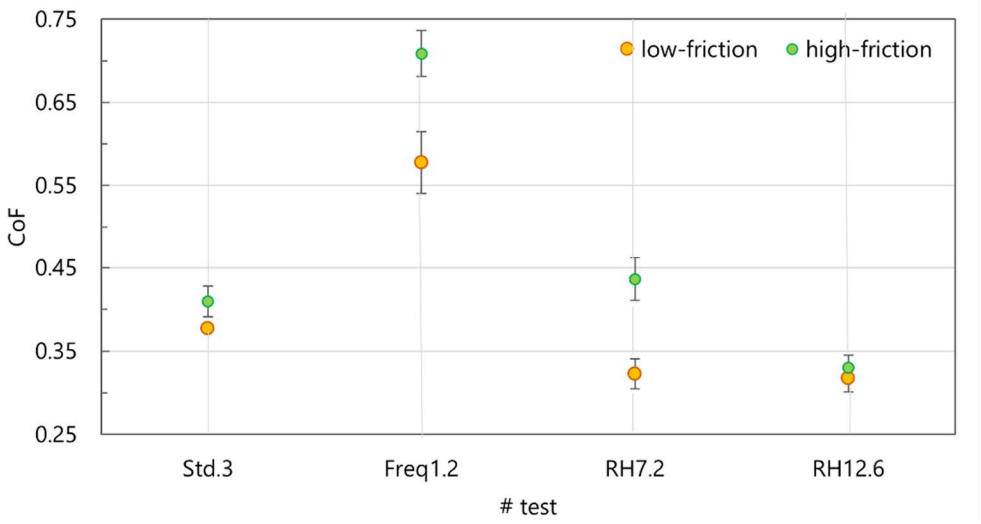



*Figure6.15*: Averages of the voltage maxima measured in low-friction and high-friction regimes, in test *Std.3, Freq1.2, RH7.2* and *RH12.6.*

From this analysis, in the major number of cases the voltage increases with the increase of CoF, suggesting a dependence on it; however, to deepen the behavior in high-friction regime, tests with higher duration should be performed and investigated.

# 7. Collateral measurements

## 7.1 Investigation of the tribo-electric properties of DLC-Si pair

This chapter focuses on the deposition and tribological analysis of Diamond-Like Carbon (DLC) coatings, with the aim of investigating the triboelectric response of different material pairings. In particular, the attention is given to the coupling DLC-Silicon (DLC-Si).

In the present set-up, the Silicon counterpart is available in the form of a standard wafer, thus there is the need to deposit the DLC as a coating onto the spherical component.
The following sections describe the deposition process and the characterization of the resulting film, without the experimental evaluation of the triboelectric signals generated during the sliding with Silicon surface because of the deposition failures. For this reason, since the spherical component is made of Steel, tests are also carried out using the uncoated Steel ball against the Silicon substrate, in order to assess the durability and performance of the deposited DLC layer.

### 7.1.1 Deposition of DLC

The DLC film is initially deposited using a standard deposition recipe optimized for low internal stress. This recipe comprehends the introduction of an interlayer Cr/CrN between the substrate and the DLC layer to guarantee more adhesion of the coating.
The starting settings are the same for each deposition:

- base pressure of the chamber $10^{-6}\ mbar$
- the distance between the substrate holder and the target was set to the minimum allowed by the system (V = 6 cm), in order to achieve the maximum deposition rate while maintaining a limited discrepancy between the central and lateral coating thickness.

In *Table7.1* the parameters used usually for the deposition of DLC are listed. Deposition times were not kept constant throughout this work, since they were varied as part of the experimental investigation.

| layer | duration | source | ΦAr | ΦN | Partial press.(±5%) |
|---|---|---|---|---|---|
| *Cr* | 5’ | 100W in DC | 27.5sccm | - | $\sim 6.88 \cdot 10^{-6}$ bar |
| *CrN* | 2’ 30’’ | 100W in DC | 27.5sccm | 6.75sccm | $\sim 7.51 \cdot 10^{-6}$ bar |
| *DLC* | 40’ | 500W in DC | 27.5sccm | - | $\sim 7.00 \cdot 10^{-6}$ bar |

*Table7.1*: magnetron sputtering parameters used for the deposition.

Before proceeding with the samples preparation, preliminary analyses were performed on a Silicon (111) wafer to determine the deposition rate for both the interlayer and the DLC. Some areas of the wafer are masked with a layer of removable ink to remove the deposition in those regions. Once reached ultra-high vacuum pressure, 5’ of film conditioning of the target is performed to remove surface contamination layers, follow by interlayer deposition on the wafer. This deposition requires 5’ deposition of Cr and 2’ 30’’ of CrN. After returning to the air, the ink is removed, leaving a portion of Silicon exposed, and an analysis is performed with a stylus profilometer to determine the thickness of the deposited coating: on average, analyzing the central portion of the wafer to avoid edge effects, the interlayer is 413nm thick.

Consequently, the interlayer is coated with 40’ deposition of DLC, to determine its deposition rate. The thickness of the deposited DLC coating was evaluated using both the chamber sensor and a profilometer, yielding consistent results. The obtained average thickness is 982 nm, corresponding to a deposition rate of approximately 0.4 nm/s.

### 7.1.2 Chemical characterization: XPS

XPS spectra analysis allows to determine the chemical composition of the deposited coating. For this purpose, Si (100) wafers with dimensions $1mm\ x\ 1mm$ is used to guarantee its introduction inside the XPS chamber. The deposition is performed using the usual deposition recipe, described in *Table7.1.* This analysis is first performed on CrN interlayer and then DLC. The photoemission spectrum is characterized by different peaks corresponding to binding energies characteristic of each element or molecule, in a particular chemical state.

Trying to find the causes of delamination or non-uniformity in the deposited DLC coating, the X-Ray Spectroscopy technique is employed to confirm the chemistry of the interlayer CrN. In *Figure7.1*, the survey spectrum in the range [0, 1100]eV is reported:

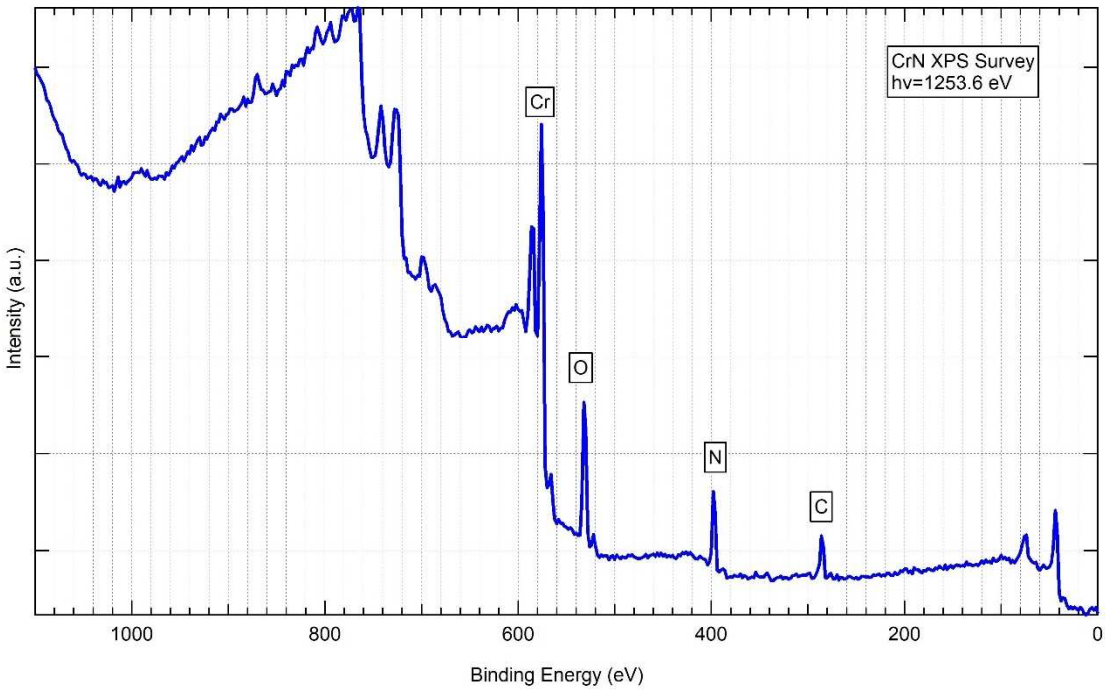



*Figure7.1*: survey spectrum of the CrN interlayer.

*Figure7.2* is related to the fit XPS analysis of the 2p peak related to Chromium present in the interlayer.

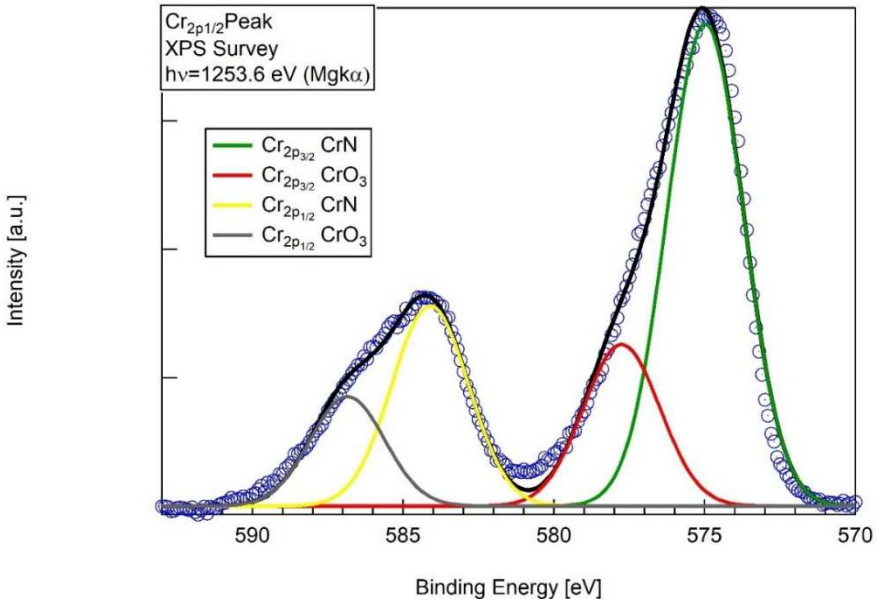



*Figure7.2*: fit XPS analysis of 2p peaks present in the interlayer.

The analysis confirms the expected composition of the CrN layer. The detected oxide is overestimated, as it is the native oxide formed during air exposure and is confined to only the first few nanometers of the surface. However, this oxide layer is not present in the studied samples, as the substrate remains under vacuum between the deposition of the CrN interlayer and the subsequent DLC coating.

Moreover, XPS technique is performed also over DLC coating, in order to determine the characteristics of the deposited DLC. *Figure7.3* is related to the fit XPS analysis of 1s peak of Carbon present in the DLC coating.

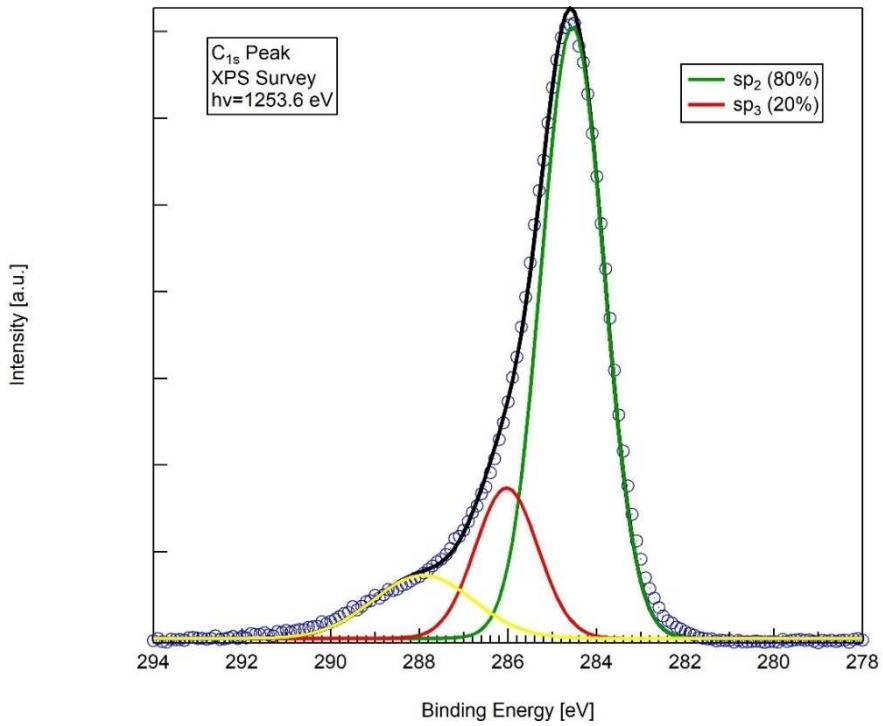



*Figure7.3*: fit XPS analysis of 1s peak of C present in DLC coating.

This XPS analysis represents the typical spectrum of a DLC film deposited using the standard procedure. The fitting reveals a dominant contribution, of approximately 80%, from $sp^2$-hybridized Carbon, shown by the green component. This peak is commonly associated with graphitic Carbon structures. The red peak corresponds to $sp^3$-hybridized Carbon, characteristic of the diamond-like phase, and accounts for roughly 20% of the total Carbon signal. These proportions suggest that the resulting DLC coating should be soft and lubricating, resembling hydrogenated amorphous Carbon (a-C:H). From electrical point of view, it should act as a semiconductor (40), thus with Silicon counterpart, they should create a TVNG.
The lubricating characteristic of the deposited DLC couldn't be verified in the studied sample because the deposited coating is rapidly removed during the test.

It is important to note that these percentages are calculated excluding the yellow component in the fit, which is attributed to physisorbed –OH groups on the surface. This feature is indicative of surface contamination due to environmental exposure.

### 7.1.3 Results of DLC deposition

As previously discussed, in order to test the triboelectric properties of DLC-Silicon pair, the DLC coating must be deposited onto a spherical counterpart, specifically a steel ball. The standard sample holder of the deposition system is a flat plate designed for thin, flat samples, such as the above analyzed wafer. In order to enable the deposition on spherical samples, a custom-made ball holder was designed and fabricated. It consists of two metallic blocks. The upper block is a parallelepiped featuring holes with a 6.3 mm diameter, slightly smaller than that of the balls (6.35 mm), allowing the balls to be supported while still enabling the deposition of the coating in maximum possible area. The lower block is a metallic base with the same dimensions as the upper one and it ensures contact with the flat sample holder of the instrument. It has specular holes designed to only cover the balls. The combination of the two openings perfectly contains the balls and keeps them fixed in position. The two blocks are fixed together and screwed to the sample holder of the instrument, ensuring a stable assembly for the deposition process.

The first sample holder was designed to contain four balls, but a new one was created to allow for the simultaneous deposition of five balls (*Figure7.4*).

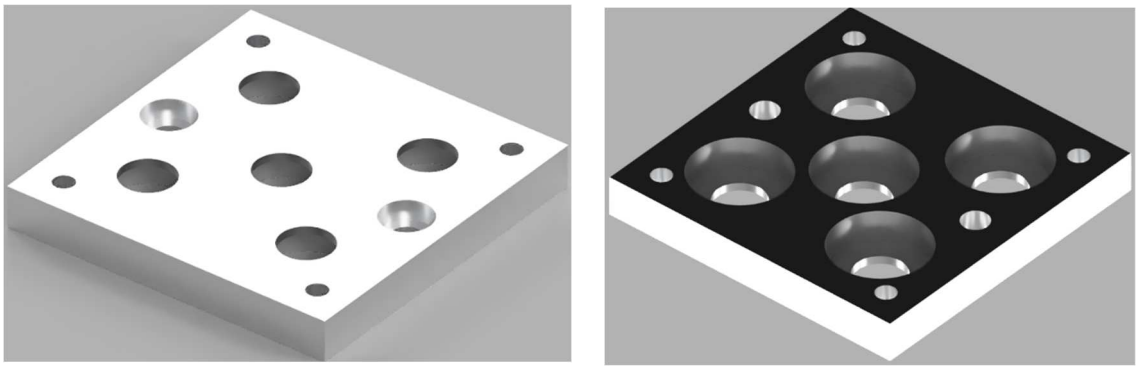


*Figure7.4*: technical rendering of the second ball holder for the DLC deposition for five balls deposition: (*a*) upper and (*b*) lower blocks.

In *Figure7.5,* the designed ball holder is shown:

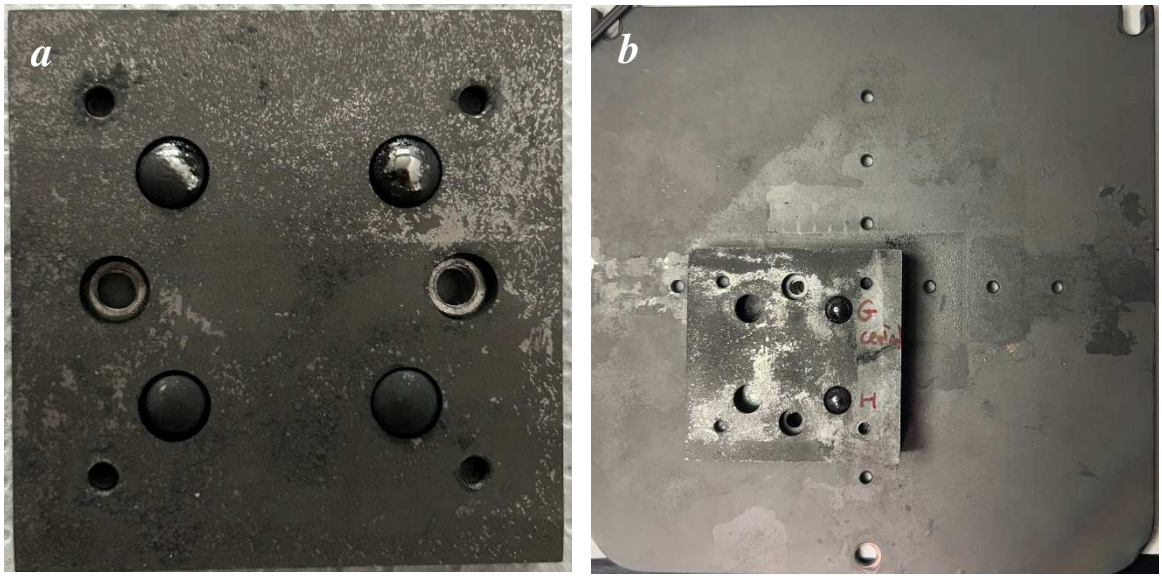



*Figure7.5*: (*a*) designed ball holder for deposition on spherical surface. (*b*) The ball holder is situated on the standard plate of the instrument in one of the possible positions.

The standard flat holder of the instrument features multiple threaded holes, allowing the ball holder to be mounted in various positions. The ball holder itself includes four sites for spherical samples, enabling deposition to be performed on balls placed at different locations. This flexibility allows the deposition in different positions inside the chamber for evaluating its effect on coating properties and uniformity.
However, due to the deposition process geometry, the non-planar nature of the surface represents a significant challenge for the coating deposition. This curvature often leads to poor adhesion of the film, resulting in delamination, or, when delamination does not occur immediately, in rapid removal of the coating within the first few test cycles. This effect can be inferred from a sharp increase in the CoF, indicating that the underlying steel surface is exposed (section 7.1.4)

To address this issue, several deposition parameters were systematically varied to identify a suitable combination that would ensure sufficient coating adhesion and durability.

*Table7.2* shows the changes in the deposition parameters:

| **Parameter** | **Range of variation** |
|---|---|
| Deposition time of DLC | 40’ , 90’ |
| Deposition time of interlayer CrN | 2’ 30’’ , 5’’ |
| Cooling environment | air, vacuum |
| Pre- deposition cleaning | standard ethanol cleaning, ultrasonic bath with acetone and ethanol |
| Lateral sample position | central, lateral (see *Figure7.5*) |

*Table7.2*: Deposition parameters varied during the optimization of the DLC coating process.

After the deposition process, an optical microscope is employed to qualitatively visualize the surface condition of the DLC coatings. This preliminary inspection allows for the identification of macroscopic defects such as delamination or non-uniform coating.

In *Figure7.6*, two representative cases are shown: (*a*) illustrates a failed coating, characterized by clear signs of irregularity, and (*b*) shows a homogeneous and continuous film. The deposition recipe is the one in *Table7.1,* while the explored deposition parameters set for these coatings are listed in *Table7.3* (in this case, the correct deposition time for the coatings is listed in the following table).

| **Parameter** | **Failed coating (*a*)** deposition *A* | **Homogeneous coating (*b*)** deposition *B* |
|---|---|---|
| Deposition time of DLC | 90’ | 90’ |
| Deposition time of CrN | 5’ | 2’ 30’’ |
| Cooling environment | air | air |
| Pre-deposition cleaning | ultrasonic bath with acetone and ethanol | ultrasonic bath with acetone and ethanol |
| Lateral sample position | central | central |

*Table7.3*: set parameters of the deposited DLC coating represented in *Figure7.6*

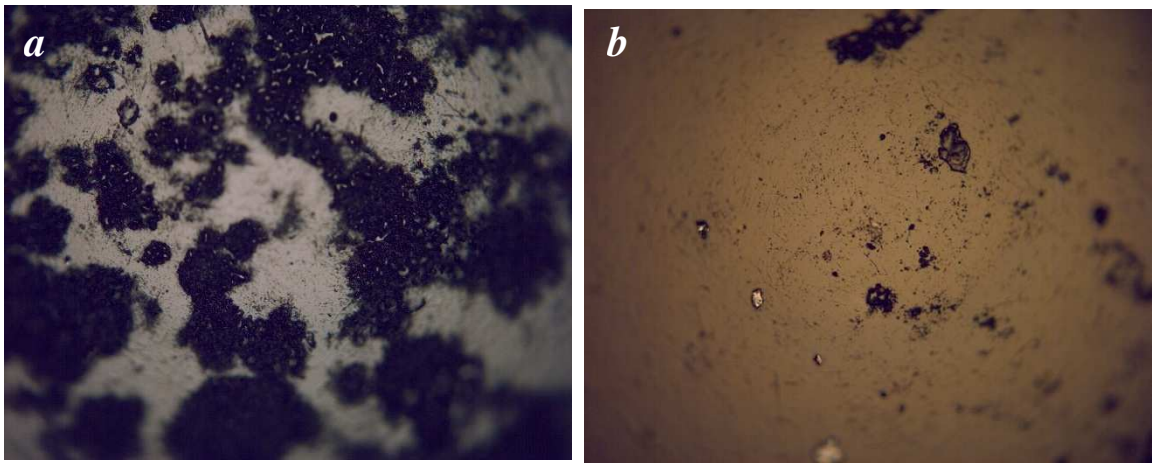



*Figure7.6*: optical microscope image with 5X magnification of (*a*) a failed DLC coating and (*b*) a homogeneous one.

Moreover, the position of the sample within the deposition chamber plays a crucial role. *Figure7.7* shows four DLC coatings deposited during the same deposition cycle (*C*) on identically steel balls, placed in different positions with respect to the target. Differences in coating characteristics are clearly observable even to the naked eye, caused by shadowing effects inherent to the deposition geometry. This effect is evident both between different samples and across different areas of the same ball: indeed, *Figure7.8* represents the image (*a*) of the most uniform and (*b*) of the worst coated steel ball in deposition *c* (its parameters are listed in *Table7.7*)

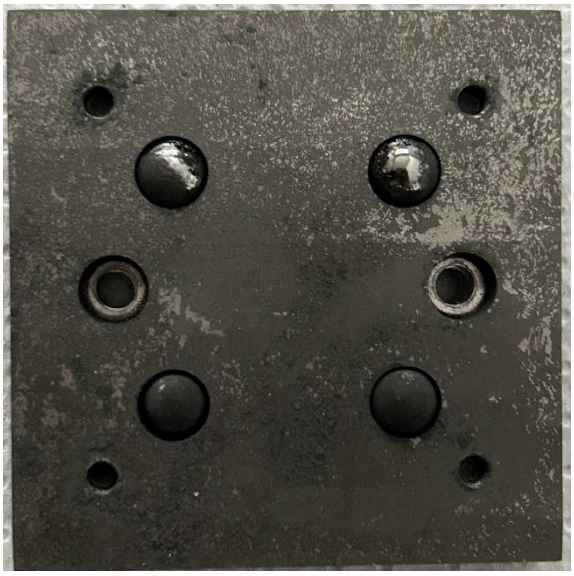


*Figure7.7:* DLC coatings on balls located in different positions relative to the target, highlighting the impact of shadowing effects during deposition *C*.

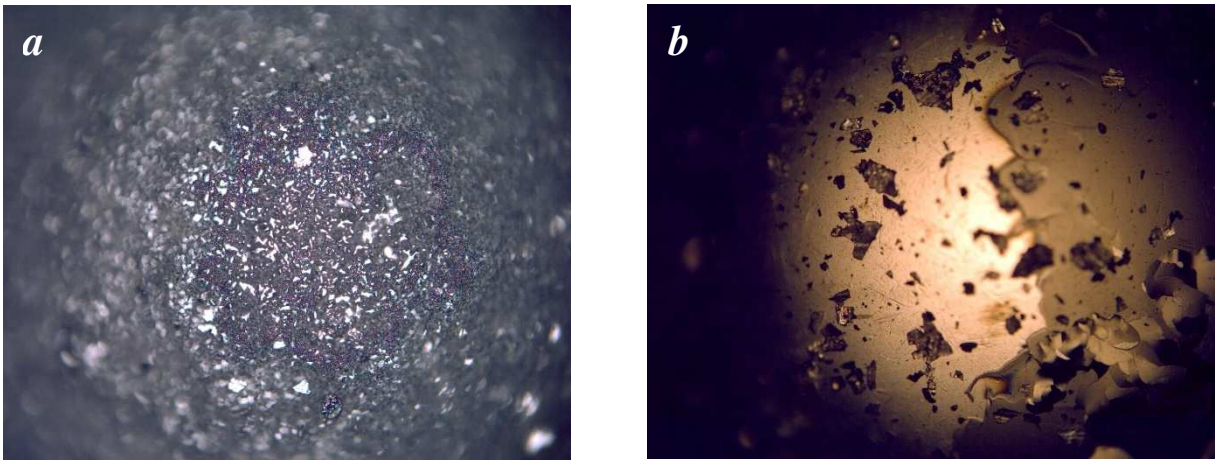



*Figure7.8*: optical microscope image with 10X magnification of (*a*) the most uniform DLC coating and (*b*) the worst one related to deposition *C*.

| **Parameter** | **Setting** |
|---|---|
| Deposition time of DLC | 90’ |
| Deposition time of interlayer CrN | 2’ 30’’ |
| Cooling environment | vacuum |
| Cleaning procedure before deposition | Standard ethanol cleaning |
| Lateral sample position | central (*a*), lateral (*b*) |

*Table7.7*: Set parameters for deposition *C*.

However, the homogeneity of the coating does not necessarily guarantee stable adhesion to the substrate. Indeed, the details of a tribological test are discussed in section 7.1.4 where the mechanical stability of the film is evaluated.

### 7.1.4 Tribological characterization: coefficient of friction measurement

As previously anticipated, the coating uniformity seen at the optical microscope doesn't correspond to a stable adhesion of the DLC coating and consequently durability of it during tribological tests made against Silicon substrate (DLC-Si).
All DLC-coated balls that exhibited uniform surface and no signs of spontaneous delamination are tested. Nevertheless, only in a limited number of tests the measured CoF approaches the characteristic values expected for DLC (38) but only in the first sliding passages. In *Figure7.9* one example of these tribological test is displayed: this test is made in *Std* condition with a time duration of 100s. For the sake of completeness, it should be noted that the new electrical configuration has already been implemented, although the suspension has not yet been introduced: in this case, the Fz oscillations are higher than in the first set of test (±30% of the Fz set value) but smaller than ±100%, which corresponds to a critical condition. In the following tests, oscillations are around ±70%. Despite this, the aim of the following analysis is to demonstrate the occurrence of failure of the DLC coating since the CoF usually measured for DLC lasts few sliding passages.

For this test, the parameters for deposition *D* are listed in *Table7.8*, while the optical microscope image of *Figure7.10* shows the deposited coating before the test, to show the resulting coating.

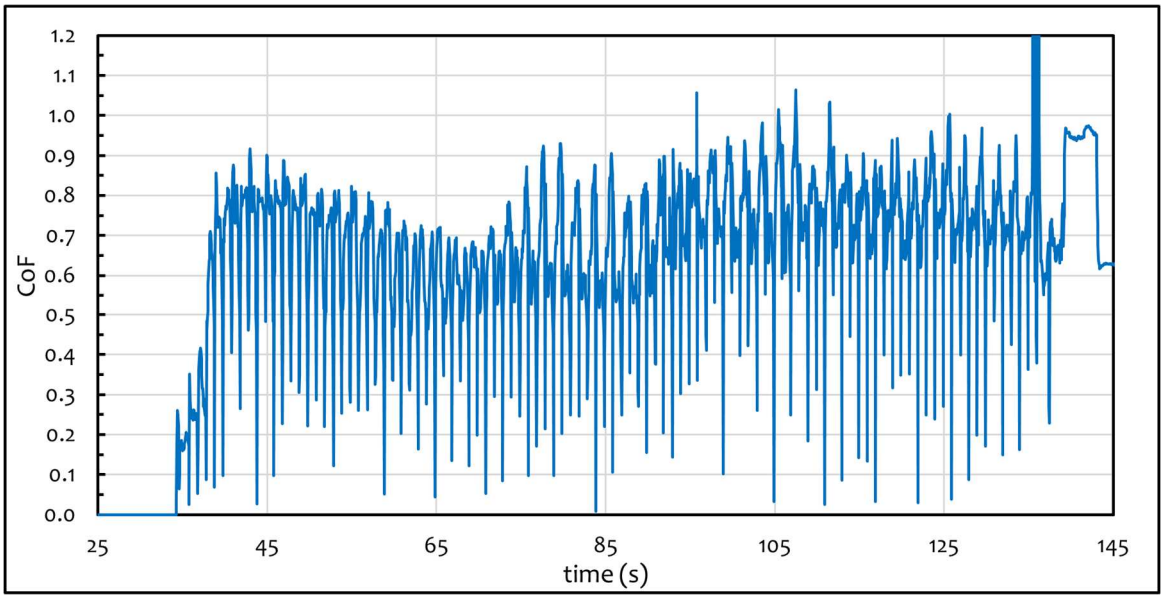



*Figure7.9*: CoF signal as a function of time measured in DLC coated ball (deposition *D*) against Silicon substrate test.

| Parameter | Setting |
|---|---|
| Deposition time of DLC | 90’ |
| Deposition time of interlayer CrN | 2’ 30’’ |
| Cooling environment | vacuum |
| Cleaning procedure before deposition | Standard ethanol cleaning |
| Lateral sample position | Central |

*Table7.8*: Set parameters for deposition *D*.

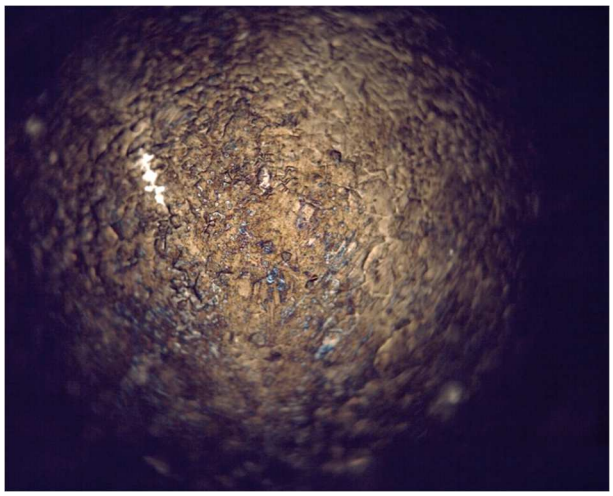


*Figure7.10*: optical microscope image (10X magnification) of the DLC coating (deposition *D*). The sphere is uniformly coated, with no signs of partial coverage, although the surface exhibits a noticeable granularity.

During the initial seconds of the test, CoF exhibits values in agreement with the expected range (38). However, as the test progresses, an increase in CoF is observed.
The dedicated Matlab script is used to segment the test into tribological regions, each defined by a characteristic CoF and duration. These values are listed in *Table7.9*.

| Matlab regions | (CoF ± δCoF ) | Time duration |
|---|---|---|
| first region | ( 0.3 ± 0.2 ) | 4.2 sonds |
| sond region | ( 0.72 ± 0.06 ) | 95.8 sonds |

*Table7.9*: CoF values and their respective durations for each Matlab region of test DLCc.

As observed from a preliminary qualitative analysis of the friction curve, the CoF remains within the expected range for DLC coatings only during the first 4.2 $seconds$ of the test, corresponding to approximately two sliding cycles.
Beyond this point, the CoF increases significantly, suggesting that the DLC coating may have been completely worn away, leaving only the underlying layers (the interlayer and the steel substrate) in contact during the remaining part of the test.

To support this hypothesis, *Figure7.11* shows a comparison between the current test and a reference test performed using a steel uncoated ball against a Silicon substrate (steel-Si) under the same experimental conditions. The used Silicon substrate has the same characteristics of the one previously employed.

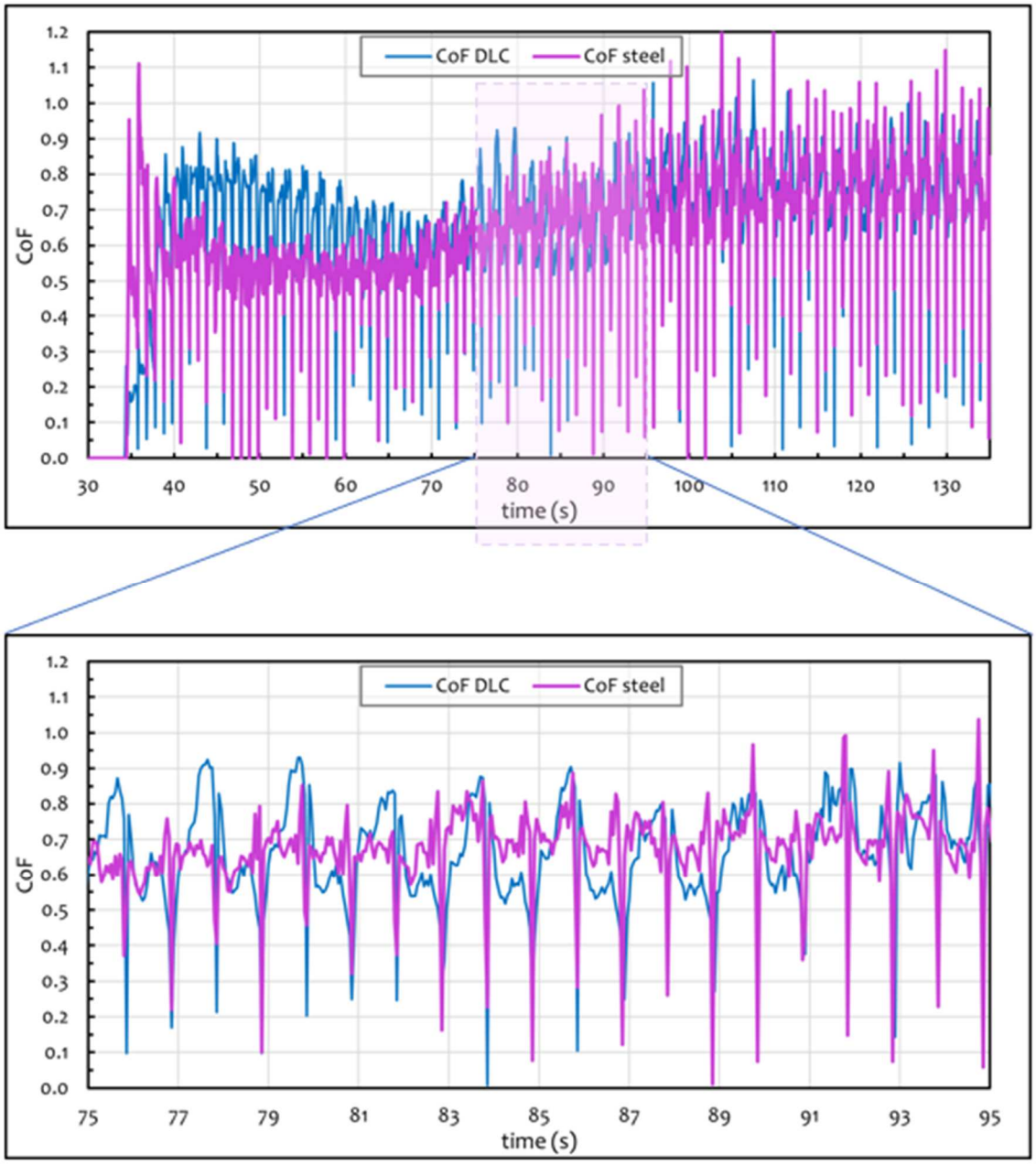



*Figure7.11*: comparison between CoF curves related to steel-Si test and DLC-Si test: (top) complete duration and (bottom) 20s zoom.

In the running-in phase, in DLC-Si test the CoF shows an increase. Excluding this first section ($\sim 5\ s$), in the next $\sim 30s$ of sliding, the CoF values observed for the DLC-Si test are higher than those measured for steel-Si test. This is probably due to progressive wear causing the partial or complete removal of the DLC coating, which results in an increased CoF. In contrast, the initial CoF behavior in the steel–Si test can be attributed to the running-in phase. However, once the motions stabilize, the CoF values for both systems tend to converge toward a similar range.

To enable the quantitative comparison of the CoF values, the Matlab script is used to extract the average CoF from the steel–Si test. *Table7.10* reports the CoF corresponding to the

second region of the DLC test and the value obtained from the entire duration of the steel–Si test, according to Matlab script.

| Test | ( CoF ± δCoF ) |
|---|---|
| DLC-Si test | ( 0.72 ± 0.06 ) |
| steel-Si test | ( 0.8 ± 0.1 ) |

*Table7.10*: the CoF value for the steel-Si test evaluated through the Matlab script are compared with the one of DLC second region.

The data verify the consistency of the CoFs within the error range.

In addition, a shorter duration test of 30s is performed with DLC coated ball (with deposition *B*) against Silicon substrate in *Std* condition, in order to focus on the first sliding passages. *Figure7.12* shows CoF curve collected during the test.

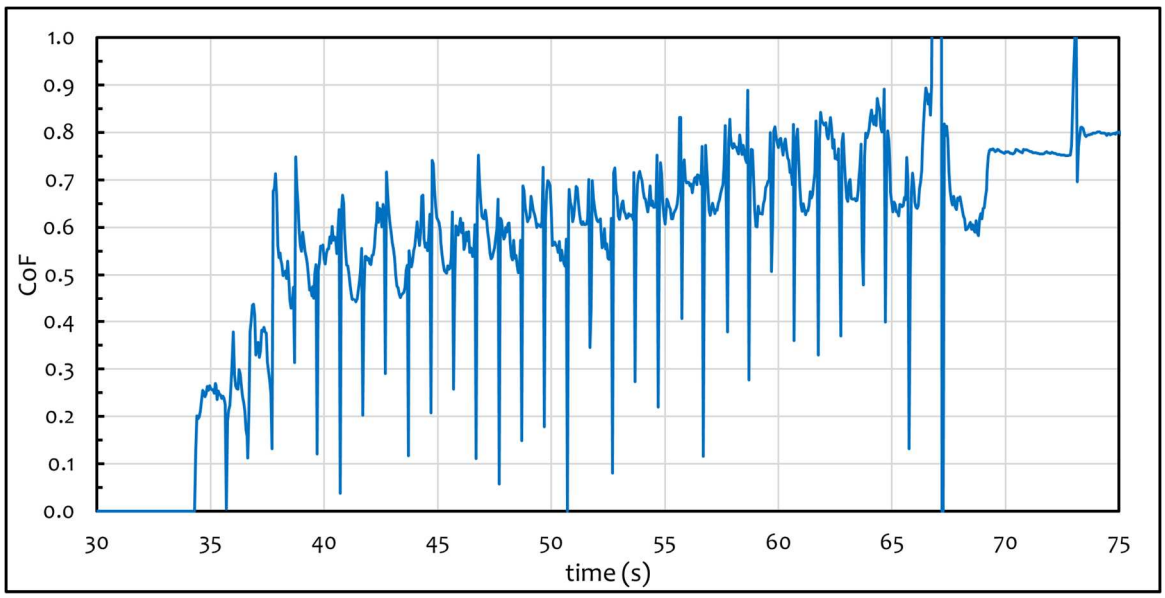



*Figure7.12*: CoF curve of the 30s test made with DLC coated ball (deposition *a*) against Silicon ball.

The behavior is consistent with that observed in other tests: after approximately three sliding passages, the DLC coating appears to be completely removed. The subsequent CoF then starts to increase reaching values comparable to those measured in the steel–Si test.

Due to the rapid wear of the DLC coating, no test could be carried out for a sufficiently long time to allow meaningful measurement of the tribovoltaic voltage signal generated by DLC-Si coupling. For this reason, the electric measurement is not presented.

### 7.1.5 Morphological characterization: EDX

Based on tribological results, it is inferred that the DLC coating is entirely removed during sliding, as the CoF values converge to those measured in steel-Si test.
To validate this assumption, an EDX analysis is conducted to investigate the elemental composition of the surface of one ball after one test. Both the worn and pristine surfaces are analyzed in order to verify the absence of Carbon in the scar in one case, and to confirm the presence of it elsewhere.

The ball considered for the analysis is the one used in the 30s test, in order to verify whether the DLC coating had already been removed after such a short sliding time. *Figure7.13* shows the surface of the wear region on the ball counterpart, acquired using two different imaging techniques:

- An optical microscope at 5× magnification, providing a general overview of the worn area;
- A Scanning Electron Microscope (SEM) at 300× magnification, using a backscattered electron detector and an incident electron beam of 25 kV; in *Table7.11* the morphological informations, as the atomic percentual, are displayed.

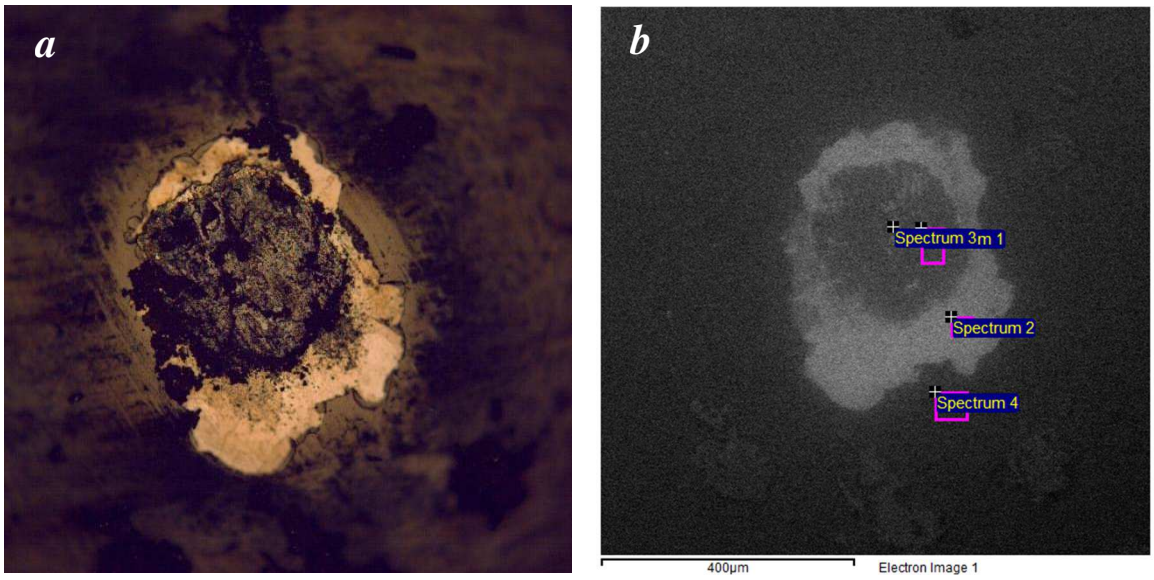



*Figure7.13*: image of the ball scar related to 30s test taken (*a*) with optical microscope (20X magnification) and (*b*) with SEM (300X magnification, BSE detector).

*Figure7.13a* confirms that the motion corresponds to a pure sliding mechanism without rotation of the ball during the test, as evidenced by the circular shape of the worn area. Based on the color contrast, three distinct regions can be identified: a central zone, a surrounding circular area, and the outer region where the coating remains intact. This distinction suggests that the central area corresponds to the sliding zone against the Silicon substrate. The brighter surrounding region likely reveals the interlayer, exposed due to

wear. It is also possible that the central zone exposes the same interlayer but appears darker due to the accumulation of debris. Beyond these regions, the DLC coating remains intact. To verify these considerations, different areas are selected for compositional analysis: one within each of the identified regions, and an additional one corresponding to the black debris. These areas are indicated by pink squares in *Figure7.13b.*

The following plots report the EDX spectra associated, where the detected elements are identified by their characteristic peaks. The intensity of each peak is proportional to the relative abundance of the corresponding element within the analyzed area.

*Figure7.14* represents *Spectrum 1* taken in the central worn area.

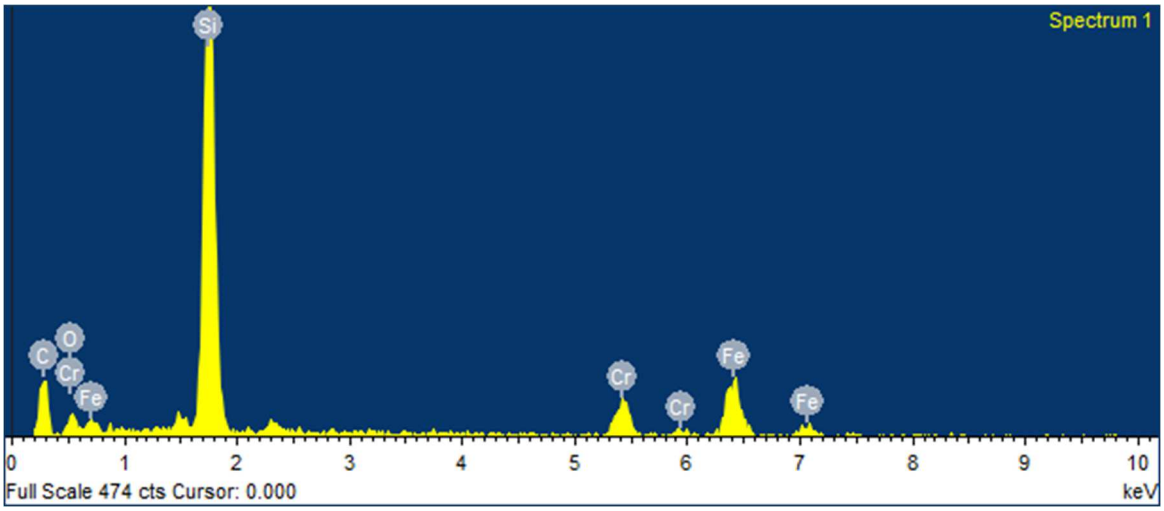



*Figure7.14*: EDX spectrum related to *Spectrum 1* of the ball scar.

It shows that the central region is rich in Silicon: this suggests Silicon transfer from the substrate to the ball counterpart. Of course, also the peaks of the other elements are visible, since the upper layer, formed by debris in this case, is thinner enough to allow the collection of the related signals.

*Figure7.15* displays *Spectrum 2* related to the brighter region.

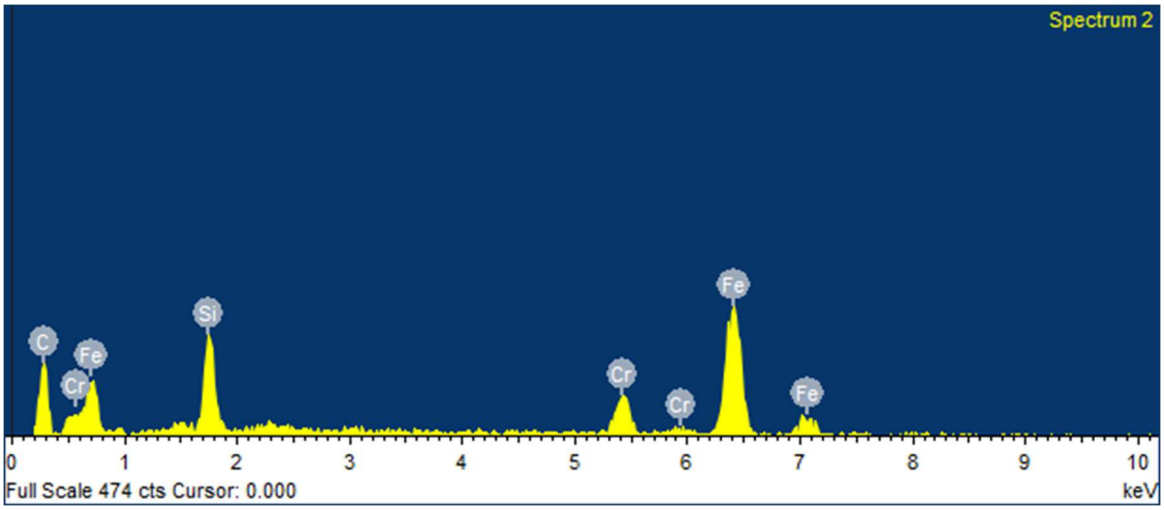



*Figure7.15*: EDX spectrum related to *Spectrum 2* of the ball scar.

This plot indicates that the exposed surface corresponds to the interlayer with Silicon transfer, as evidenced by the noticeable Silicon peak. The presence of the Fe peak is attributed to the steel substrate.

*Figure7.16* shows *Spectrum 3* which corresponds to the analysis of a black spot in the central area.

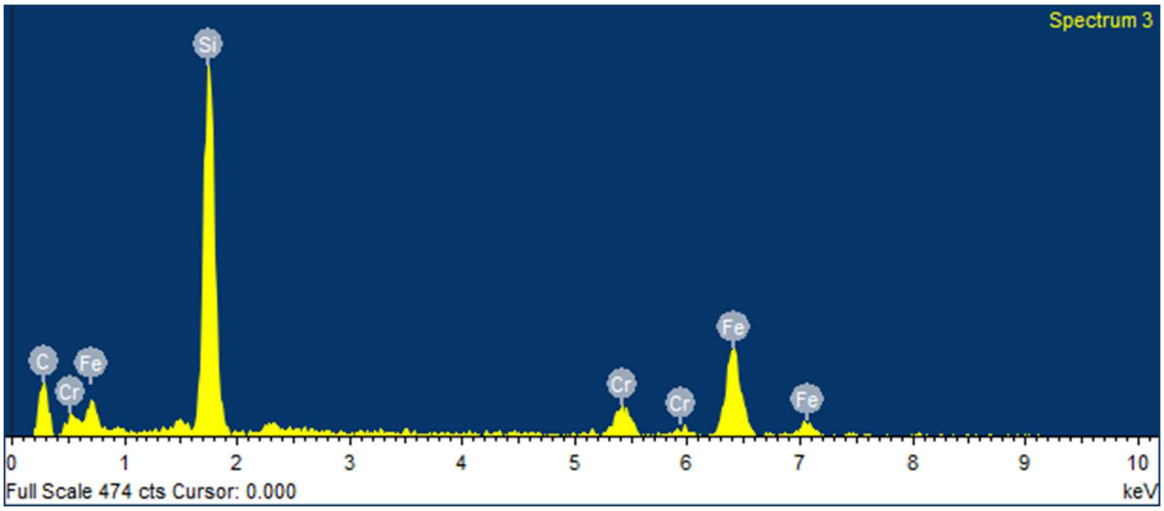



*Figure7.16:* EDX spectrum related to *Spectrum 3* of the ball scar.

The high intensity of the Silicon peak in the EDX analysis suggests that the debris consist primarily of Silicon, that are originated from the substrate.

In *Figure7.17*, the pristine surface spectrum (*Spectrum 4*) is displayed

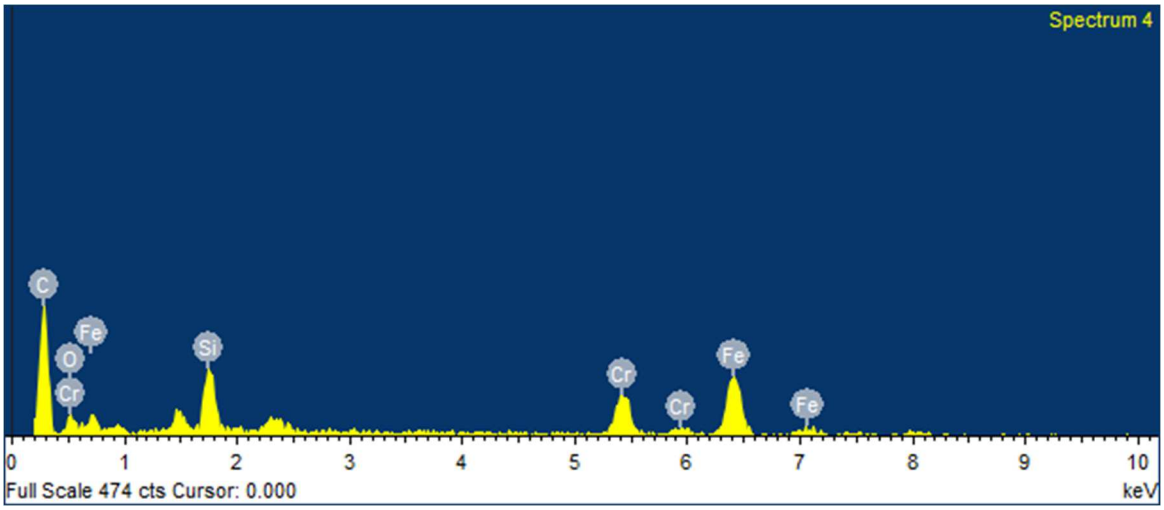



*Figure7.17:* EDX spectrum related to *Spectrum 4* of the ball scar.

This spectrum confirms that the deposited coating is primarily composed of Carbon, indicating the presence of DLC.

The following *Table7.11* wants to give a quantitative idea of the composition of each region:

| | **Element atomic %** | | | | |
|---|---|---|---|---|---|
| | C | O | Si | Cr | Fe |
| *Spectrum 1* | 68.09 | 7.52 | 17.64 | 2.08 | 4.66 |
| *Spectrum 2* | 75.63 | - | 6.12 | 3.03 | 15.22 |
| *Spectrum 3* | 72.40 | - | 17.02 | 2.04 | 8.54 |
| *Spectrum 4* | 79.05 | 8.99 | 3.19 | 2.83 | 5.94 |

*Table7.11*: atomic percentages of the elements in all the spectrum, evaluated by EDX technique.

To facilitate a clearer comparison between *Spectrum 1*, acquired from the central wear scar, and *Spectrum 4*, obtained from the pristine surface, *Figure7.18* presents a superposition of their respective peaks.

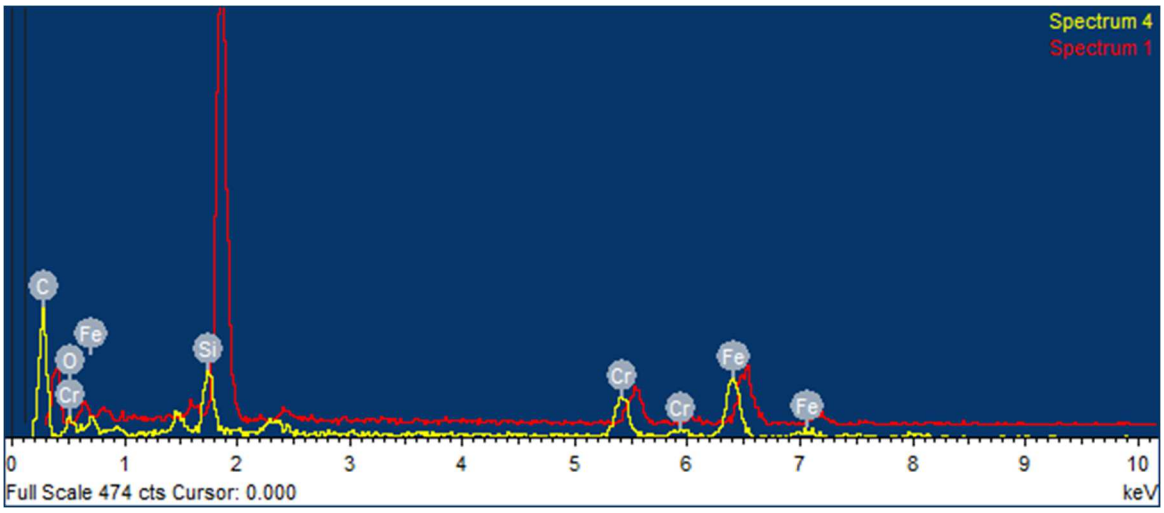



*Figure7.18*: EDX spectrum related to *Spectrum 1* and *4* of the ball scar.

It is evident that the Silicon signal is more intense in the worn area, possibly due to material transfer from the substrate. The peaks associated with the interlayer remain at similar intensity across all spectra, suggesting that while the DLC layer has been removed, the interlayer is still present. Indeed, even if the DLC appears to be uniformly deposited in *Spectrum 4*, the interlayer signal is still visible due to the small thickness of the coating. In *Spectrum 1*, the Carbon peak is notably less intense, indicating a reduced presence of DLC, probably in form of debris due to wear.

The corresponding track on Silicon substrate is very small, thus for the optical microscope image 20X magnification is required. In *Figure7.19*, it is displayed:

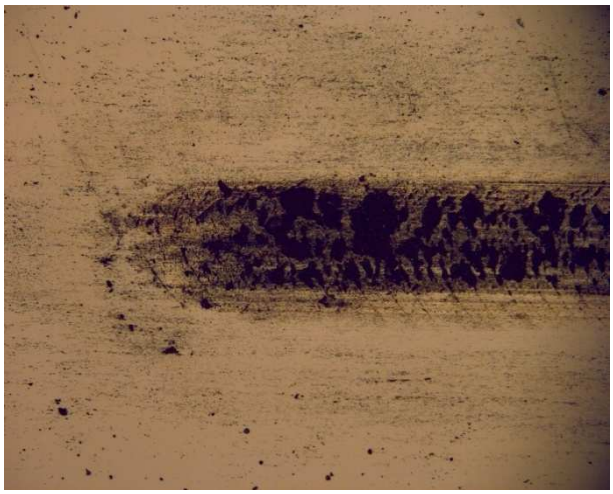


*Figure7.19*: image of the wear track related to 30s test on Si substrate taken with optical microscope (20X magnification).

Assuming that the DLC layer was removed during the test, the black spots visible on the track are likely parts of the coating, displaced by the ball counterpart.

Unfortunately, its EDX analysis could not be performed, as the worn area is not visually distinguishable through SEM backscattering detector. Consequently, selecting the regions of interest for investigation may lead to inaccurate results.

### 7.1.6 Potential future investigations

Since the recipe used for the DLC deposition is the usual one that works on flat sample, the no-uniformity coating obtained in this work is probably due to the spherical geometry of the sample, which does not allow a correct adhesion of the coating. For this reason, different courses of action were considered:

- A first possibility is to sand the spherical sample before the deposition: the roughness of the surface increases but in this way another parameter is introduced in discussion.
- The second possible solution is to create a flat surface on the sphere, which would be more suitable, as demonstrated in previous studies of the lab. However, this would change the tribological mode, turning it from ball on flat to flat on flat.
- Another possibility is to deposit DLC on a flat surface and Silicon on a spherical sample. In this case, preliminary studies would be necessary to determine the parameters for the deposition of Silicon.
- The last option was to implement a new ball holder that provides movement of the spherical sample during the deposition, hoping that the coating would grow uniformly all over the surface.

# 8. Conclusions and possible development lines

The growing energy demand, especially from widespread portable electronic devices, requires new technologies that are efficient, safe, and sustainable. TVNGs offer a promising solution by converting mechanical energy into electricity through the phenomenon of triboelectrification, which involves charge generation from contact and friction between materials. In this direction, this work aims to study the tribovoltaic effect for different materials couplings, through a parametrical approach, varying load, sliding frequency and relative humidity.

The first step of this work consisted in designing the experimental set-up able to simultaneously measure voltage and friction outputs. Different technical issues about both electrical and mechanical components arose during the test campaign, thus the implementation of the set-up consisted of many subsequent steps. The main criticalities were related to the measurement of a reliable and detectable electrical signal, which was obtained by modifying the existing standard tribometer, and by the definition of the optimal wiring of all the electrical parts. Another important technical issue was the integration of the new mechanical components in the existing tribometer maintaining the proper functioning.

The main studied coupling was Aluminum ball against Silicon substrate. The simultaneous detection of the friction and voltage signals were obtained, and the corresponding average values were extracted though a dedicated post-processing procedure.

CoF exhibits a clear evolution through three distinct regimes, due to the progressive wear and the subsequent transfer of material between the mating surfaces: running-in, low-friction, and high-friction regimes. Particular attention was paid to the low-friction regime, characterized by a relative small amount of debris produced during sliding. In this regime, the CoF does not show a clear dependence on the varied parameters, with an average value of approximately $0.60$. In contrast, the electrical measurements indicate that the generated voltage increases with both the applied load and the sliding frequency, as expected by the accepted interpretation of the process. The observed voltage variation range is $[\,0.19;\ 0.40]mV$.

To deepen the phenomenon, the tribovoltaic data have been combined with the study of the wear by means of topographical (profilometry, optical imaging, SEM) and chemical analyses (EDX) of the counterparts. The topographical analysis shows variations of the wear rate exclusively at higher normal loads, while the chemical analysis confirms the presence of material transferred between the two counterparts. Despite this, no clear correlations are pointed out within the limits of the accuracy offered by the current system.

With the purpose of studying an innovative material couplings, DLC coated ball against Silicon substrate was considered. However, the deposition of DLC on the spherical counterpart by PVD magnetron sputtering was not successful in terms of adherence of the coating, preventing the analyses of the expected tribovoltaic effect.

The present study could be considered as a starting point for investigating the tribovoltaic effect with other material couplings. Indeed, in addition to the already mentioned pairs, other promising systems can be investigated following the same set-up and procedures. In particular, the exploitation of new material combinations - such as HOPG-Si, DLC-HOPG, and Al-Ge - could represent a promising direction for advancing the field and identifying efficient real-world applications. These couplings are also of interest for theoretical simulations by molecular dynamics.

# 9. Bibliografia


1. *Electrons on dieletricts and contact electrification.* **C.Y. Liu, A.J. Bard.** 145-156, s.l. : Chem. Phys. Lett., 2009, Vol. 480.

2. *Electric potential decay on polyethylene: Role of atmospheric water on electric charge build-up and dissipation.* **T.A. Burgo, C.A. Rezende.** 401-409, s.l. : J. Electrostat., 2011, Vol. 4.

3. *Effect of humidity and pressure on the triboelectric nanogenerator.* **V. Nguyen, R. Yang.** 604, s.l. : Nano Energy, 2013, Vol. 2.

4. *In Situ Quantitative Study of Nanoscale Triboelectrification and Patterning.* **Y.S. Zhou, Y. Liu, Z. Lin, C. Pan.** 2771-2776, s.l. : Nano Lett., 2013, Vol. 13.

5. *A novel weight neighborhood centrality algorithm for identifying influential spreaders in complex networks.* **J. Wang, X. Hou, K. Li.** 88, s.l. : Nat. Commun., 2017, Vol. 8.

6. *Raising the Working Temperature of a Triboelectric Nanogenerator by Quenching Down Electron Thermionic Emission in Contact-Electrification.* **Xu, C.** 38, s.l. : Adv. Mater., 2018, Vol. 30.

7. *The role of material transfer in contact electrification.* **Lowell, J.** s.l. : J. Phys. D: Appl. Phys., 1977, Vol. 10.

8. *On the origin of contact-electrification.* **Z.L. Wang, A.C. Wang.** s.l. : Materials Today, 2019, Vol. 30.

9. *Triboelectric Nanogenerator: A Foundation of the Energy for the New Era.* **C. Wu, A. C. Wang, W. Ding, H. Guo, and Z. L. Wang.** 1802906, s.l. : Adv. Energy Mater, 2019, Vol. 9.

10. *Stretchable, transparent, and thermally stable triboelectric nanogenerators based on solvent-free ion-conducting elastomer.* **P. Zhang, Y. Chen, Z.H. Guo,.** 1909252, s.l. : Advanced Functional Materials, 2020, Vol. 30.15.

11. *The Triboelectric Nanogenerator as an Innovative Technology toward Intelligent Sports.* **J. Luo, W. Gao, Z.L. Wang.** 2004178, s.l. : Advanced Materials, 2021, Vol. 33.17.

12. *On Maxwell's displacement current for energy and sensors.* **Wang, Zhong Lin.** s.l. : Materials Today, 2017, Vol. 20.2.

13. *Triboelectric Nanogenerators: Design, Fabrication, Energy Harvesting, and Portable-Wearable Applications.* **V. Vivekananthan, A. Chandrasekhar.** 3, s.l. : Nanogenerators, 2020, Vol. 5.

14. *Tribovoltaic effect: Fundamental working mechanism and emerging applications.* **S. Sriphan, N. Vittayakorn.** 100318, s.l. : Materials Today, 2023, Vol. 22.

15. *The tribovoltaic effect.* **S. Lin, Z. L. Wang.** s.l. : Materials Today, 2023, Vol. 62.

16. *Tribological-behaviour-controlled direct-current triboelectric nanogenerator based on the tribovoltaic effect under high contact pressure.* **D. Yang, L. Zhang, N. Luo, Y. Liu, W. Sun, J. Peng,M. Feng, Y. Feng, H. Wang, D.** 107370, s.l. : Nano Energy , 2022, Vol. 99.

17. *Direct-current triboelectricity generation by a sliding Schottky nanocontact on MoS2 multilayers.* **J. Liu, A. Goswami, K. Jiang, F. Khan, S. Kim, R. McGee, Z. Li, Z. Hu,.** 112, s.l. : Nature Nanotech, 2018, Vol. 13.

18. *Sustained electron tunneling at unbiased metal-insulator-semiconductor triboelectric contacts.* **J. Liu, M. Miao, K. Jiang, F. Khan, A. Goswami, R. McGee, Z. Li, L.** 320, s.l. : Nano Energy, 2018, Vol. 48.

19. *Direct Current Triboelectric Nanogenerators, a Perspective from Material Selections.* **R. Xu, Q. Zhang, J. Y. Wang, D. Liu, J. Wang, Z. L. Wang,.** 104185, s.l. : Nano Energy, 2019, Vol. 66.

20. *Tribovoltaic Effect: Origin, Interface, Characteristic, Mechanism & Application.* **Z. Zhang, L. Gong, R. Luan, Y. Feng, J. Cao, C. Zhang.** 2305460, s.l. : Advanced Science, 2024, Vol. 11.

21. *Tribovoltaic Nanogenerator: a new mechanism for harvesting mechanical energy.* **J. Liu, Y. Zhang, J. Chen, R. Bao, K. Jiang, F. Khan, A. Goswami,.** 650, s.l. : Matter, 2019, Vol. 1.

22. *Tribovoltaic Effect on Metal–Semiconductor Interface for Direct-Current Low-Impedance Triboelectric Nanogenerators.* **Z. Zhang, D. Jiang, J. Zhao, G. Liu, T. Bu, C. Zhang, Z. L. Wang.** 1903713, s.l. : Adv. Energy Mater., 2020, Vol. 10.

23. *Tribo-thermoelectric and tribovoltaic coupling effect at metal-semiconductor interface.* **Z. Zhang, T. He, J. Zhao, G. Liu, Z. L.Wang, C. Zhang.** 100295, s.l. : Materials Today Physics, 2021, Vol. 16.

24. *The tribovoltaic effect and electron transfer at a liquid-semiconductor interface.* **S. Lin, X. Chen, Z. L. Wang.** 105070, s.l. : Nano Energy, 2020, Vol. 76.

25. *A dynamic adaptive self-powered sensor module for multi-parameter sensing.* **Y. Song, N. Wang, M. M. Fadlallah, S. Tao, Y. Yang, Z. L. Wang.** 105406, s.l. : Nano Energy, 2021, Vol. 79.

26. *Flexible tribovoltaic nanogenerator via static electric pumping and diesel-fuel lubrication.* **J. Meng, Z.H. Guo, C. Pan, L.Wang, C. Chang, L. Li, X. Pu, Z. L.Wang.** 2442, s.l. : ACS Energy Lett., 2021, Vol. 6.

27. *Microscale Schottky superlubric generator with high direct-current density and ultralong life.* **X. Huang, X. Xiang, J. Nie, D. Peng, F. Yang, Z. Wu, H. Jiang, Z. Xu.** 2268, s.l. : Nat. Commun., 2021, Vol. 12.

28. *High-current density tribovoltaic nanogenerator via asymmetric electrode design.* **H. Zheng, R. Shen, H. Zhong, Y. Lu, X. Yu, S. Lin.** 2105325, s.l. : Adv Funct Materials, 2021, Vol. 31.

29. *Broadband Self-Powered E-Skin for Noncontact Gesture Recognition via Tribovoltaic Effect.* **Z. Zhang, Z. Wang, Y. Chen, Y. Feng, S. Dong, H. Zhou, Z. L. Wang, C. Zhang.** 2200146, s.l. : Adv. Mater., 2022, Vol. 34.

30. *A broadband self-powered skin for noncontact health monitoring via tribovoltaic effect.* **Z. Wang, Z. Zhang, Y. Chen, L. Gong, S. Dong, H. Zhou, Y. Lin, Y. Lv, G. Liu, C. Zhang.** 2366, s.l. : Energy Environ. Sci., 2022, Vol. 15.

31. *Tribovoltaic Effect–Driven Self-Powered Frequency-Tunab le Broadband Mechanical-Energy Harvester.* **W. Qiao, Z. Zhao, L. Zhou, S. Li, P. Yang, X. Li, J. Liu, J. Wang, Z. L. Wang.** 2208544, s.l. : Adv. Funct Materials, 2022, Vol. 32.

32. *Self-Powered Flexible Triboelectric Nanogenerator Based on Microstructure-Engineered Polymer Films for Wearable Energy Harvesting.* **H. Yuan, Z. Xiao, J. Wan, Y. Xiang, G. Dai, H. Li, J. Yang.** 2200550, s.l. : Adv. Energy. Mater., 2022, Vol. 12.

33. *Tunable Tribovoltaic Effect via Metal–Insulator Transition.* **R. Yang, Z. He, S. Lin,W. Dou, Z. L.Wang, H.Wang, J. Liu.** 9084, s.l. : Nano. Lett., 2022, Vol. 22.

34. *Self-Powered Smart Textile Based on Dynamic Schottky Diode for Human-Machine Interactions.* **P. Deng, Y. Wang, R. Yang, Z. He, Y. Tan, Z. Chen, J. Liu, T. Li.** 2207298, s.l. : Adv. Sci., 2023, Vol. 10.

35. *A High Current Density Direct-Current Generator Based on a Moving van der Waals Schottky Diode.* **S. Lin, * Y. Lu, S. Feng, Z. Hao, Y. Yan.** 1804398, s.l. : Adv. Mater., 2018.

36. *Study of interfacial design for direct-current tribovoltaic generators.* **X. Xiu, J. Li, X. Tao,.** 2022, Nano Energy, p. 9.

37. *A humidity-enhanced silicon-based semiconductor tribovoltaic direct-current nanogenerator.* **Z.Wang, L.Gong, S.Dong, B.Fan, Y.Feng, Z.Zhang, C.Zhang.** 25230-25237, s.l. : Materials Chemistry A, 2022, Vol. 10.

38. *Friction and wear of DLC films deposited on additive manufactured AlSi10Mg: the role of surface finishing.* **E. Salerno, D. Casotti, G.Paolicelli, E. Gualtieri, A. Ballestrazzi, G.C. Gazzadi, G. Bolelli, L. Lusvarghi, S. Valeri, A. Rota.** 129531, s.l. : Surface & Coatings technology, 2023, Vol. 463.

39. *Diamond-like carbon — present status.* **Y. Lifshitz.** s.l. : Diamond and Related Materials, 1999, Vol. 8.

40. *Electronic and optical properties of amorphous carbon with different sp3/sp2 hybridization ratio.* **L. Liu, F. Lu, J. Tian, S. Xia, Y.Diao.** s.l. : Applied Physics A, 2019.

41. *Evaluation of DLC, MoS2, and Ti3C2Tx thin films for triboelectric nanogenerators.* **S. Tremmel.** 107185, s.l. : Nano Energy, 2022, Vol. 97.

42. *Investigation of diamond-like carbon films as a promising dielectric material for triboelectric nanogenerator.* **S.H. Ramaswamy, J. Shimizu, W. Chen, R. Kondo, J. Choi.** 875-885, s.l. : Nano Energy, 2019, Vol. 60.

43. *A novel ultrahigh-speed ball-on-disc tribometer.* **T. Zhang, F. Jiang, L. Yan, Z. Jiang, X. Xu.** 106901, s.l. : Tribology International, 2021, Vol. 157.

44. *Fiber/fabric-based piezoelectric and triboelectric nanogenerators for flexible/stretchable and wearable electronics and artificial intelligence.* **K. Dong, X. Peng, Z.L. Wang.** 1902549, s.l. : Advanced Materials, 2020, Vol. 32.5.

45. *Assessment of energy storage technologies: A review.* **M.M Rahman.** 113295, Edmonton : Energy conversion and Management - Elsevier, 2020, Vol. 223.

46. *A flexible fiber-based supercapacitor–triboelectric nanogenerator power system for wearable electronics.* **J. Wang, X. Li, et al.** 4830-4836, s.l. : Advanced Materials, 2015, Vol. 27.33.

47. *Textile based triboelectric nanogenerators for self-powered wearable electronics.* **S.S. Kwak, H.J.Yoon, S.W. Kim.** 1804533, s.l. : Advanced Functional Materials, 2019, Vol. 29.2.

48. *From contact electrification to triboelectric nanogenerators.* **Z.L. Wang.** s.l. : Reports Prog. Phys., 2021, Vol. 84.